Vertical Transport of van der Waals Materials and Their Application in Hot Electron Transistors

Zhu, Xiaodan

2017

UNIVERSITY OF CALIFORNIA

Los Angeles

Vertical Transport of van der Waals Materials and Their Application in Hot Electron Transistors

A dissertation submitted in partial satisfaction of the
requirements for the degree Doctor of Philosophy
in Materials Science and Engineering

by

Xiaodan Zhu

2017

ABSTRACT OF THE DISSERTATION

Vertical Transport of van der Waals Materials and Their Application in Hot Electron Transistors

by

Xiaodan Zhu

Doctor of Philosophy in Materials Science and Engineering

University of California, Los Angeles, 2017

Professor Qibing Pei, Co-Chair

Professor Kang Lung Wang, Co-Chair

Vertical integration of van der Waals (vdW) materials into heterostructures with atomic precision is one of the most intriguing possibilities brought forward by these 2-dimensional (2D) materials. Essential to the design and analysis of these structures is a fundamental understanding of the vertical transport of charge carriers into and across vdW materials. In this dissertation, I explore the important roles of single layer graphene in the vertical tunneling process, both as a collecting electrode and as a vdW tunneling barrier, and explore graphene's application as the base material of hot electron transistors (HETs).

When graphene comes into contact with highly doped silicon, a fully preserved vdW gap is formed at the interface, which acts effectively as a tunnel barrier. In the scenario where graphene acts as the collecting electrodes, the electrons injected from the highly doped silicon are captured by graphene, and propagate laterally through graphene. Using electron tunneling spectroscopy (ETS), it is shown that this process is limited by the relaxation of carriers into the linear density

of states of graphene.

When graphene is sandwiched between two electrodes, the graphene layer together with the vdW gap act as a tunnel barrier that is transparent to the vertically tunneling electrons due to its atomic thickness and the mismatch of transverse momenta between the injected electrons and the graphene band structure. This is accentuated from the ETS showing a lack of features corresponding to the Dirac cone band structure of the graphene. Meanwhile, the graphene acts as a lateral conductor through which the potential and charge distribution across the tunnel barrier can be tuned. These unique properties make graphene an excellent 2D atomic net, which is transparent to charge carriers, and yet it can control the carrier flux via electrical potential at the same time. A new model including the effect of the quantum capacitance of the graphene for vertical tunneling is developed to further elucidate the role of graphene in modulating the tunneling process.

As a result of the unique vertical transport properties of graphene, hot electron transistors with graphene as the base material and the vdW gap as the tunnel barrier can be fabricated, eliminating the need for an additional tunnel barrier. This leads to significantly increased current densities, as well as minimized energy loss for the hot electrons in the tunnel barrier, which in turn leads to lower turn on voltages and higher current gain, compared to previous reports of graphene based HETs.

The dissertation of Xiaodan Zhu is approved.

Ya-Hong Xie

Chee Wei Wong

Qibing Pei, Co-Chair

Kang Lung Wang, Co-Chair

University of California, Los Angeles

2017

Dedicated to my parents

for their love and support

Table of Contents

List of Figures

List of Tables

ACKNOWLEDGEMENTS

It has been more than six years since I joined the Device Research Laboratory (DRL) in UCLA. I feel truly blessed to have the chance of studying and conducting research in this amazing group. I would like to express my deepest gratitude towards Professor Kang Lung Wang, for his continuous support and guidance throughout all these years. He is not only the best research advisor any student could hope to have; he is a mentor to me in all aspects of my life. For every project that my colleagues and I worked on, Professor Wang always challenges us to think more deeply, present our work more clearly, and make the physical picture more complete. He imprinted upon us to always find the basic principles and fundamental physics behind each experiment and observation, which I believe is the characteristic of a true researcher and scientist.

I would also like to thank Professor Qibing Pei for acting as my co-chair in the department of Materials Science and Engineering, and for all his help throughout my PhD study and research. Moreover, I would like to acknowledge with much appreciation Professor Yahong Xie of the UCLA department of Materials Science and Engineering and Professor Chee Wei Wong of UCLA department of Electrical Engineering for taking the time among their busy schedules to act as my PhD dissertation committee, and for their insightful comments and suggestions, which greatly improved the quality of this work. I am grateful to Professor Pulickel M. Ajayan of Rice University and his students for providing us high quality and large area graphene and other van der Waals material samples. I would also like to thank Professor Yong Wang of Zhejiang University and his students for performing the TEM analysis on our samples, and Professor Roger K. Lake of University of California, Riverside for valuable discussions on the tunneling model of the vertical transport across graphene.

I am honored to have the pleasure of working with such talented people as gathered in DRL. Special thank goes to Dr. Sidong Lei, who works closely with me in constructing the transport and capacitance model of the vertical transport of graphene; without his effort, the work presented in this thesis would not be possible. Many thanks to Dr. Mark A. Zurbuchen. I have learned so much from our discussions. I would like to thank all my dear colleagues for their friendship and collaboration, especially Dr. Mei Xue, Dr. Ryan Hoekstra, Dr. Chandan Biswas, Dr. Yan-Wenn Lan, Dr. Carlos M. Torres Jr., Dr. Gen Yin, Aryan Navabi, Hussam Qasem and Shin-Hung Tsai for their help and collaboration. I am very grateful for the assistance and help from the staff of the UCLA Nanoelectronics Research Facility, especially Hoc Ngo, Wilson Lin and Max Ho.

Finally, no words can express my deepest gratitude towards my parents and my husband. Their unconditional love and support provide me with unending strength and inspiration.

Xiaodan Zhu

Los Angeles, March 2017

VITA

2010 B.S. Physics, Peking University, P. R. China

2010-2017 PhD Candidate, Materials Science and Engineering, University of California, Los Angeles, CA, USA

PUBLICAITIONS

1. H. Medina, J.-G. Li, T.-Y. Su, Y.-W. Lan, S.-H. Lee, C.-W. Chen, Y.-Z. Chen, A. Manikandan, S.-H. Tsai, A. Navabi, **X. Zhu**, Y.-C. Shih, W.-S. Lin, J.-H. Yang, St. R. Thomas, B.-W. Wu, C.-H. Shen, J.-M. Shieh, H.-N. Lin, A. Javey, K. L. Wang, Y.-L. Chueh, 'Wafer-Scale Growth of WSe_2 Monolayers Toward Phase-Engineered hybrid WO_x/WSe_2 Films with Sub-ppb NO_x Gas Sensing by A Low Temperature Plasma-Assisted Selenization Process', *Chemistry of Materials*, 29 (2017), 1587–1598.

2. Q. L. He, X. Kou, A. J. Grutter, G. Yin, L. Pan, X. Che, Y. Liu, T. Nie, B. Zhang, S. M. Disseler, B. J. Kirby, W. Ratcliff II, Q. Shao, K. Murata, **X. Zhu**, G. Yu, Y. Fan, M. Montazeri, X. Han, J. A. Borchers, K. L. Wang, 'Tailoring exchange couplings in magnetic topological-insulator/antiferromagnet heterostructures', Nature Nanotechnology, 16 (2016), 94-100.

3. Q. Shao, G. Yu, Y.-W. Lan, Y. Shi, M.-Y. Li, C. Zheng, **X. Zhu**, L.-J. Li, P. Khalili Amiri, K. L. Wang, 'Strong Rashba-Edelstein Effect-Induced Spin-Orbit Torques in Monolayer Transition Metal Dichalcogenides/Ferromagnet Bilayers', Nano Letters, 12 (2016), 7514-7520.

4. T. Nie, J. Tang, X. Kou, Y. Gen, S. Lee, **X. Zhu**, Q. He, L.-T. Chang, K. Murata, Y. Fan, K. L. Wang, 'Enhancing electric-field control of ferromagnetism through nanoscale engineering of high-Tc Mn_xGe_{1-x} nanomesh', Nature Communications, 7 (2016), 12866.

5. C. Biswas, Z. Ma, **X. Zhu**, T. Kawaharamura, K. L. Wang, 'Atmospheric growth of hybrid ZnO thin films for inverted polymer solar cells', *Solar Energy Materials and Solar Cells*, 157 (2016), 1048-1056.

6. Y.-W. Lan, C. M. Torres Jr., S.-H. Tsai, **X. Zhu**, Y. Shi, M.-Y. Li, L.-J. Li, W.-K. Yeh, K. L. Wang, 'Atomic-Monolayer MoS_2 Band-to-Band Tunneling Field-Effect Transistor', *Small*, published online August 2016.

7. Y.-W. Lan, C. M. Torres Jr., **X. Zhu**, H. Qasem, J. R. Adleman, M. B. Lerner, S.-H. Tsai, Y. Shi, L.-J. Li, W.-K. Yeh, K. L. Wang, 'Dual-mode Operation of 2D Material-base Hot Electron Transistors', *Scientific Reports*, 6 (2016), 32503.

8. Y.-W. Lan, C. M. Torres Jr, **X. Zhu**, C.-L. Sun, C.-D. Chen, K. L. Wang, 'Self-aligned

Graphene Oxide Nanoribbon Stack with Gradient Bandgap for Visible-light Photodectection', *Nano Energy,* 27 (2016), 114-120.

9. L. Duan, J. Wang, K. Yue, **X. Zhu**, K. L. Wang, 'C-S@PANI Composite with Polymer Spherical Network Structure for High Performance Lithium-sulfur Batteries', *Physical Chemistry Chemical Physics*, 18 (2016), 261-266.

10. **X. Zhu**, T. Kawaharamura, A. Z Stieg, C. Biswas, L. Li, Z. Ma, M. Zurbuchen, Q. Pei, K. L. Wang, 'Atmospheric and Aqueous Deposition of Polycrystalline Metal Oxides Using Mist-CVD for Highly Efficient Inverted Polymer Solar Cells', *Nano Letters*, 8 (2015), 4948–4954.

11. L. Li, J. Liang, S.-Y. Chou, **X. Zhu**, X. Niu, Q. Pei, 'A Solution Processed Flexible Nanocomposite Electrode with Efficient Light Extraction for Organic Light Emitting Diodes', *Scientific Reports*, 4 (2014), 4307.

12. J. Zhu, **X. Zhu**, R. Hoekstra, L. Li, F. Xiu, M. Xue, B. Zeng, and K. L. Wang, 'Metallic nanomesh electrodes with controllable optical properties for organic solar cells.' *Applied Physics Letters*, 100 (2012), 143109.

CONFERENCES

1. **X. Zhu**, S. Lei, K. L. Wang, 'High Current Gain 2D Hot Electron Transistors', Presentation, Center for Excellence for Green Nanotechnology (CEGN), 2016 UCLA Workshop, Los Angeles.

2. **X. Zhu**, T. Kawaharamura, A. Stieg, C. Biswas, L. Li, Z. Ma, Q. Pei, K. L. Wang, 'Scalable Processing of Metal Oxides Using Atmospheric Mist-CVD for High Efficiency Inverted Polymer Solar Cells', Poster, 2014 MRS Fall Meeting, Boston.

Chapter 1 Introduction

1.1 The Advent of van der Waals (vdW) Materials

Since the successful isolation of graphene in 2004[1], the ability to obtain vdW materials with thickness down to one atomic layer has opened up myriads of opportunities for the observation of new physical phenomena, as well as realizing practical applications in completely new ways. Graphene is a monolayer of carbon, and can be seen as the basis for other carbon materials. It can be wrapped up into 0-dimentional buckyballs, rolled into 1-dimentional carbon nanotubes and stacked into graphite (Fig. 1.1)[2].

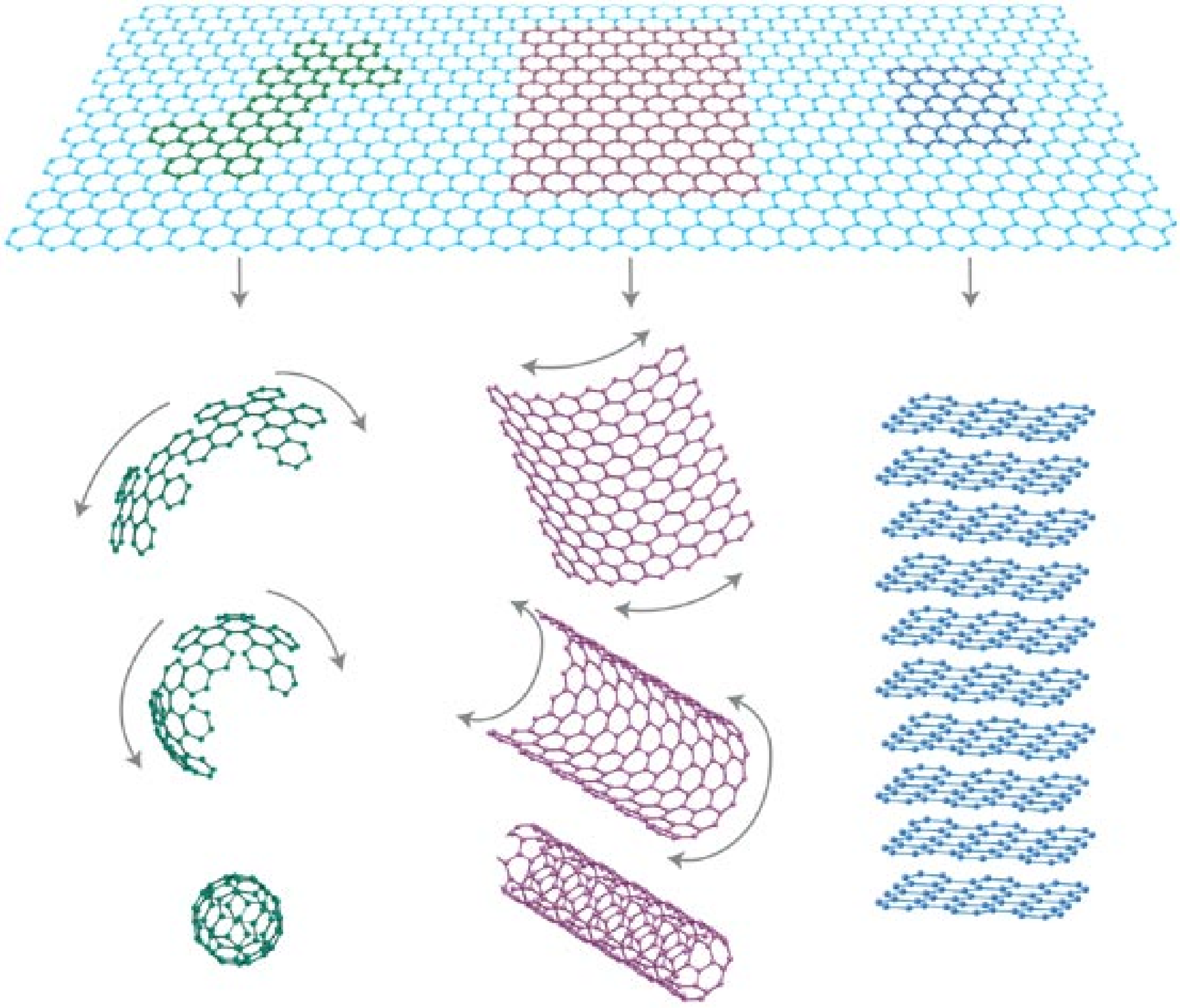

Figure 1.1 The atomic structure of graphene and its relation to other carbon based materials. Graphene can wrap up into 0-dimention fullerene, roll up into carbon nanotubes and stack vertically to form graphite. Adapted with permission from ref. (2). Copyright 2007 Nature Publishing Group (NPG).

The discovery of graphene can be attributed to the facile but effective process of mechanical exfoliation of graphite[3], and graphene is later produced in a variety of methods, including molecular beam epitaxy (MBE)[4], chemical vapor deposition (CVD)[5, 6] and liquid phase exfoliation[7], resulting in graphene with a wide range of flake sizes and material properties, which enables numerous potential applications for this unique material. Especially important for the area of electronics and relevant to this thesis is the growth of graphene using CVD, which is capable of producing single layer graphene in large areas (up to tens of inches in dimension)[8], making wafer-scale device manufacturing possible.

Immediately following the discovery of graphene, numerous vdW materials are successfully isolated into single layers and investigated. A whole family of vdW materials are available now, with electrical properties spanning semi-metallic (graphene), semiconducting (transition metal dichalcogenides (TMDs)[9], black phosphorus[10]), and insulating (hexagonal boron nitride, *h*-BN[11]) (summarized in Fig. 1.2[12]).

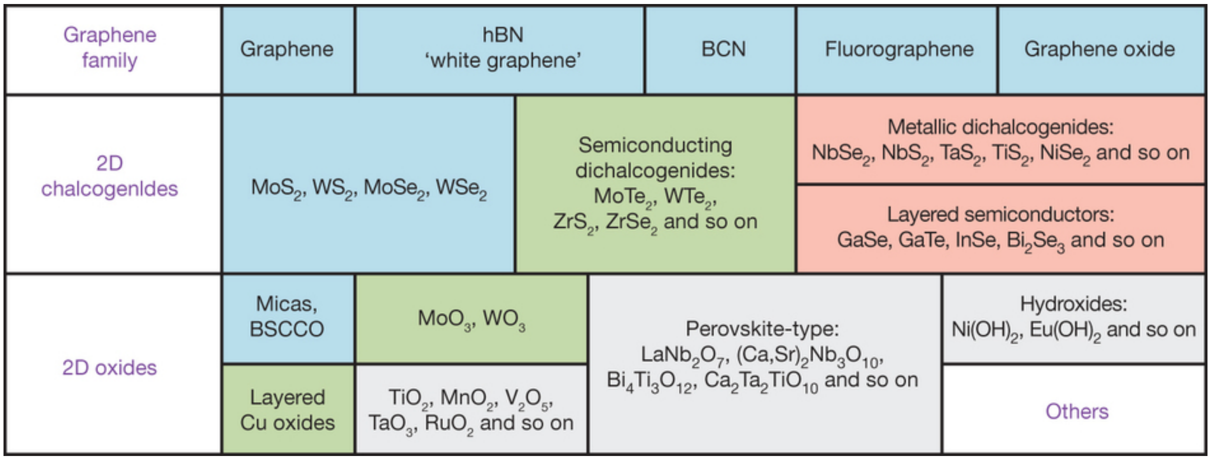

Graphene family	Graphene	hBN 'white graphene'	BCN	Fluorographene	Graphene oxide
2D chalcogenides	MoS_2, WS_2, $MoSe_2$, WSe_2	Semiconducting dichalcogenides: $MoTe_2$, WTe_2, ZrS_2, $ZrSe_2$ and so on		Metallic dichalcogenides: $NbSe_2$, NbS_2, TaS_2, TiS_2, $NiSe_2$ and so on	
				Layered semiconductors: GaSe, GaTe, InSe, Bi_2Se_3 and so on	
2D oxides	Micas, BSCCO	MoO_3, WO_3	Perovskite-type: $LaNb_2O_7$, $(Ca,Sr)_2Nb_3O_{10}$, $Bi_4Ti_3O_{12}$, $Ca_2Ta_2TiO_{10}$ and so on	Hydroxides: $Ni(OH)_2$, $Eu(OH)_2$ and so on	
	Layered Cu oxides	TiO_2, MnO_2, V_2O_5, TaO_3, RuO_2 and so on		Others	

Figure 1.2 Existing members of the 2-dimentional (2D) materials family. Materials that are

stable in ambient conditions are shaded in blue, those that are less stable shaded in green, and those shaded pink are only stable in inert atmosphere. Materials that are shaded in grey are 3-dimentional (3D) materials that can be exfoliated down to single layer. Adapted with permission from ref. (12). Copyright 2013 NPG.

These vdW materials exhibit many exciting properties on their own, such as ultra-high mobility[13], ferromagnetism[14] and anti-ferromagnetism[15], as well as topologically protected edge conducting states[16]. A more intriguing opportunity is the ability to stack vdW materials with different properties into heterojunctions with atomic precision in the vertical direction (Fig. 1.3)[12]. These atomically thin vdW materials feature dangling bond free surfaces, making them the ideal candidates to be stacked together with well controlled interfaces (that is, vdW gaps) in between. This greatly enhanced our ability to create ultrathin heterostructures, which traditionally can only be realized through careful choices of lattice matched material with precisely controlled MBE or metallic organic chemical vapor deposition.

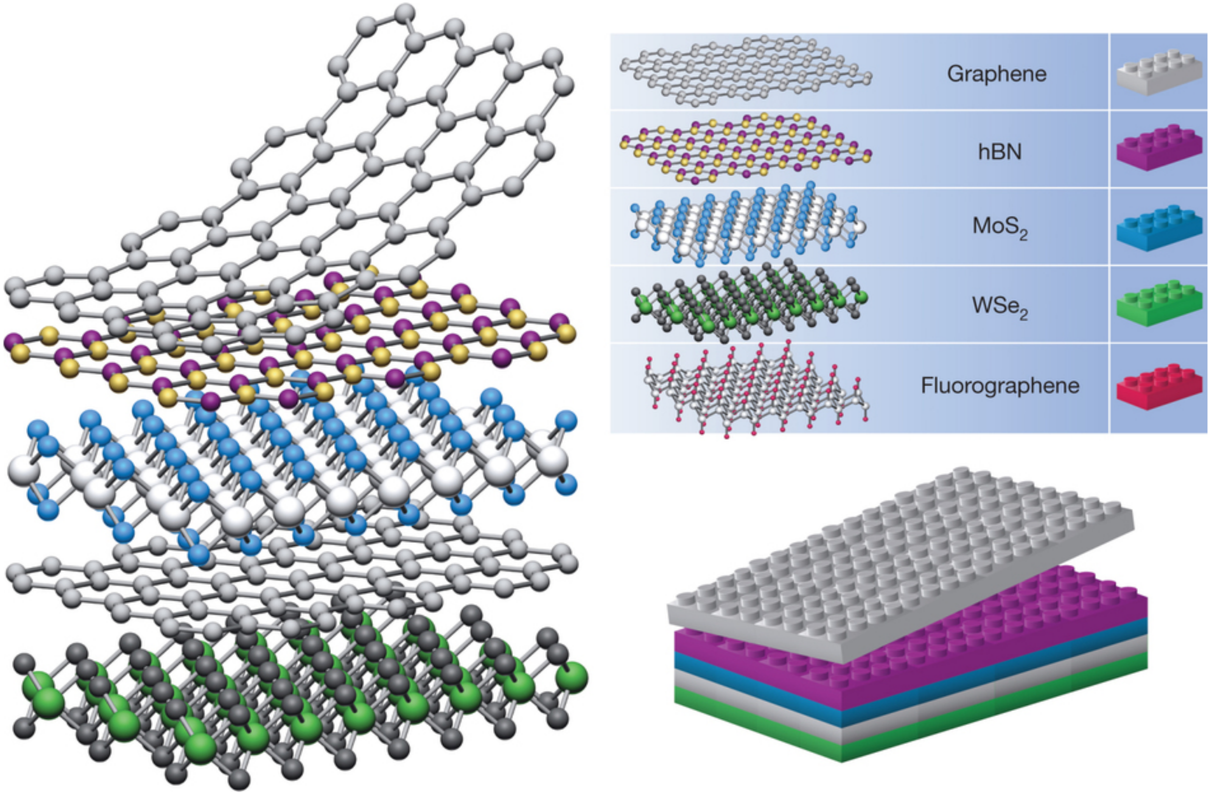

Figure 1.3 Schematic diagram illustrating the stacking of vdW materials into vdW heterostructures. Atomically thin vdW materials can be stacked into carefully designed heterostructures like Lego blocks to realize different functionalities. Adapted with permission from ref. (12). Copyright 2013 NPG.

Two strategies have been explored to achieve this atomic stacking: mechanical assembly and direct growth (Fig. 1.4a)[17]. Mechanical assembly is capable of integrating materials with distinct lattice parameters and growth conditions, but run the risk of material contamination and degradation during the stacking process. Intricate heterostructures have been produced using this method. For example, quantum well based light emitting diodes (LEDs) consisting of more than ten layers of vdW materials have been demonstrated by Withers *et al.* with a quantum efficiency of 10 %, (Fig. 1.4b)[18]. Direct growth can only integrate materials with compatible growth conditions, but its advantage is obvious: it can produce heterojunctions with atomically sharp and clean interfaces with controlled twist angle between each layer. Gong *et al*. have shown the growth of MoS_2/WS_2 vertical heterojunctions synthesized using CVD (Fig. 1.4c)[19]. Using these two strategies, heterostructures with a number of functionalities have been produced, including vertical transistors[20], photovoltaics[21], photodetectors[22], LEDs[18] and etc.

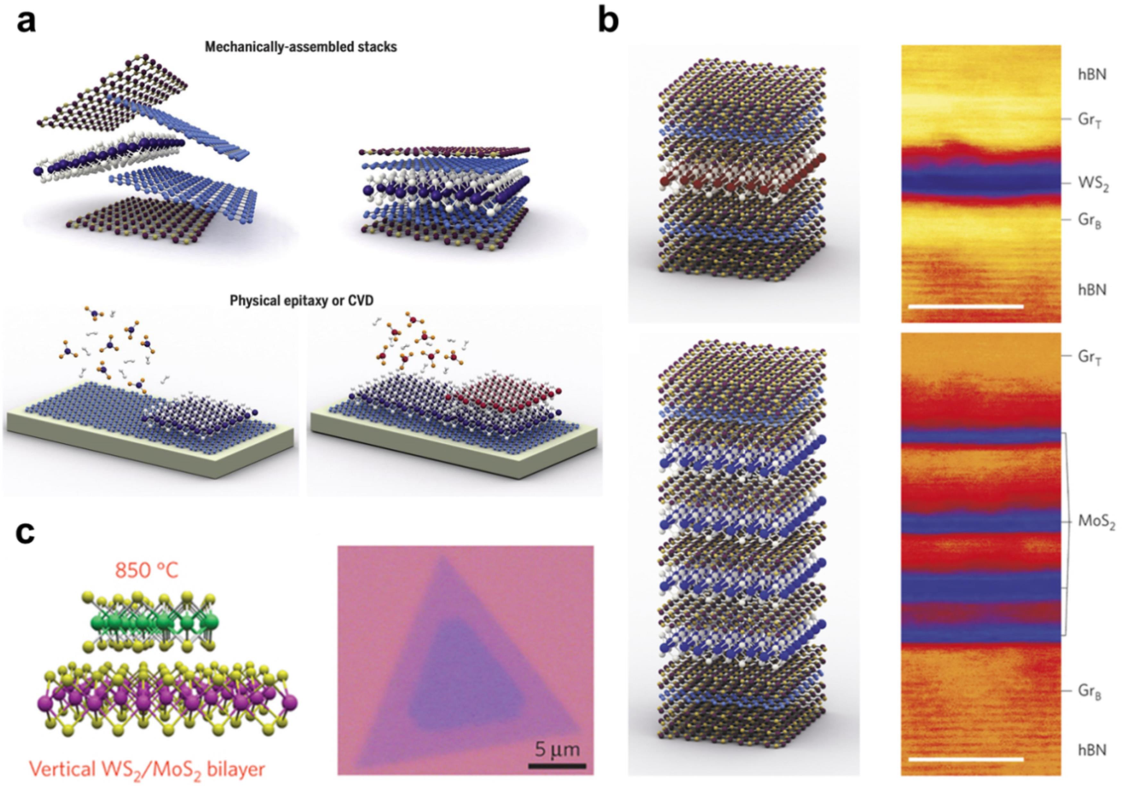

Figure 1.4 Fabrication of vdW material heterostructures. a, Schematic illustrations of two methods to fabricate vdW material heterostructures: mechanical assembly and direct growth using physical epitaxy or CVD. **b,** Quantum well based LEDs with a structure of *h*-BN/Gr/*h*-BN/WSe_2/*h*-BN/Gr/*h*-BN (top) and *h*-BN/Gr/*h*-BN/MoS_2/*h*-BN/MoS_2/*h*-BN/MoS_2/*h*-BN/MoS_2/*h*-BN/Gr/*h*-BN (bottom) fabricated using the mechanical assembly method. Schematics showing the atomic structure of the stack and cross-sectional bright field scanning transmission electron microscopy images are shown. **c,** Vertical WS_2/MoS_2 heterojunction grown using CVD. Schematic diagram of the structure is shown along with an optical image of the structure. Adapted with permission from ref. (17-19). Copyright 2016 American Association for the Advancement of Science (AAAS), 2015 NPG, 2014 NPG.

1.2 Electronic Properties of Graphene and Alternative vdW Materials

1.2.1 Electronic Properties of Graphene

Graphene exhibits a unique semi-metallic electrical behavior. It is a single layer of carbon atoms arranged in a honey-comb configuration. It is made up of a triangular lattice with a basis of two carbon atoms as denoted by the two set of yellow and blue dots in Fig. 1.5a. The reciprocal lattice of graphene is shown in Fig. 1.5b, and the corner of the Brillouin Zone, K and K' points are termed the Dirac points[23].

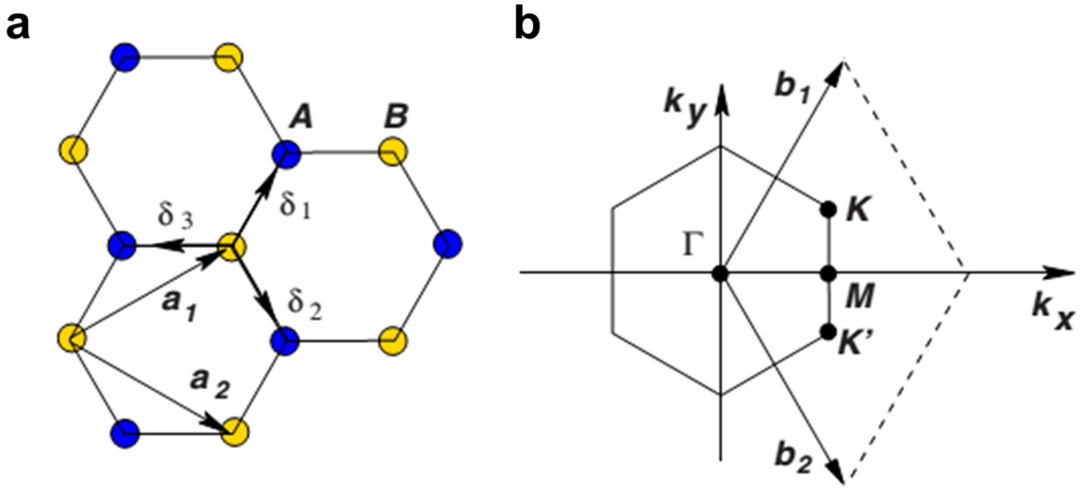

Figure 1.5 Lattice structure of graphene. a, The honey-comb lattice of graphene. It is consisted of a trigonal lattice with a basis of two carbon atoms (the blue dots, A and the yellow dots, B). The two vectors, $\mathbf{a}_1$ and $\mathbf{a}_2$, are the lattice vectors of the trigonal lattice. The nearest neighbor vectors, δ_1, δ_2 and δ_3, are also given. **b,** The Brillouin Zone of graphene with the reciprocal lattice vectors given as $\mathbf{b}_1$ and $\mathbf{b}_2$. Corners of the Brillouin Zone, **K** and **K'**, is where the Dirac cones are located. Adapted with permission from ref. (23). Copyright 2009 American Physical Society (APS).

The four valence electrons of graphene occupy one *s* orbital and 3 *p* orbitals. As a result of the sp^2 hybridization, three of the valence electrons form covalent carbon-carbon bonds, the σ bond, which form a planar trigonal structure, and is responsible for the high robustness of the graphene lattice. The remaining *p* orbital bond covalently with neighboring atoms to form the out of plane π bond. The π bond is half-filled, which is the source of the exceptional electrical conduction observed in graphene.

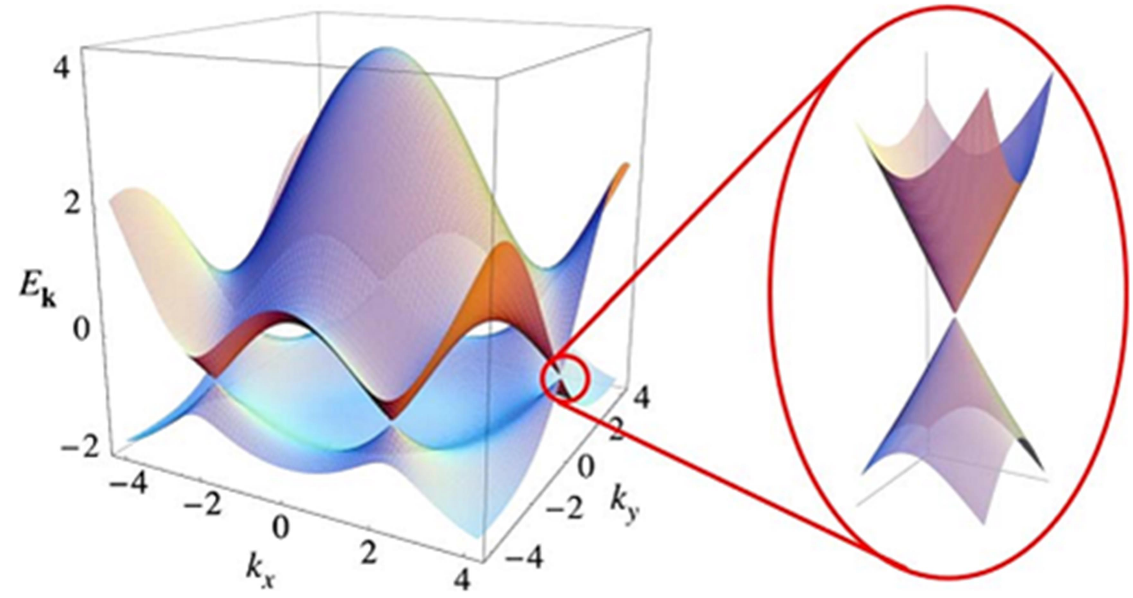

Figure 1.6 2D energy spectrum of graphene calculated using the tight binding model. To obtain this result it is assumed that the nearest neighbor hopping energy, $t = 2.7\ eV$ and the next nearest neighbor hopping energy, $t' = -0.2t$. Inset shows a zoomed in image of the energy spectrum near the Dirac point where the two Dirac cone meet, and linear energy dispersion is observed. Adapted with permission from ref. (23). Copyright 2009 APS.

The electronic energy dispersion of graphene can be calculated using the tight binding approach, which considers hopping between nearest neighbors and next nearest neighbors. The Hamiltonian for electrons in graphene is given as[23]:

$$H = -t \sum_{\langle i,j\rangle,\sigma} (a^{\dagger}_{\sigma,i}\, b_{\sigma,j} + b^{\dagger}_{\sigma,j} a_{\sigma,i}) - t' \sum_{\langle\langle i,j\rangle\rangle,\sigma} (a^{\dagger}_{\sigma,i}\, a_{\sigma,j} + b^{\dagger}_{\sigma,i} b_{\sigma,j} + a^{\dagger}_{\sigma,j} a_{\sigma,i} + b^{\dagger}_{\sigma,j} b_{\sigma,i}) \quad (1.1)$$

in which $a_{i,\sigma}$ ($a^{\dagger}_{i,\sigma}$) annihilates (creates) an electron with the spin σ ($\sigma = \uparrow, \downarrow$) on site $\mathbf{R_i}$ on sublattice A (similar definition is used for sublattice B). t is the nearest neighbor hopping energy, and t' is the next nearest neighbor hopping energy. The band structure of graphene with finite values of t and t' can be derived, and the result is shown in Fig. 1.6.

The zoomed in image of the energy dispersion around the Dirac points reveals that the π band and the π^* band meet exactly at the Dirac point (inset of Fig. 1.6) and for neutral graphene, the

Fermi level crosses the Dirac point. Expansion near the Dirac point results in a linear energy dispersion relation[24]:

$$E = \hbar v_F k \tag{1.2}$$

in which k is the momentum relative to K (K'), and v_F is the Fermi velocity with the value $v_F \simeq 1 \times 10^6 m/s$. This relation is analogous to that of massless fermions in quantum electrodynamics, therefore electrons in graphene are called massless Dirac fermions, and propagates in graphene at a velocity of v_F, independent of the energy and momentum. As a result of the linear energy dispersion, the effective mass of graphene, $m^* = \frac{1}{\hbar^2}\frac{d^2E}{dk^2}$, equals zero. The density of states (DOS) of graphene in the vicinity of the Dirac cone can be derived from equation 1.2 to be a linear function of energy:

$$\rho(E) = \frac{g_s g_v A_c |E|}{2\pi(\hbar v_F)^2} \tag{1.3}$$

where $g_s = 2$ and $g_v = 2$ is the spin and valley degeneracy respectively, A_c is the area of the unit cell and is given by $A_c = 3\sqrt{3}a^2/2$, in which $a \approx 1.42$ Å is the carbon-carbon distance. Many of the fascinating electronic properties of graphene comes from the fact that electrons in graphene mimic relativistic particles, such as room temperature integer quantum Hall effect[25] and Klein paradox[26] to name a few.

1.2.2 Electronic Properties of vdW Materials beyond Graphene

Graphene acts as a zero bandgap semiconductor or semi-metal; this limits its application in certain electronic applications as well as opto-electronic devices. Thus, a growing number of alternative vdW materials are being explored, with electronic properties ranging insulators, semiconductors to superconductors and topological insulators. This has enabled the realization of ultra-thin functional heterojunctions composed entirely of vdW materials.

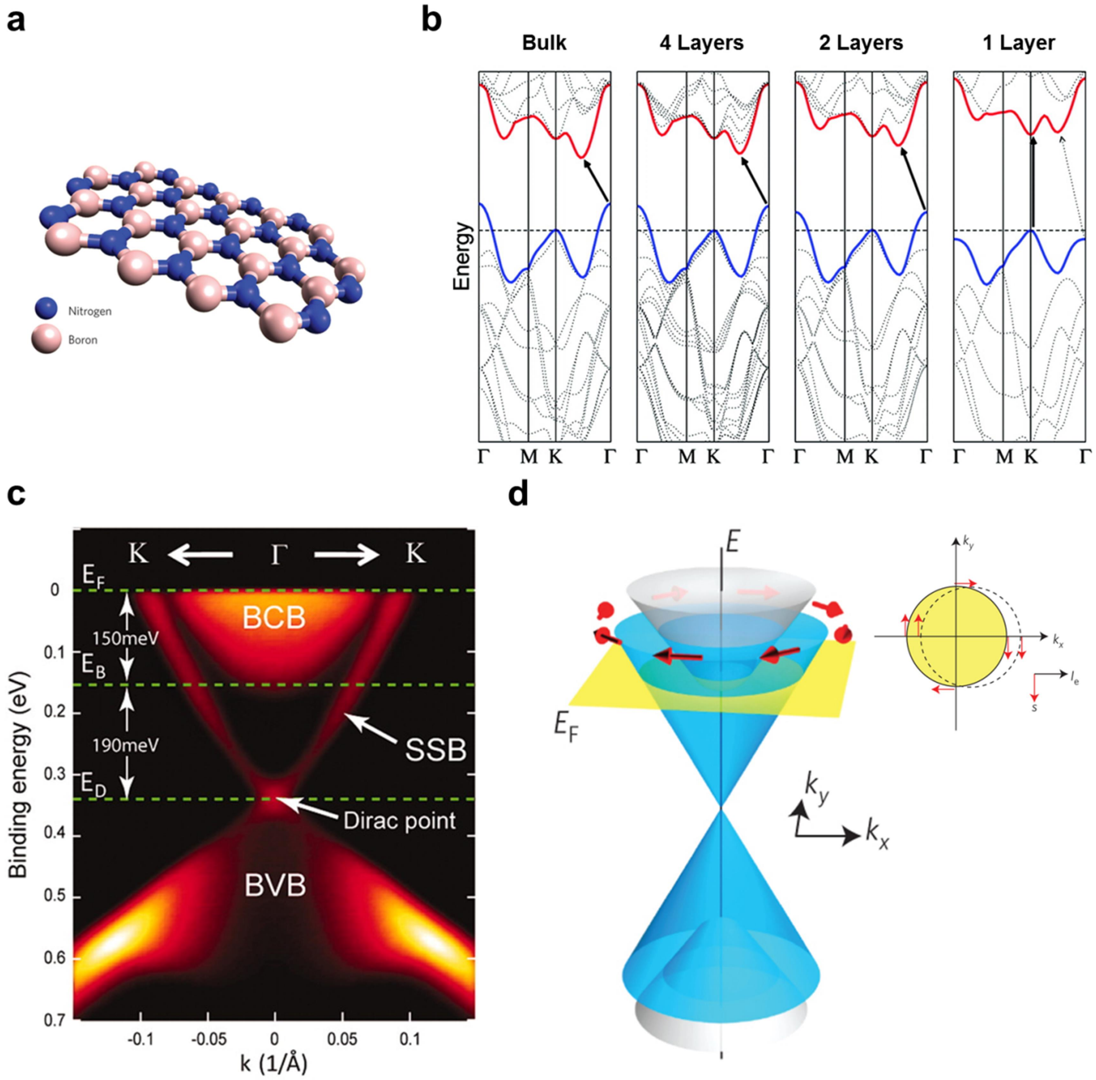

Figure 1.7 Electronic properties of vdW materials beyond graphene. a, Atomic structure of *h*-BN. Boron and nitrogen atoms form a honey-comb lattice each occupying the A and B sublattices in the Bernal structure. **b,** Energy band diagram of MoS_2 for bulk material and 4 layer, bilayer and monolayer cases exhibiting a transition from indirect to direct bandgap. **c,** Energy band diagram of Bi_2Se_3 measured using Angle-Resolved Photo-Emission Spectroscopy (ARPES) showing the bulk conduction band (BCB), bulk valence band (BVB) and the surface-state band (SSB). The position of the Fermi level (E_F), the bottom of the BCB (E_B) and the Dirac point (E_D) are indicated by the green dashed line. **d,** Schematic diagram illustrating that the spin polarization is at right angles to the momentum in topological insulators. The Dirac cone of the surface states is plotted in blue, and the BCB and BVB in grey. Inset shows a top-view of the spin-momentum locking with (dashed line) and without (solid line) an applied voltage. Adapted with permission from ref. (27, 36, 45, 46). Copyright 2016 NPG, 2010 ACS, 2010 AAAS, 2014 NPG.

h-BN has an atomic structure similar to that of graphite, with the boron and nitrogen atoms occupying the A and B sublattices of the Bernal structure respectively (Fig. 1.7a)[27]. It features a wide band gap of 5.97 eV[28], a dielectric constant of 3~4, and a breakdown voltage of around 0.7 V/nm[29]. Therefore, it is one of the most heavily investigated vdW insulators to date. The *h*-BN has been successfully implemented as an atomically flat and dangling bonds free substrate for graphene and other vdW materials based devices[30]. It has also been used as a gate dielectric[31]. In both cases, substrate induced degradation of transport properties for vdW materials are reduced by the use of *h*-BN. Tunneling through the *h*-BN has also been explored[32], and vertical transistors based on the resonant tunneling process through graphene/ *h*-BN/graphene junctions have been demonstrated[33].

TMD materials and black phosphorus are among the most widely reported vdW semiconductors to date. They feature band gaps that are sensitive to the number of vdW layers. For instance, the band gap is 1.29 eV for bulk MoS_2, but increases to 1.9 eV for monolayer[34]. For black phosphorus, the bulk band gap is around 0.3 eV, while for monolayer it is 2 eV[35]. MoS_2 exhibits an interesting transition from indirect to direct band gap when thinned down to monolayer. Density function al theory (DFT) calculations of the MoS_2 band structure is shown in Fig. 1.7b for bulk, 4 layer, 2 layer and monolayer MoS_2[36], and the indirect to direct band gap transition is reproduced. The conduction band states at K point arises from the strongly localized *d*-orbitals of Mo, which exhibit minimal interlayer coupling. As a result, the direct excitonic transition at K point does not vary with the layer thickness significantly. On the other hand, the bottom of the conduction band near Γ point stems from a linear combination of the *d* orbitals of Mo and the antibonding p_z orbitals of S atoms, which is sensitive to the layer thickness as each vdW layer is made up of a S-Mo-S unit. For the indirect transition from the top of the valence to the conduction band states near Γ point, the energy gap increases with decreasing layer number dramatically, until it exceeds the direct transition at K point for monolayer, hence the observed transition. Similar phenomenon is observed in other TMD materials[37], making them promising materials in opto-electronic applications[34].

Semiconducting vdW materials are applied as the channel materials of field effect transistors (FETs), with high on-off ratios (up to 10^8)[38], and adequate mobilities (up to 1000 cm_2/Vs for black phosphorus[10]). Many other device concepts are being explored, such as valleytronics[39, 40], which utilizes the degenerate but inequivalent valleys in momentum space. Ising superconductivity is observed in ionic liquid gated MoS_2[41, 42], and characteristics of a charge density wave is observed in $MoSe_2$ related to the mirror twin boundaries[43].

A new class of vdW materials have recently been gaining immense interest, especially in the physics community: the topological insulators including Bi_2Se_3, Bi_2Te_3 and their doped counterparts[44]. Bi_2Se_3 has a bulk band gap of around 0.3 eV, but due to the strong spin-orbital coupling (SOC) in this material, band inversion takes place, resulting in the generation of topologically protected surface states at the boundary of topological insulator/vacuum or ordinary insulators[45]. This unique band structure can be observed using Angle-Resolved Photo-Emission Spectroscopy (ARPES), as shown in Fig. 1.7c, and the Dirac cone feature related to the gapless surface states is clearly visible. As a result, electrons propagating at the surface act like massless Dirac fermions and are immune to back scattering from non-magnetic impurities due to the protection of the time reversal symmetry. Spin-momentum locking is also observed for these surface electrons due to the giant SOC, with the spin always at right angles to the momentum (Fig. 1.7d)[46]. As a result, dissipation-less helical spin-polarized conductor is observed in the quantum spin Hall measurement[47, 48]. Many other interesting and sometimes illusive physical phenomena have been observed in this intriguing class of materials, including Shubnikov-de Haas oscillations[49], Aharonov-Bohm effect[16] and quantum anomalous Hall effect in magnetically doped topological insulators[50].

1.3 Vertical Transport of vdW Materials

Due to the anisotropy in the atomic structure of vdW materials, carrier transport in the out-of-plane direction is expected to be markedly different from that of the lateral direction (which is the focus of the previous section). Meanwhile, vertical transport of carriers through vdW materials is a process inherent to all vdW devices, thus, it has rapidly emerged as one of the most interesting topics in the vdW material research field. In this section, various transport processes and device concepts that highlight vertical transport of carriers through vdW materials and the vdW gaps are reviewed.

1.3.1 Vertical Tunneling into vdW Materials

Due to the presence of the vdW gap, it is expected that carrier injection into the vdW material is different from that of a material with 3D crystal lattices. A simplified version of this problem is electron tunneling through a small distance in vacuum into a vdW monolayer, for example, graphene. Here, the vacuum gap could affect the electron transport similarly to the vdW gap. This experiment can be performed using the scanning tunneling microscopy (STM), in which a tunneling current between a metal tip and the sample (in this case, the vdW material) separated by a vacuum gap of around 4 Å is measured[51]. The experimental setup commonly adopted for the measurement of graphene is shown in 1.8a. The graphene is supported by an insulating substrate (such as SiO_2 or BN), and electrodes are fabricated to form ohmic contacts with the graphene flake[52]. Electrons injected by the metal tip tunnel vertically through the vacuum gap and reach graphene, where energy and momentum relaxation takes place so that the electrons can propagate laterally within graphene and are collected by the electrode. An example of the measured conductance (*dI*/*dV*) as a function of the applied bias *V* is shown in Fig. 1.8b, a threshold bias is observed in the tunneling process. Above the threshold voltage, the V-shape DOS of graphene can be identified in the *dI*/*dV*-*V* curve, indicating that the tunneling current in this region is limited by the small DOS of graphene. Gate dependence of the position of the V-shape feature further supports this theory.

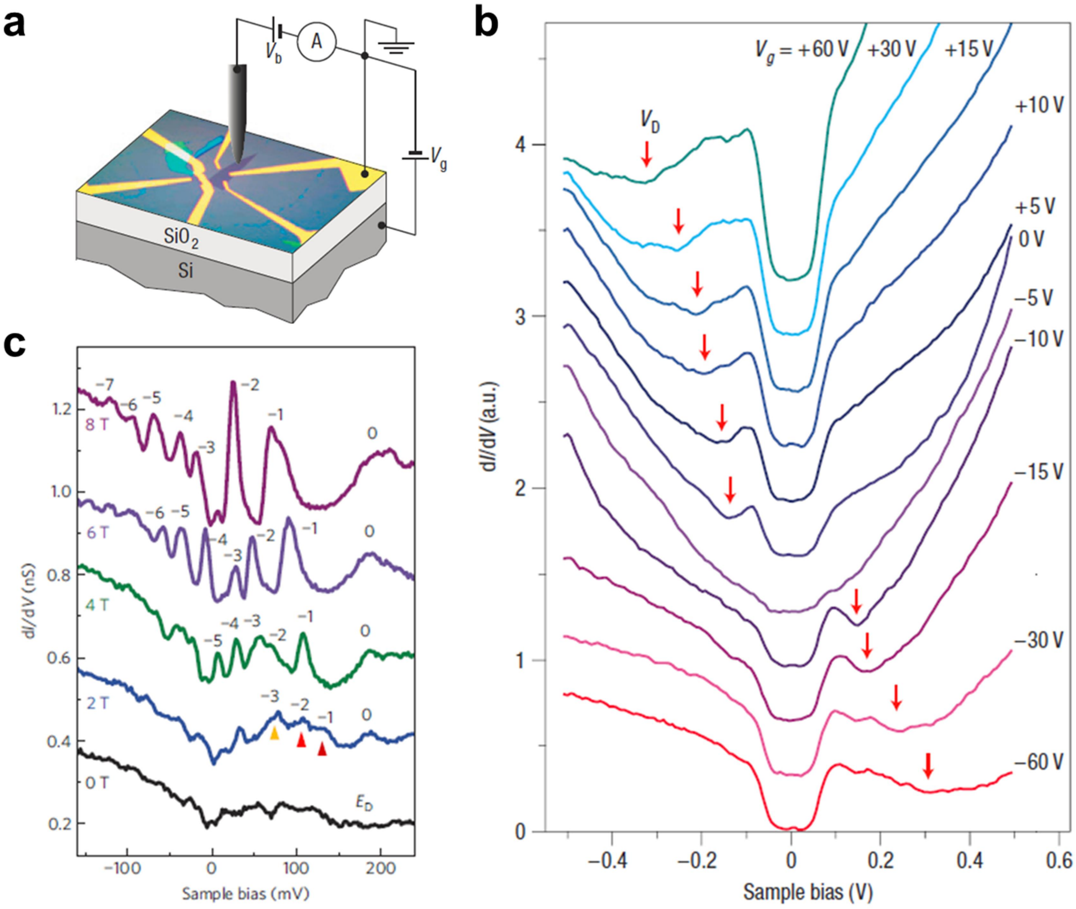

Figure 1.8 STM measurement of electron tunneling into graphene. a, Measurement setup for the STM measurement of graphene. **b,** Conductance as a function of sample bias under various gate biases. Threshold voltages are observed independent of the gate bias, which is attributed to the onset of the phonon-assisted tunneling process. The Dirac cone feature is also observed,

which shifts monotonically as a function of the gate bias. **c,** Magnetic field dependence of the conductance showing the evolution of the Landau levels with increasing magnetic field. Adapted with permission from ref. (52, 56). Copyright 2008 NPG, 2011 NPG.

Below the threshold, the *dI*/*dV*-*V* curve deviates from the V-shape DOS of graphene; Rather, minimal conduction is observed. This is because the phonon assisted energy and momentum relaxation process is suppressed when the voltage is below the corresponding phonon energy[53]. While the existence of a single phonon threshold, as well as the threshold phonon energy remains controversial to date[54-57], the phonon-assisted process transforming vertically tunneling electrons to laterally propagating Dirac fermions have been observed universally. The Dirac fermion nature of the electrons is confirmed through magnetic field dependence measurements where the Landau level spectra are clearly observed (Fig. 1.8c)[56].

1.3.2 Vertical Tunneling through vdW Materials

Now we focus on the vertical tunneling across vdW materials, i.e., the vdW materials' role as tunnel barriers. Being a wide band gap insulator, *h*-BN is the natural choice as a vdW barrier, and the thickness dependent tunneling current is measured on exfoliated samples by Britnell *et al*. as shown in Fig. 1.9a[29]. Detail features from the tunneling current across few layer *h*-BN sandwiched by graphene/graphite as electrodes are investigated by Jung *et al*. through direct measurement of the 1st and 2nd order derivatives of the *I*-*V* characteristic, as shown in Fig. 1.9b[58]. This method is called the electron tunneling spectroscopy (ETS), as will be discussed in detail in Chapter 2, section 2.2.2. Similar to the STM measurement of graphene, the linear DOS of graphene as the electrode governs the tunneling current across the *h*-BN barrier, and various phonon modes related to the *h*-BN barrier, graphene and *h*-BN/graphene heterostructure are identified, signature of a phonon-assisted process.

A less intuitive choice of a vdW barrier, graphene, has also been investigated and the *I-V* characteristic is shown in Fig. 1.9c[59]. The tunneling nature of the graphene sandwiched between two metal electrodes stem from the vdW gaps formed on both sides of graphene. The graphene is applied as a tunnel barrier for magnetic tunnel junctions where spin polarized tunneling is realized.

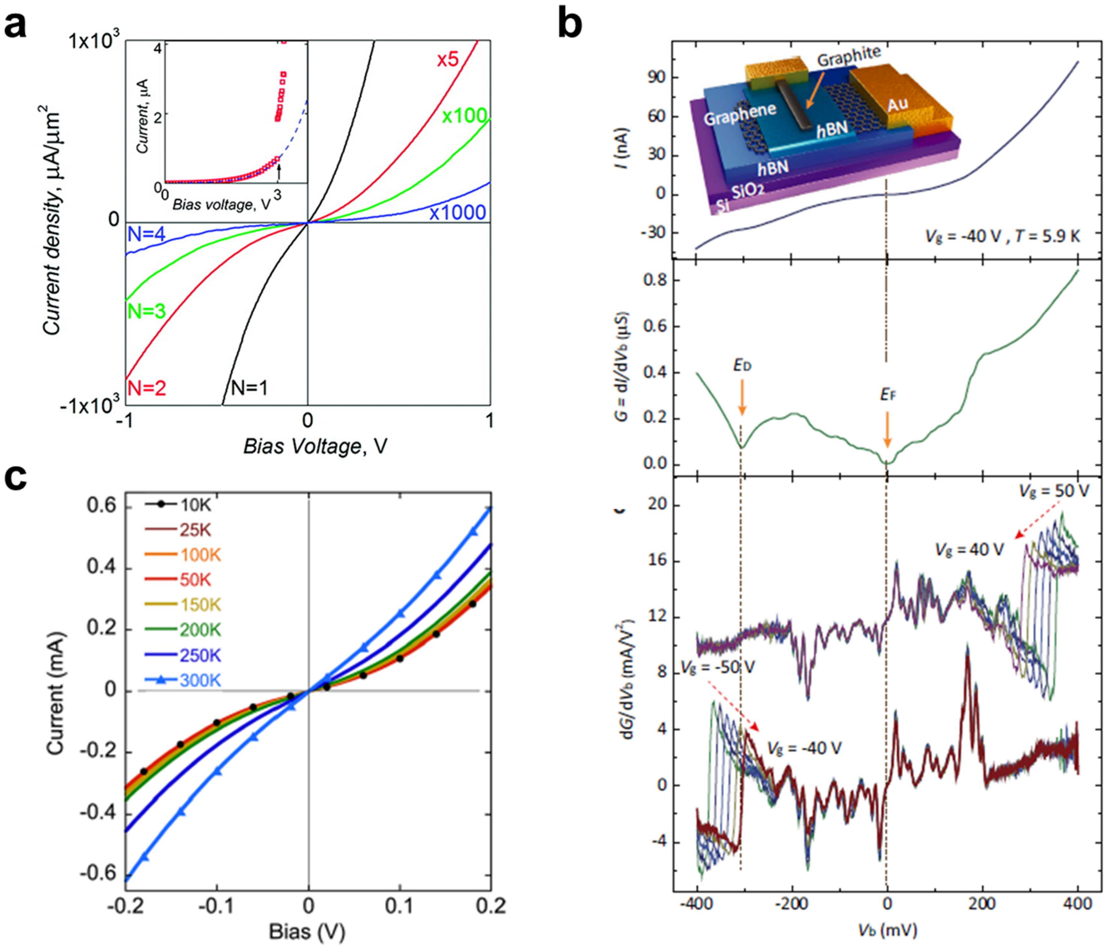

Figure 1.9 vdW materials as tunnel barriers. a, Current density-voltage (*J-V*) characteristics of vertical tunneling through *h*-BN with different layer thicknesses. Inset shows the breakdown characteristic of 4 layer *h*-BN. **b,** ETS of few layer *h*-BN. Top panel: *I-V* characteristic of the tunneling across few layer *h*-BN. Inset of top panel: Schematic diagram illustrating the structure of the *h*-BN tunneling device. Middle panel: 1st order ETS of the *h*-BN tunnel structure showing signature of the Dirac cone feature. Bottom panel: 2nd order ETS of the *h*-BN tunnel structure with different applied gate voltage. Peaks corresponding to the Dirac cone, as well as the phonon

modes of graphene, *h*-BN and graphene/ *h*-BN heterostructure are observed. **c,** Temperature dependent *I-V* characteristics across the metal/graphene/metal tunneling structure. Adapted with permission from ref. (29, 58, 59). Copyright 2012 American Chemical Society (ACS), 2015 NPG.

1.3.3 Metal Contacts to vdW Materials

Aside from vdW material based tunneling structure and devices, the out of plane transport behavior of vdW materials are present in all vdW material based devices, one important example is metal contacts to vdW materials. Creating ohmic contacts with a small contact resistance is a universal topic for any materials' application in electronic devices. According to the International Technology Roadmap for Semiconductors (ITRS), a contact resistance as low as 0.3-0.5 kΩ μm has been achieved for metal-silicon contacts in CMOS technology[60], and this number is commonly cited as the standard to evaluate the contact resistance to next generation semiconductor materials.

In traditional contacts to bulk semiconductors, a low contact resistance is often achieved through creating a highly doped contact region (such as through ion implantation), however this method is inapplicable for vdW materials with the thickness of only a few atomic layers. In addition, analogous to the tunneling phenomenon discussed in Section 1.3.1, electrons injected from the metal contact will need to traverse the vdW gap into the vdW material, then propagate laterally through the vdW material. Hence, physics governing the contact resistance of metal contact to vdW materials could be very different from that of conventional 3D contacts.

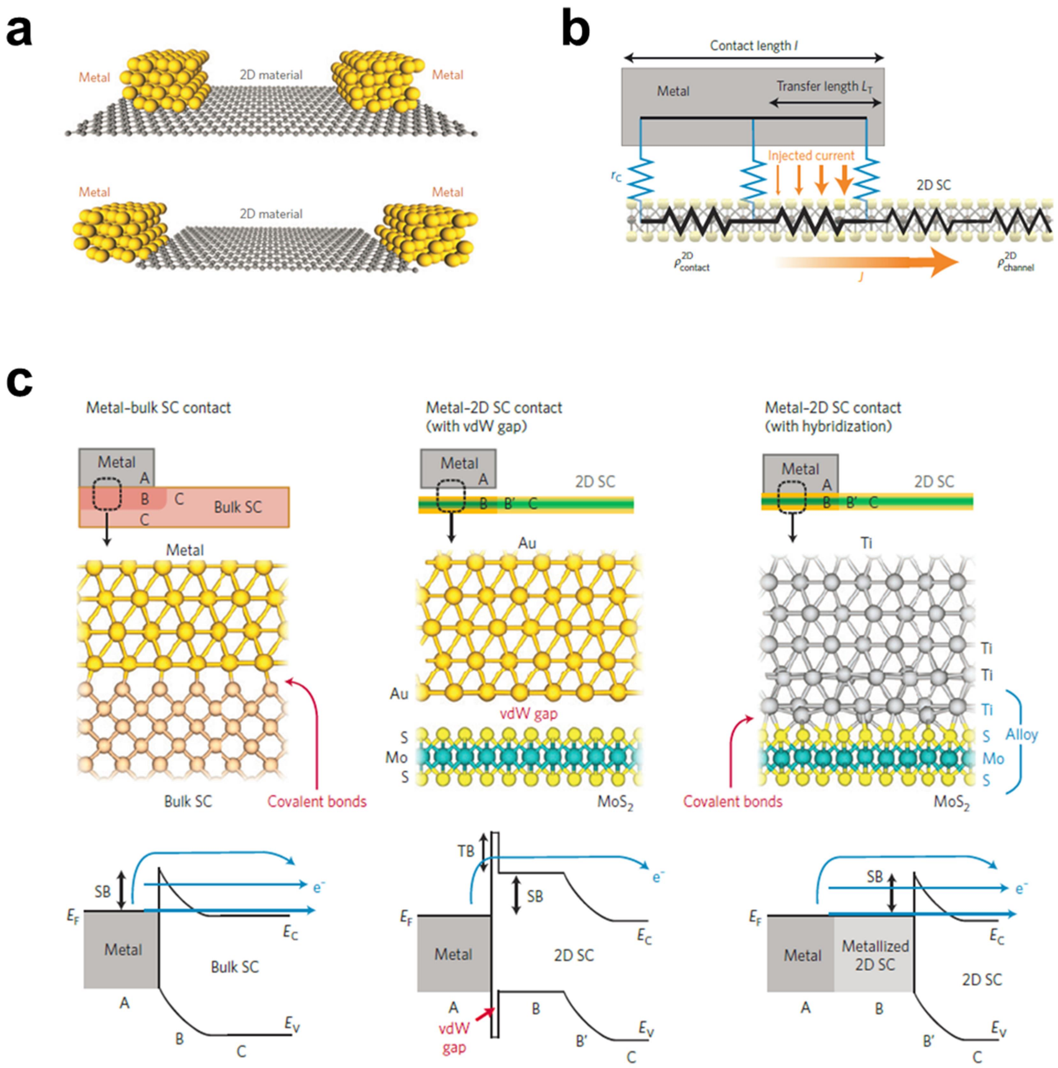

Figure 1.10 Metal contacts to vdW materials. a, Schematic diagram illustrating the difference between top and edge contact. **b,** Transmission line model of metal contacts to vdW materials. Orange arrows illustrate the flow of current. Current crowding occurs at the contact edge. **c,** Schematic diagram showing the device structure, the atomic structure and band structure of metal contacts to 3D materials (left panel), vdW materials without hybridization with the metal contact (middle panel) and vdW materials with hybridization to the metal contact (right panel). Adapted with permission from ref. (61). Copyright 2015 NPG.

Two distinct contact geometries can be identified for metal contact to vdW materials: the 'top contact' and 'edge contact'[61], illustrated in Fig. 1.10a. Realistic contacts are more often than not a combination of the two, and the trajectory of the carriers can be analyzed using a transfer line model[62] (Fig. 1.10b). In a recently published review paper by Allain *et al*., metal contacts to semiconductors are summarized into three categories[61], as shown in Fig. 1.10c. Left panel shows metal contacts to bulk semiconductors characterized by the atomic bonding between the semiconductor and the metal, and a Schottky barrier is generally formed. The middle panel plots metal contact to vdW materials without hybridization between the two materials, and a vdW gap is preserved. When electrons are injected from the metal contact into the semiconductor or vice versa, both the Schottky barrier and the vdW gap as an additional barrier needs to be taken into account. The right panel illustrates metal contacts to vdW materials with hybridization between the two, so that the vdW gap is eliminated or only partially preserved. In this case the transport properties of electrons could be seen as an intermediate state between the latter two cases. As a result, metal contact to vdW materials are found to depend significantly on whether hybridization could occur, rather than the work function of the metal.

Many methods on improving the metal contacts to vdW materials have been reported. Wang *et al*. reported edge only contact to *h*-BN encapsulated graphene to avoid the resistive vertical transport into graphene[63]. Metals that are prone to hybridization with the outer atoms of the vdW materials are chosen to promote a lower contact resistance[64, 65]. Thermal annealing treatments have been used to enhance the adhesion between the metal and the vdW materials[38, 66]. For TMD materials, an additional method have been reported, where the 2H-phase of the TMD material (semiconducting) are transformed into 1T'-phase (metallic) to improve the contact[67].

1.3.4 vdW Material Based Vertical Devices

Recent years saw continued advancements of fabrication processes to create vdW heterostructures with dangling bonds free interfaces, i.e., the vdW gaps in between. Therefore, there has been increasing interest in novel device concepts of vertical vdW devices. This includes atomically thin transistors and diodes, highly efficient optoelectronic devices, as well as components of spintronics.

Resonant tunneling diodes have been realized for graphene/X/graphene (X is a vdW material acting as a barrier, such as *h*-BN[68]), as well as TMD heterostructures[69]. Demonstration by Mishchenko *et al*. using stacked graphene/ *h*-BN/graphene is shown in Fig. 1.11a. This device utilizes the fact that tunneling between the two graphene electrodes is limited by the linear DOS, and with the presence of a crystallographic twist angle between them, a resonance in the *J-V* characteristic is observed, corresponding to the condition in which the momentum and energy is conserved at this bias. Departing from the resonant bias, the current density drops as a result of the momentum mismatch, and therefore a phonon assisted process is required. The resonant peak position can be tuned by applying a gate voltage, as shown in the right panel of Fig. 1.11a for three gate biases. The application of this resonant diode as a radiofrequency oscillator is demonstrated, with MHz response.

In an almost identical structure, the tunneling current across graphene/ *h*-BN/graphene[33] and graphene/WS_2/graphene junctions can be effectively tuned using gates as tunnel FETs (TFETs)[20]. Similar demonstrations are achieved utilizing band-to-band tunneling (BTBT), with the most successful demonstration reaching a subthreshold swing of below 30 mV/dec[70], lower than theoretical values for that of MOSFETs (60 mV/dec). This is shown in Fig. 1.11b, where BTBT through the Ge (p^{++})/MoS_2 junction can be controlled through the gate voltage. Another device concept based on the vertical tunneling process is the hot electron transistors (HETs), as will be discussed in detail in the next section (1.4), and is the focus of Chapter 4 of this thesis.

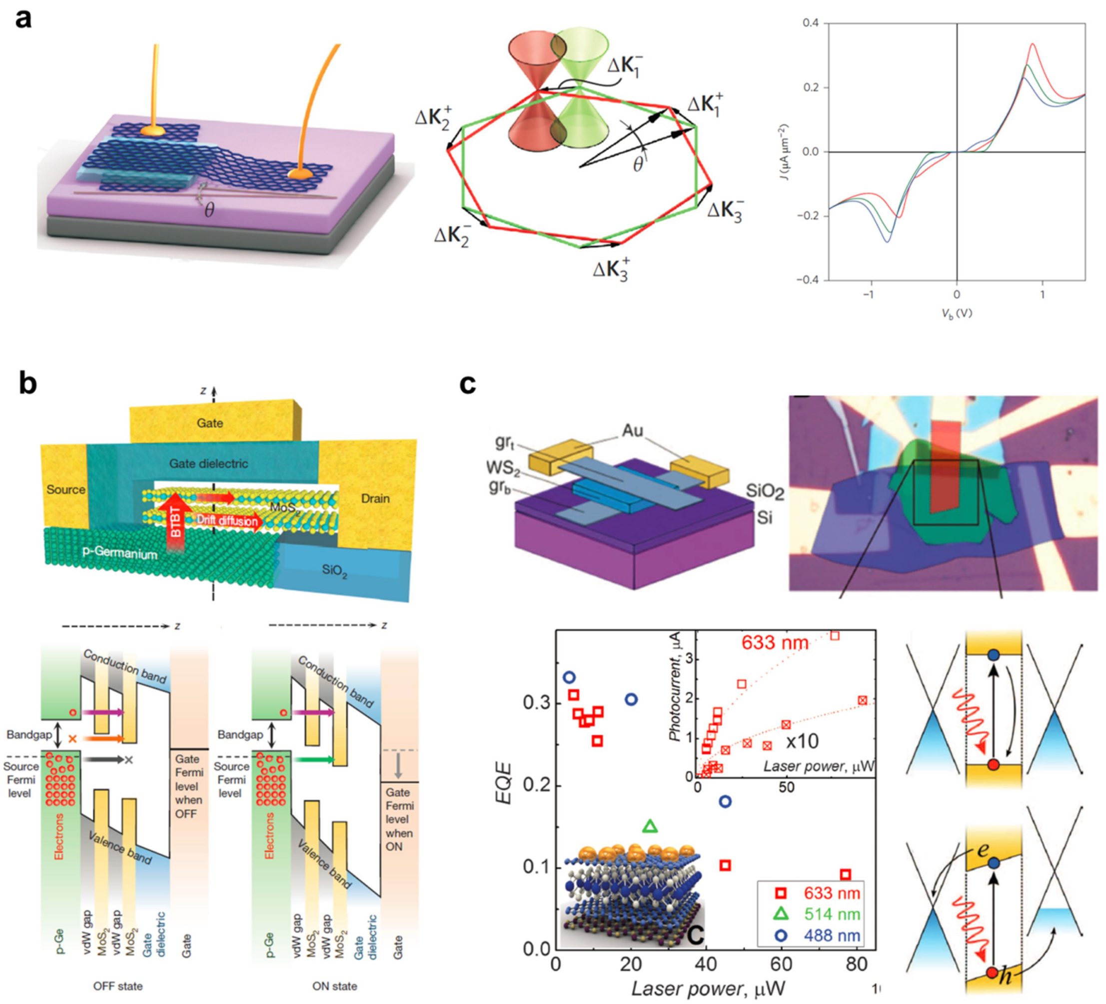

Figure 1.11 VdW materials based vertical devices. a, The device structure, schematic diagram and *J-V* performance of graphene/*h*-BN/graphene resonant tunneling diodes. **b,** The device structure and energy band diagram of MoS_2 based tunnel FETs. **c,** The device structure, optical microscope image, external quantum efficiency and photocurrent as a function of laser power, as well as the energy band diagram of atomic graphene/WS_2/graphene heterostructures with enhanced photo-responsively. Adapted with permission from ref. (33, 70, 71). Copyright 2014 NPG, 2015 NPG, 2013 AAAS.

Vertical optoelectronics have been demonstrated with atomically sharp interfaces and junctions. These devices take advantage of the strong light-matter interaction of vdW materials, as a result of the van Hove singularities of 2D systems[23, 71]. Charge separation, recombination and transport take place within the vdW gaps, but whether these processes are strongly affected by the presence of the vdW gaps remains elusive. The strong photo-response from TMD material WS_2

is measured using a vertical heterostructure graphene/WS_2/graphene by Britnell at el (Fig. 1.11c)[71]. The application of graphene as the electrodes in this structure makes the photo-response gate tunable, and the responsivity is high considering the atomic thickness of the vertical stack.

1.4 vdW Materials for Novel HETs

There has been significant interest in using vdW materials to replace the conventional metal base region in HETs, to take advantage of the short transit time across these atomically thin materials. The HET is operated by controlling a flow of hot electrons from the emitter to the collector by varying the base potential. The HETs are similar to bipolar junction transistors (BJTs) in terms of device structure and equivalent circuit. The continued interest towards this device structure is fueled by the hopes of producing a device that is faster than the BJTs[72].

For conventional BJTs, the speed of the transistor depends critically on the base region. The cut-off frequency, f_T, is given as:

$$f_T = \frac{1}{2\pi\tau_{EC}} \tag{1.4}$$

in which τ_{EC} is the sum of the time needed for the electron to traverse the emitter, base and collector region: $\tau_{EC} = \tau_E + \tau_B + \tau_C$. $\tau_B$is the base transit time and is defined as the thickness of the base region divided by the vertical speed of the electrons $\tau_B = d_B/v$. Therefore when only considering f_T, a smaller base thickness is desired. Another important figure of merit to characterize the speed of a BJT is the maximum oscillation frequency, f_{max}, defined as:

$$f_{max} = \frac{1}{2}\sqrt{\frac{\alpha f_T}{2\pi R_B C_C}} \tag{1.5}$$

in which α is the common base current gain, R_B is the base resistance, and C_C is the collector-base capacitance. To achieve a larger f_{max}, a smaller R_B is needed, which means a thicker base region. Thus, there exists a trade-off on the base region thickness for BJTs and devices resembling the BJTs, limiting its maximum speed. τ_B can also be reduced by increasing the electron speed, v, and eliminating scattering events during transport, i.e., ballistic transport through the base region. Under these circumstances, the velocity of the carrier is solely determined by the initial velocity at which the electrons are injected, which in turn is dependent of the design of the emitter-base barrier. This motivates investigation of the HET structure, as in this structure motion of the hot electrons within the base region is characterized by ballistic transport.

1.4.1 A Brief History of HETs

The first HET is experimentally demonstrated by Mead in 1960[73], using a metal-oxide-metal-oxide-metal (MOMOM) structure (Fig. 1.12a). The α is small for this structure, as a result of the high quantum mechanical reflection at the base/filter barrier interface, as well as the short mean free path of electrons in the metal base. An alternative structure is investigated by Spratt *et al.*, replacing the second oxide barrier with a Schottky barrier, resulting in a metal-oxide-metal-semiconductor (MOMS) structure (Fig 1.12b)[74]. A slight increase in α is observed, but still, it is limited by the relatively short mean free path of electrons in the metal base, the difficulty of achieving a pin-hole free and thin metal base layer, as well as the poor control over the uniformity of the thin tunnel barrier.

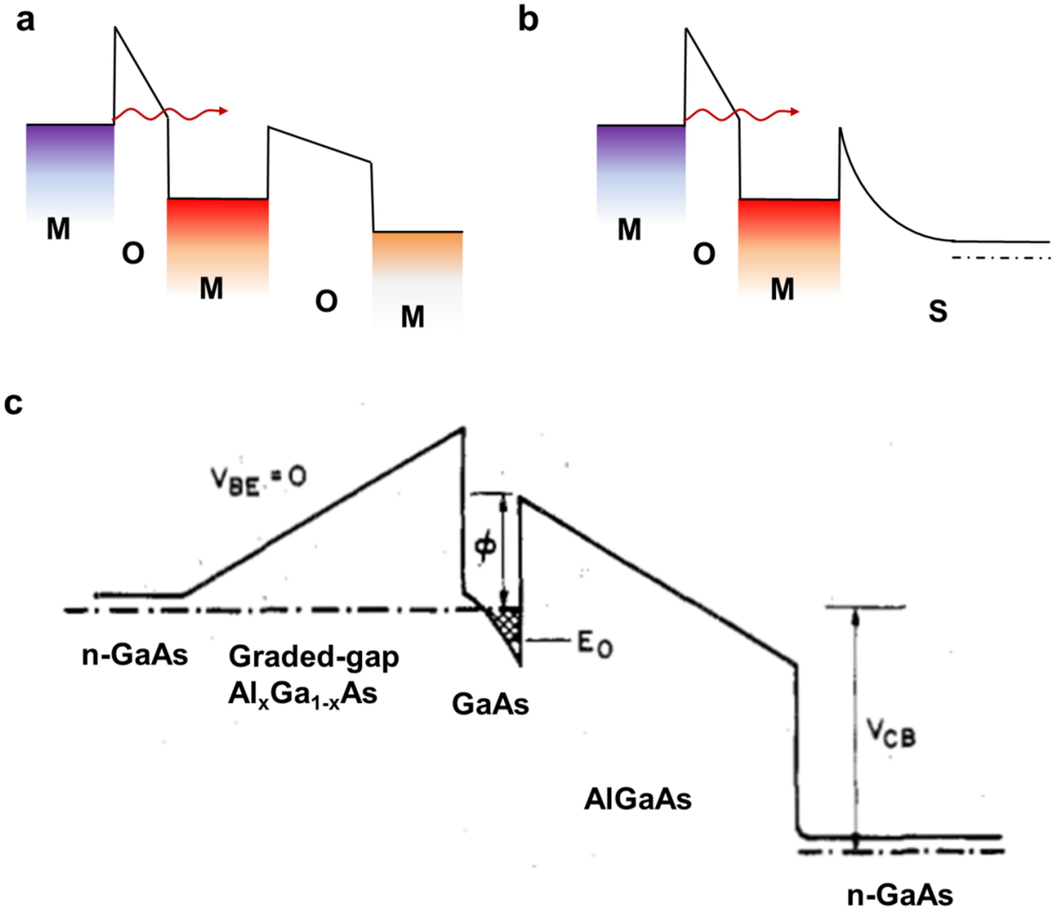

Figure 1.12 Device structures of various variations of HETs. a, The MOMOM HET structure. This was the first structure investigated as a HET. **b,** The MOMS HET structure. **c,** The tunneling hot electron transfer amplifier (THETA) structure grown using MBE. Adapted with permission from ref. (77). Copyright 1986 Institute of Electrical and Electronics Engineers (IEEE).

In 1981, Heiblum analyzed past works on HETs and proposed the tunneling hot electron transfer amplifier (THETA) structure[75]. Device structures consisted entirely of MBE grown epitaxial III-V semiconductors was proposed to avoid pin-hole formation[76], and the term THETA is sometimes used to refer to this particular type of HETs. One of the most successful demonstrations uses GaAs/AlGaAs heterostructures to create HETs with a high α of 96 % (as shown in Fig. 1.12b). In this case the base region is the 2D electron gas (2DEG) formed at the

GaAs/AlGaAs interface[77].

1.4.2 vdW Materials for Improved HETs

Graphene's unprecedented high mobility has triggered excitement on its application in high speed electronics. Its lack of a band gap, however, greatly limits its potential application as the channel material in CMOS technology. As a result, Mehr *et al*. investigated the possibility of graphene based vertical transistor using theoretical calculations and THz performance is predicted[78].

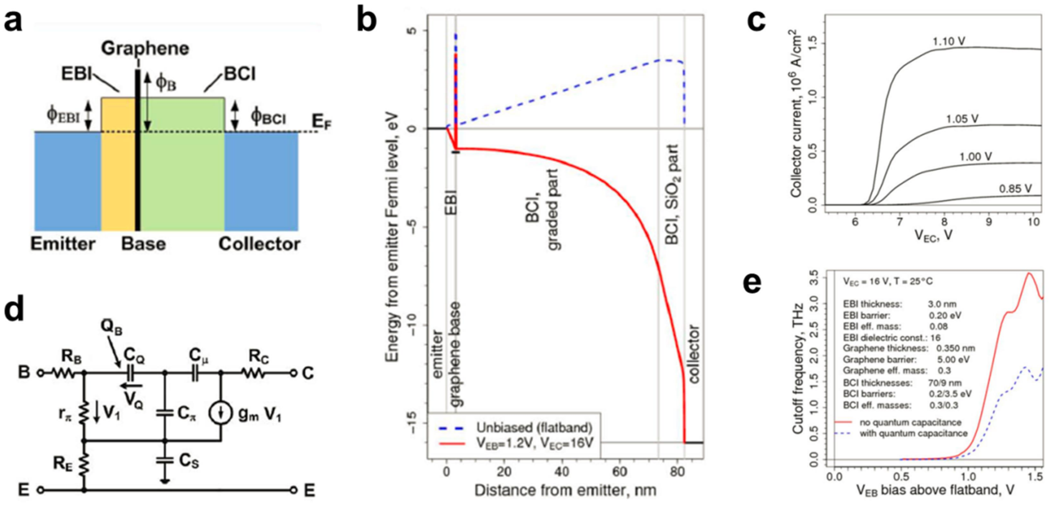

Figure 1.13 Theoretical calculation of graphene based HETs. a, Schematic diagram of the calculated device structure consisting of the emitter, emitter-base insulator (EBI), graphene as the base region, the base collector insulator (BCI) and the collector. The graphene is treated as a barrier in the vertical transport of electrons. **b,** High frequency equivalent circuit of the graphene based HET. R_E, R_B , R_C are the emitter, base and collector resistance respectively. r_π is the differential resistance of the EBI. C_π and C_μ are the capacitance of EBI and CBI respectively. $C_Q$is the quantum capacitance of graphene, and $C_S$is the substrate capacitance. **c,** Calculated band diagrams of the graphene based HET in thermal equilibrium (blue dashed line) and the on state (red line). **d,** Calculated common emitter characteristic. **e,** f_T as a function of the emitter bias (V_{EB}) characteristic with (blue dashed line) and without (red line) considering the quantum capacitance of graphene both showing THz response. Adapted with permission from ref. (78). Copyright 2012 IEEE.

In view of the trade-off between the d_B and R_B for HETs, graphene is the perfect choice, with its atomic thickness and low sheet resistance. Fig. 1.13a shows the device structure used for the calculation, with graphene as the base material. The calculated band diagram is shown in Fig. 1.13b for thermal equilibrium and on state. Note for vertically propagating electrons, graphene acts as a barrier, instead of the semi-metal commonly observed for lateral transport. The calculated output characteristics are shown in Fig. 1.13c for an EBI with a thickness of 0.35 nm and a barrier height of 5 eV. The high frequency equivalent circuit (Fig. 1.13d) takes into account the contact resistance of the emitter (R_E), base (R_B) and collector (R_C), as well as the differential resistance and capacitance of the emitter-base insulator (EBI) (r_π , C_π) and the base collector insulator (BCI) (C_μ). The quantum capacitance of graphene, C_Q, defined as $C_Q = \partial Q_B / \partial V_Q$, in which Q_B is the charge accumulated in graphene, and V_Q is the Fermi level of graphene, can be incorporated. Using this model, the f_T can be calculated, and is shown as a function of V_{EB} in Fig. 1.13e. Incorporating the quantum capacitance decreases the f_T considerably, but THz f_T is still obtained.

Our group is one of the first groups to experimentally demonstrate HETs with graphene as the base material[79]. In this structure, highly doped n-type silicon, Si (n^{++}), is chosen as the substrate as well as the emitter electrode. Thermal oxide grown on top of the Si (n^{++}) is chosen as the EBI or tunnel barrier, metal oxide layer deposited using atomic layer deposition (ALD) as the BCI or filter barrier, and metal is used as the top collector electrode. This paper highlight the importance of choosing an appropriate filter barrier height, ϕ_C, with a ϕ_C equals 3.3 eV (for Al_2O_3) resulting in an α of 1.2 %, and when the ϕ_C is decreased to 2.0 eV (for HfO_2), α is creased to 4.8%. Similar demonstration is reported by the Lemme group as well[80]. Later reports using single layer MoS_2 as the base material led to a staggering increased α (95 %), and a β of around 4, however partly due to the high resistivity of the MoS_2 material and its contacts, the injection current is limited to a sub-nA level[81, 82]. Novel dielectric combinations have been investigated to replace SiO_2 as the tunnel barrier, resulting in the highest injection current density to date[83], with a emitter current density close to 10 A/cm^2 and an α of around 20 %.

While still in its infancy, vdW material based HETs have seen significant progress in terms of its current density level, as well as its current gain. This is also a unique platform to study the vertical transport of carriers across vdW materials, as well as carrier transport at vdW material/metal oxide interfaces. Another exciting opportunity is to construct an all-vdW material HET, which is currently limited by the ability to grow large area and pin-hole free vdW insulators.

1.5 Synopsis

This dissertation addresses the fundamental physics of the vertical tunneling of electrons into and across vdW materials and its potential application in HETs. The chapters are arranged as following:

Chapter 2 focuses on the fundamental process of electron tunneling through the vdW gap and into the vdW material using graphene as the model material. A fully preserved vdW gap is retained at the interface of the hydrogen terminated silicon and the graphene, which acts effectively as a tunnel barrier. After tunneling into graphene, the electrons are forced to propagate laterally within the basal plane of graphene. Thus the tunneling flux is governed by the linear DOS of graphene shown via low temperature ETS.

Chapter 3 explores the vertical tunneling across vdW materials, with the lateral transport eliminated by sandwiching the vdW material between two vertically aligned electrodes. The vertically propagating electrons interact weakly with the in-plane band structure of graphene, as a result of the transverse momentum mismatch. The vertical transport across vdW materials is described using a modified Simmon's direct tunneling model and a capacitance model taking into account the 2D nature of the graphene and the quantum capacitance.

Chapter 4 investigate a potential application for the vertical tunneling process of graphene discussed in Chapter 2 and 3, by applying graphene as the base material of HETs, and Si-graphene contact as the emitter-base junction. Improved injection current is achieved using this structure, with a turn-on voltage close to the filter barrier height.

Finally, a conclusion is given in Chapter 5, followed by suggested work for further research in this field.

Chapter 2 Vertical Tunneling into Graphene through the vdW Gap

2.1 Motivation

Quantum manipulation and control over charge carrier and spin transport are at the forefront of the development of next generation electronics and computing systems, in particular the transport across interfaces and heterojunctions. Since the successful isolation of graphene in 2004[1], the emergence of vdW materials has brought the construction of quantum heterostructures to new frontiers with precise manipulation and control down to the atomic level. vdW materials featuring dangling bond free surfaces are ideal to be stacked together with well controlled interfaces (that is, vdW gaps) in between[12]. Electron tunneling in vdW materials is a process inherent to all vdW devices, and thus, it has rapidly emerged as one of the most interesting topics in the vdW material research field. This process has led to the realization of novel electronic devices, including resonant tunneling diodes[33], tunnel field effect transistors[70, 84], hot electron transistors[78, 79, 81, 82], optoelectronic devices[85-87], as well as spintronic applications[59, 88, 89].

So far, the majority of research on the tunneling processes of vdW materials focus on electron tunneling into vdW materials through an artificial gap[52, 55, 90-92]. Following vertical transport across the tunnel barrier, carriers are collected by the vdW materials and transport laterally along the 2D plane and thus the band structure of the vdW materials as well as the carrier interaction with elementary excitations can be studied. In such scenarios, the vertical tunneling process is coupled with the lateral dispersion relationship of the band structure of the vdW materials; hence the in-plane band structure can explain most of the experimental observations. In particular, the Dirac cone picture is widely used to explain the experimental phenomena in reports of graphene, such as the linear DOS [90, 91], magnetic field induced Landau levels splitting[56], and the formation of charge puddles[54, 92] etc. These works take advantage of the dangling bond free surfaces of vdW materials in the construction of vertical heterostructures. However, the role of the vdW gaps during the tunneling process, and the effect of the 2D nature of the vdW materials to the vertical transport behavior remain elusive.

In this chapter, we study the important process of tunneling through the vdW gap that is inherent to all vdW materials based device structures using graphene as the model material. It is found that a fully preserved vdW gap is retained at the interface of the hydrogen terminated silicon and the graphene. Thus injection through the vdW gap leads to a quantum tunneling behavior for vertically propagating electrons, followed by lateral propagation within the basal plane of graphene. Using low temperature ETS, the coupling between the out-of-plane injection and in-plane transport is studied.

2.2 Experimental Details

2.2.1 Fabrication Process Flow of the Tunneling Structure

To study the process of electron tunneling into graphene, n-type degenerately doped Si (n^{++}) with a doping concentration of 10^{19} cm^{-3} is used as the substrate, as well as one of the tunneling electrodes. Si is chosen as one of the electrodes, instead of metal, due to its ease of forming an atomically flat surface, to avoid puncture of the monolayer graphene. To isolate each individual device, and to achieve a well-defined carrier injection region, patterned field oxide (FOX) is deposited using the local oxidation of silicon (LOCOS) method, and the details of this process is given in the following paragraphs.

Si (n^{++}) substrates are first loaded into an oxidation furnace (Tystar) to deposit 50 nm of SiO_2 (Fig. 2.1a). This layer of SiO_2 serves as a pad oxide layer for the subsequent growth of Si_3N_4. The Si_3N_4 layer is deposited using plasma-enhanced chemical vapor deposition (PECVD, Plasmatherm 790) to a thickness of 250 nm (Fig. 2.1b), and then patterned using photolithography and an Advanced Oxide Etcher (AOE, STS MESC Multiplex) into disks, which defines the carrier injection region of exposed Si (n^{++}) (Fig. 2.1c). The substrate with the patterned Si_3N_4 is then transferred into an oxidation furnace at 1050°C for 50 mins, resulting in a 530 nm FOX layer deposited in regions not covered by the Si_3N_4 (Fig. 2.1d). An image of the substrate after the FOX deposition is shown in Fig. 2.1e, with each dot representing one device with the Si_3N_4 protection layer on top. The purple region corresponds to the FOX separating individual devices.

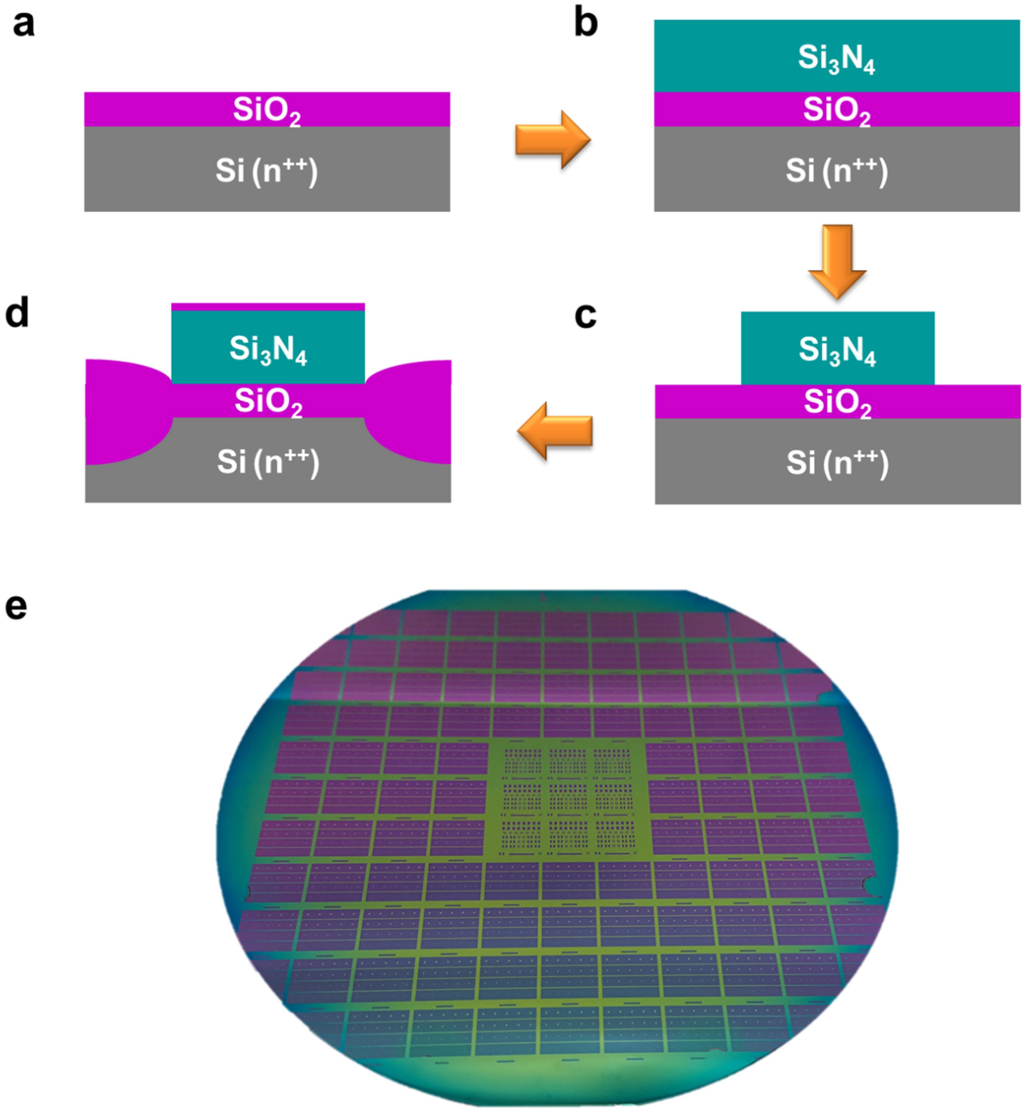

Figure 2.1 Fabrication flow for patterned Si_3N_4 as the mask for the LOCOS process. a, Schematic diagram showing the pad oxide grown on top of the Si (n^{++}) substrate. **b**, Schematic diagram showing the Si (n^{++}) substrate after the deposition of Si_3N_4 using PECVD. **c**, Schematic diagram showing the Si_3N_4 mask patterned using photolithography and AOE. **d**, Schematic diagram showing the Si (n^{++}) substrate after the thermal oxidation process, with thick FOX grown in regions not covered by the Si_3N_4 mask. **e**, Image of the Si (n^{++}) substrate after the FOX deposition. Each dot corresponds to one carrier injection electrode covered by the pad oxide and the Si_3N_4 disk. The FOX separating individual electrodes can be identified by the purple color.

To expose the Si (n^{++}) which serves as one of the tunnel electrode, the substrate is first treated with buffered oxide etch (BOE 6:1) to remove the oxide layer formed on top of the Si_3N_4 layer during the high temperature growth of the FOX. The substrate is then immersed in 85 % H_3PO_4 at 155°C for 2 hours to fully remove the Si_3N_4 mask (Fig. 2.2a). This is followed by 60 s of BOE treatment to remove the pad oxide, exposing bare Si (n^{++}) for carrier injection (Fig. 2.2b). Fig. 2.2c presents an image of the substrate, and an optical micrograph of four injection regions (grey dots) is shown in Fig. 2.2d. Each exposed Si (n^{++}) region is isolated by the FOX (light green region in the optical micrograph), and the thickness of the FOX is measured to be around 370 nm. This patterned Si substrate in Fig. 2.2c and 2.2d serves as the basis for all the tunneling structures and HET devices presented in this thesis.

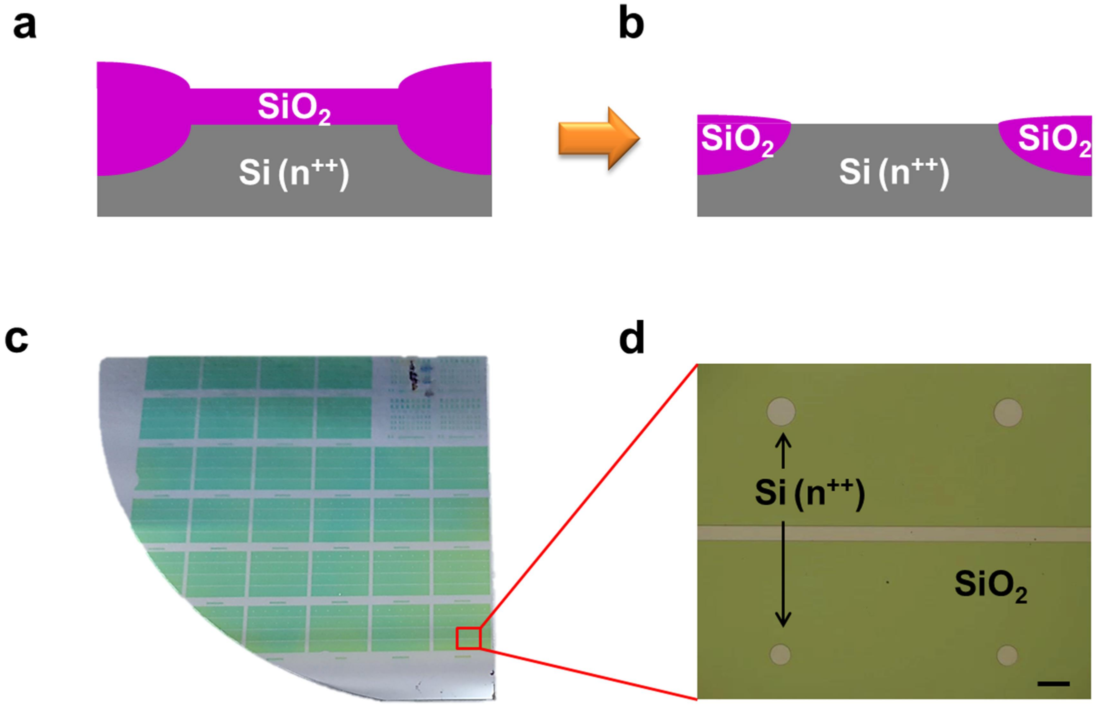

Figure 2.2 Patterned substrates with Si (n^{++}) electrodes isolated by FOX. **a**, Schematic diagram showing a cross section of the substrate after removal of the Si_3N_4 mask. **b**, Schematic diagram showing a Si (n^{++}) electrode surrounded by FOX after the BOE treatment. **c**, Image of the final Si (n^{++}) substrate with Si (n^{++}) electrodes separated by FOX. **d**, Optical image of four Si (n^{++}) electrodes (grey dots) separated by FOX (as indicated by the light green color). Scale bar, 200 μm.

To study the vertical tunneling process, large area CVD graphene grown on top of Cu foil is used. The graphene is transferred from the Cu foil to the patterned substrate using a wet-transfer technique to form the Si (n^{++})/Gr contact. For the transfer, a thin layer of PMMA is first spin-coated on one side of the graphene covered Cu foil, followed by oxygen plasma to remove the graphene on the opposite side. Then the Cu foil is placed floating in Cu etchant for 30 mins to dissolve the Cu, leaving PMMA covered graphene floating on the surface. The PMMA coated graphene is then fished out using a Si substrate and transferred into deionized (DI) water. This process is repeated multiple times before the graphene sheet is fished out by the target substrate. The PMMA layer is removed by rinsing and immersing the substrate in acetone, followed by immersing in acetone heated up to 80 °C for 10 mins. Fig. 2.3a shows the Raman spectrum of the graphene after the wet transfer process. The signature G peak and 2D peak is clearly visible, at 1590 cm^{-1} and 2659 cm^{-1} respectively.

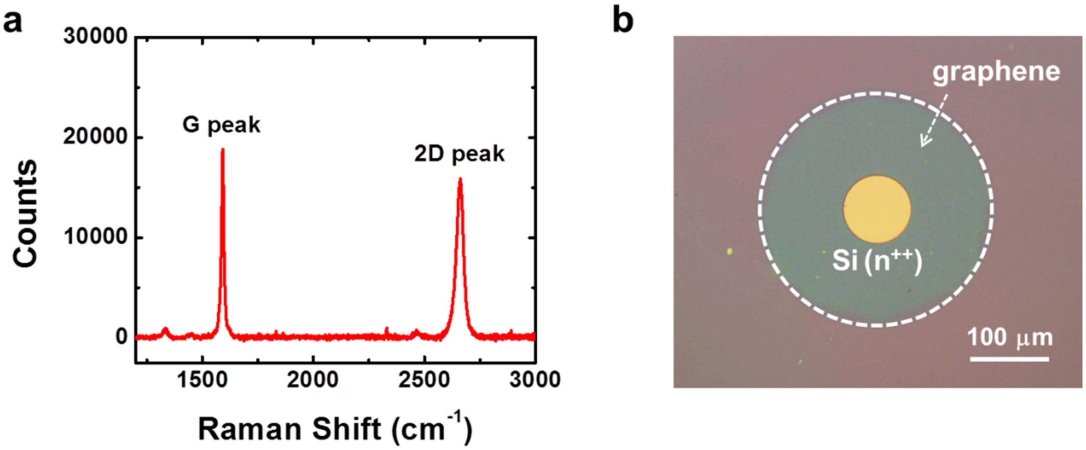

Figure 2.3 Graphene for the investigation of the vertical tunneling process. a, Representative Raman spectrum of the CVD graphene after transfer onto the Si substrate. The G peak and the 2D peak are clearly identified, signatures of a high quality graphene film. **b**, Optical image of patterned graphene disks in contact with the Si (n^{++}) electrode. The graphene region is indicated by the white dash line.

To protect the graphene surface from direct contact to photoresists during the multiple photolithography process that follows, a 3.5 nm Al layer is deposited on top of graphene to act as a protection layer. The thin Al layer oxidizes into Al_2O_3, and is easily removed by developers such as AZ400K when need to. The transferred graphene is patterned into disks using photolithography and oxygen plasma, and the result is shown in Fig. 2.3b, with the graphene region outlined by the white dash line.

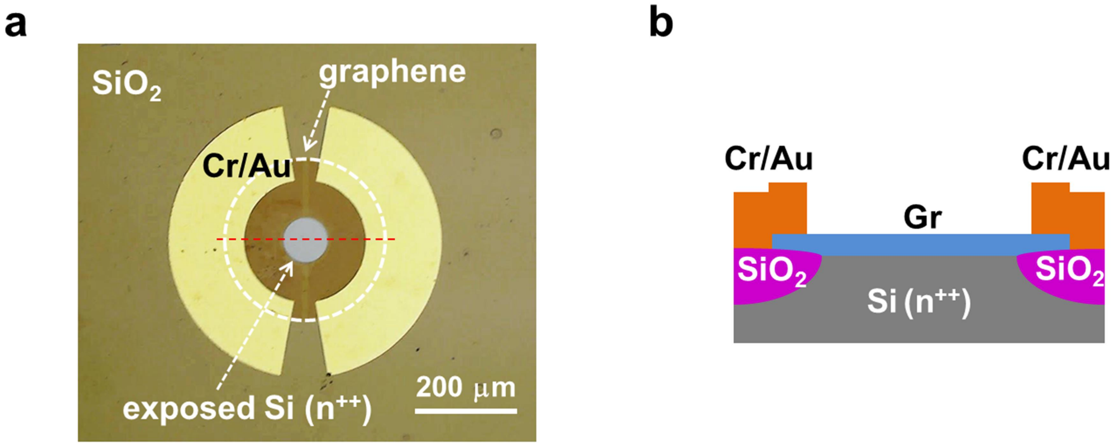

Figure 2.4 'Side contact' structure for the investigation of tunneling into graphene. a, Optical image of the fabricated 'side contact' device. The graphene region is indicated by the white dash line. **b**, Schematic diagram showing the cross section of the 'side contact' structure along the direction indicated by the red dash line in **a**.

Side contacts to the graphene consisting of 10 nm Cr/100 nm Au are defined using photolithography and deposited using e-beam evaporation (CHA Mark 40). Fig. 2.4a shows an optical image of the device with the side contacts deposited, and a schematic diagram showing the cross section of the device along the red dash line in Fig. 2.4a is presented in Fig. 2.4b. Top gate can be added to the side contact structure to tune the relative position of the Fermi level and the Dirac point of graphene. Al_2O_3 of 27 nm thickness is deposited as the top gate dielectric using atomic layer deposition (ALD, Fiji), and the gate electrode is again defined using photolithography and deposited using e-beam evaporation, consisting of a bilayer structure of 85 nm Al and 15 nm Pt. Optical image of the side contact device with top gate is shown in Fig. 2.5a, with a schematic of the cross section given in Fig. 2.5b.

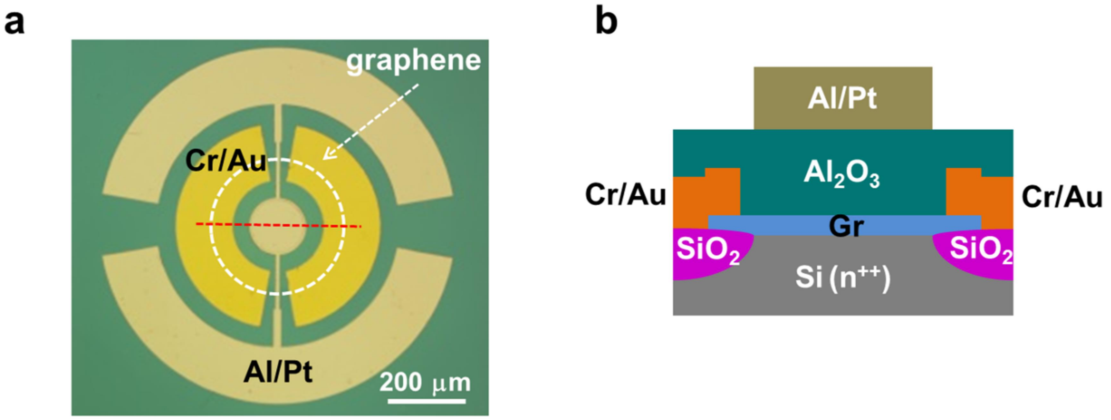

Figure 2.5 Gate controllable 'side contact' ETS structure. a, Optical image of the gate controllable device with the top gate electrode aligned to the injection area. The graphene region is indicated by the white dash line. **b**, Schematic diagram showing a cross-section of the gate controlled 'side contact' structure. The cross section is taken along the direction of the red dash line in **a**.

2.2.2 System Setup and Data Interpretation for the ETS

ETS, sometimes referred to as the inelastic electron tunneling spectroscopy (IETS), measure the first and second order derivatives of the tunneling current across a junction versus the applied bias. It uses the lock-in technique to detect small changes in the carrier transport across a tunnel junction due to the effect of changes in the available DOS, phonon interactions or the existence of trap states. The basic principle is given as follows: when an AC modulation voltage plus a DC offset bias are applied across the device under test (DUT), the modulated current response can be expressed mathematically in the form of Taylor expansion:

$$I(V_b + V_m cos\omega t) = I(V_b) + \left.\frac{dI}{dV}\right|_{V_b} V_m cos\omega t + \frac{1}{2}\left.\frac{d^2I}{dV^2}\right|_{V_b} {V_m}^2 cos^2\omega t + \cdots$$

$$= I(V_b) + \left.\frac{dI}{dV}\right|_{V_b} V_m cos\omega t + \frac{1}{4}\left.\frac{d^2I}{dV^2}\right|_{V_b} {V_m}^2 (1 + cos2\omega t) + \cdots \quad (2.1)$$

in which V_b is the DC bias, V_m is the AC modulation and ω is the modulation frequency. From this equation, it is clearly seen that by measuring the first (ω) and second (2ω) harmonic signal using lock-in amplifiers, the first and second derivative of current versus the applied bias, i.e., the first and second order ETS can be directly measured. This method yield a much higher signal to noise ratio compared to direct mathematical differentiation from DC measurements of current-voltage (I-V) characteristics.

In our experimental setup, the AC modulation with a DC offset is applied to the DUT using a function generation (Agilent 3250). The oscillation frequency is chosen to be 743.3 Hz, and the amplitude of the modulation is 2 mV, which mark the lower limit of the signal width detectable using our setup. The output AC current signal is converted into a voltage signal using a current preamplifier (SR 570) and fed into a lock-in amplifier (SR530) to measure the first harmonic signal. The second order ETS is measured simultaneously by further passing the signal output from the current preamplifier to a voltage preamplifier (SR560) before input into a second lock-in amplifier for second harmonic measurement. A block diagram showing how the various components of our system are connected is presented in Fig. 2.6. To avoid smearing of fine spectrum features due to thermal fluctuation, this setup is operated in a physical properties measurement system (PPMS, Quantum Design) to enable measurement at temperatures as low as 1.9 K.

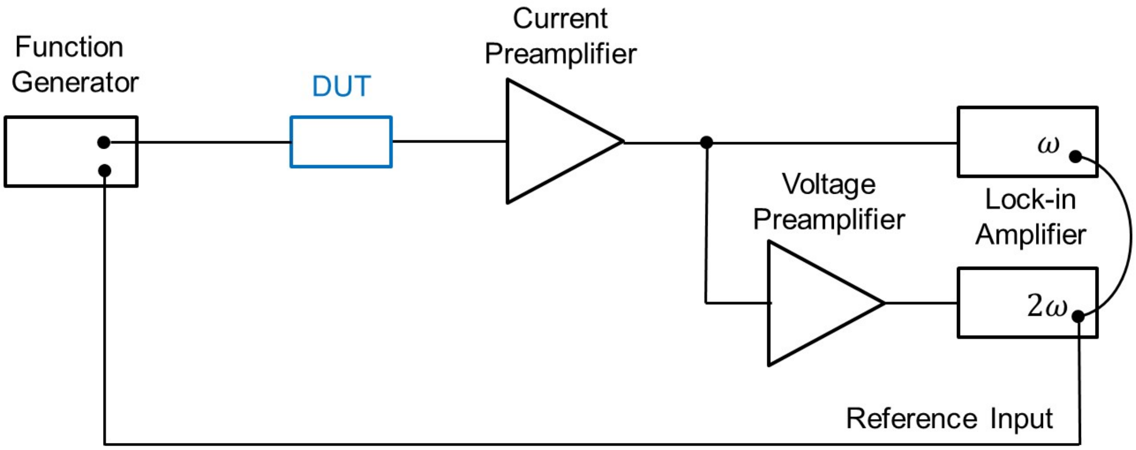

Figure 2.6 Block diagram of the ETS measurement setup. Voltage with an AC modulation is provided by the function generator to the DUT, and the output signal is amplified by the current and voltage preamplifier before input into lock-in amplifiers for first and second harmonic measurements.

Based on the obtained spectrums, materials properties and physical phenomena governing the tunneling process can be identified. Here, phonon assisted tunneling is taken as an example to illustrate data interpretation of ETS. As shown in Fig. 2.7a, when the applied bias exceeds the threshold for activation of a phonon-assisted tunneling process at V_t, an additional conduction channel is opened, resulting in a change in the slope of the *I-V* characteristic, as shown in Fig. 2.7b. This slight change in the slope could be difficult to identify in real data, but it manifest itself as a step in the first order ETS (Fig. 2.7c) and a peak in the second order ETS (Fig. 2.8d), which can be easily identified. Similarly, trap assisted tunneling (Fig. 2.8a) results in a step in the *I-V* characteristic (Fig. 2.8b), a single peak in the first order ETS (Fig. 2.8c) and a double peak feature in the second order ETS (Fig. 2.8d). The first order ETS is also directly correlated with the number of available conduction channels in the tunneling process. Therefore, it can also be a reliable measurement of the DOS of the tunneling electrodes when it is the limiting factor in the tunneling process.

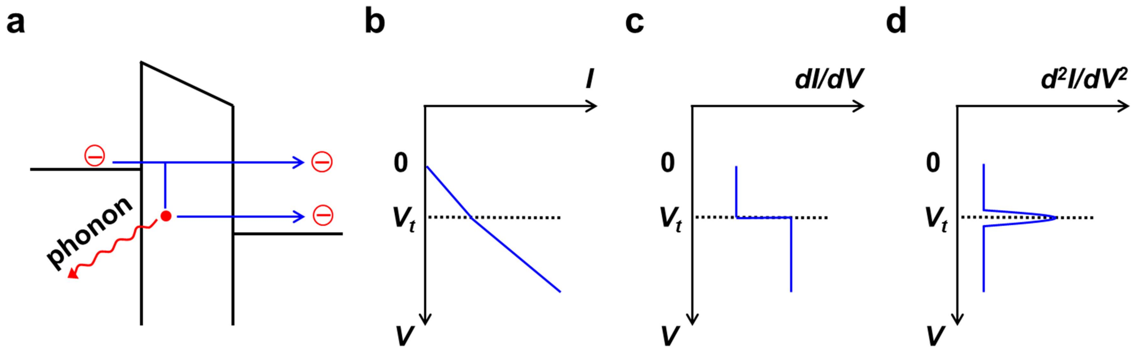

Figure 2.7 ETS signal of phonon assisted tunneling. **a**, Schematic band diagram showing the elastic tunneling process along with a phonon assisted tunneling process. **b**, Schematic diagram showing a change in the slope of the I-V characteristic due to the additional conduction channel from the phonon assisted tunneling process. **c**, Schematic diagram showing a step feature in the first order ETS as a result of the phonon assisted tunneling. **d**, Schematic diagram of the second order ETS showing a peak as a result of the phonon assisted tunneling.

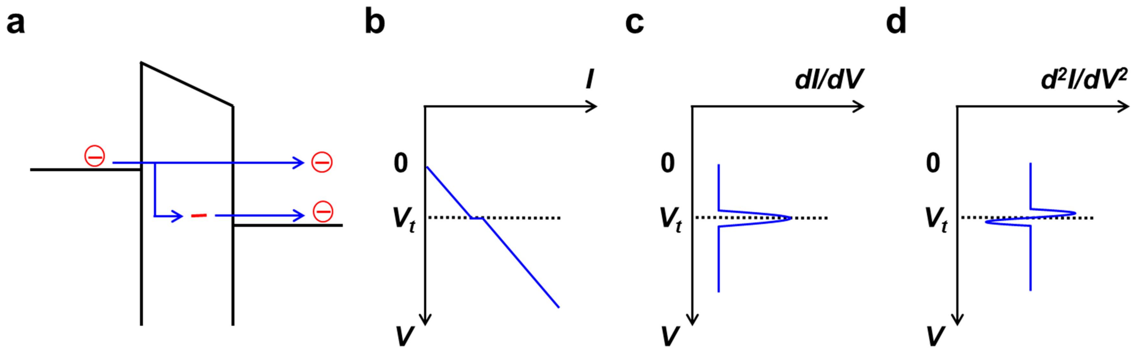

Figure 2.8 ETS signal of trap assisted tunneling. **a**, Schematic band diagram showing the elastic tunneling process along with a trap assisted tunneling process. **b**, Schematic showing a step in the I-V characteristic due to trap assisted tunneling process at a bias of V_t. **c**, Schematic diagram showing a single peak in the first order ETS as a result of trap assisted tunneling. **d**, Schematic diagram of the second order ETS showing a double peak feature as a result of trap assisted tunneling.

To calibrate our ETS measurement setup, commercially available Ge tunneling diodes (1N3712) are measured at 1.9 K. To prevent oscillation caused by the negative differential resistance, a 50 Ω resistor is parallel connected to the diode during measurement as detailed in our group's previous work[93]. The second order ETS measured using our system is given in Fig. 2.9a, and the various phonon modes of Ge is clearly identified at positions consistent with literature values (Fig. 2.9b)[93]. This demonstrates the reliability and the high signal to noise ratio achievable using our setup.

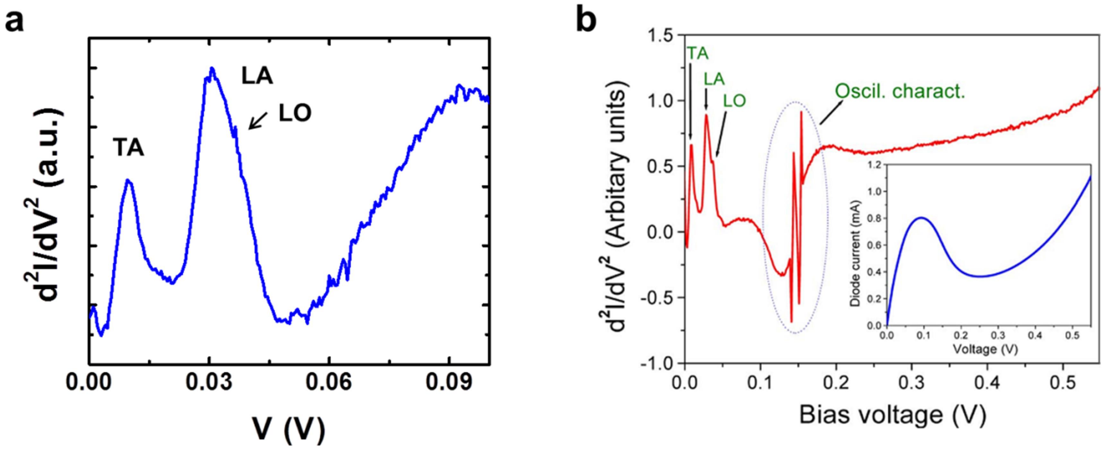

Figure 2.9 Measurement setup calibration using Ge tunnel diodes. a, Second order ETS from commercially available Ge tunnel diodes with features corresponding to phonon modes of Ge. **b**, Literature report of second order ETS from Ge tunnel diodes. The results from our experimental setup are consistent with literature reports. Adapted with permission from ref. (93). Copyright 2006 IEEE.

2.3 Electrical Characterization of Vertical Tunneling into Graphene

2.3.1 Temperature Dependence of the Current Density-Voltage (J-V_S) Characteristic

A schematic diagram showing the measurement setup of the 'side contact' structure is shown in Fig. 2.10a. During the measurement, the Si substrate is grounded and the tunneling bias is applied through the Cr/Au side electrodes. In this structure, the electrons are injected from Si (n^{++}) through the vdW gap and captured by graphene. Then the electrons travel laterally through graphene before it is collected by the Cr/Au electrode, therefore the graphene serves as the counter electrode for collecting the tunneling electrons.

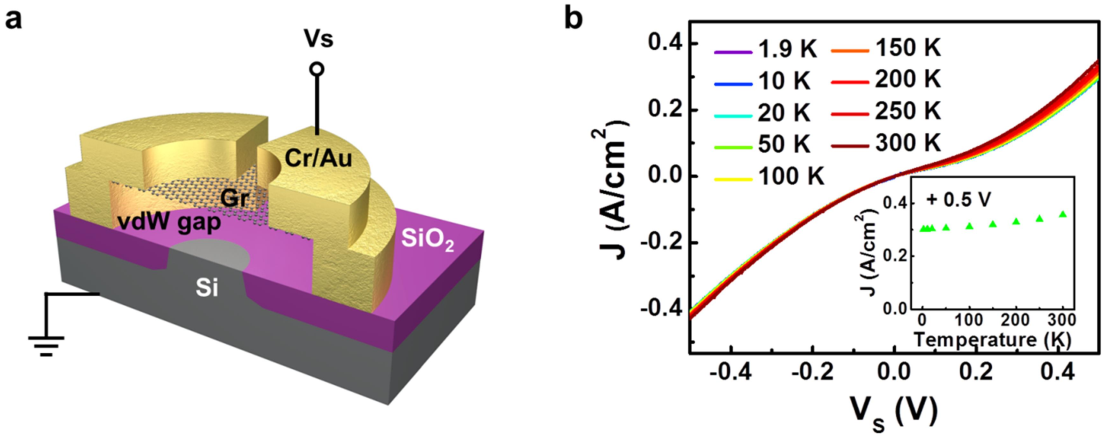

Figure 2.10 J-V_S characteristic of the 'side contact' structure in which graphene acts as the counter electrode in the tunneling process. a, Schematic diagram showing the measurement setup for the 'side contact' structure. During the measurements, Si (n^{++}) is grounded and the side voltage (V_S) is applied through the Cr/Au side electrode. **b,** J-V_S characteristics at various temperatures showing little temperature dependence. Inset plots J as a function of temperature at a bias of +0.5 V.

Fig. 2.10b shows the J-V_S characteristics at different temperatures for this 'side contact' device. The inset of Fig. 2.10b plots the current density at $V_S = 0.5\ V$ versus temperature, showing little temperature dependence of the J-V_S characteristic. Meanwhile, except for the nonlinearity, the curves do not show significant rectification. Considering both aspects, it can be concluded that the contact between the graphene and the silicon is neither ohmic nor Schottky, but tunneling. The Si (n^{++}) is treated with HF immediately before the transfer of the graphene onto its surface, i.e., the silicon surface is passivated by Si-H bond[94], which is relatively inert and dangling bond free, similar to the surface of graphene. As a result, a vdW gap is anticipated to form between the hydrogen terminated Si surface and graphene, as illustrated in Fig. 2.11. Our temperature dependent J-V_S curves collected from the 'side contact' device confirmed this hypothesis. For this type of contact, the tunneling current density is on the order of 0.1 A/cm^2. Therefore we conclude that a tunneling type transport dominates due to the presence of the vdW gap, although graphene is well-accepted as a zero band gap semiconductor[25, 95] or semi-metal[1].

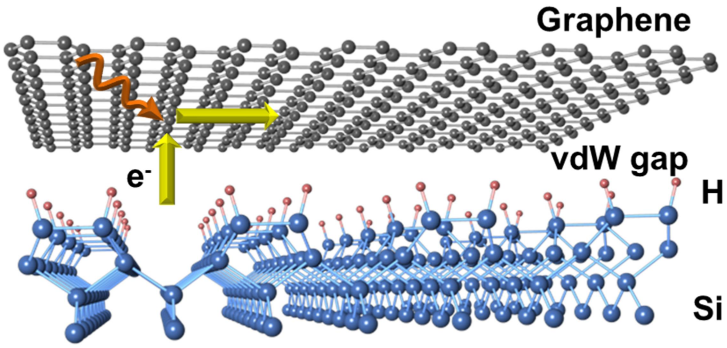

Figure 2.11 Schematic diagram showing a close-up look at the vdW gap between the graphene and the Si (n^{++}). The yellow arrows indicate the flow of electrons from Si through the vdW gap and into the graphene layer. The orange arrow illustrates the need for phonon or other elemental excitations to participate in this process due to the requirement of momentum conservation.

2.3.2 Temperature Dependence of the ETS

To further our insight into the tunneling behavior through the vdW gap and the lateral transport from the graphene counter electrode, we performed the first order and second order ETS.

The first order ETS is commonly used to probe the DOS of samples under study. The tunneling current can be expressed using the Bardeen model as[51]:

$$I = \frac{4\pi e}{\hbar}\int_0^{eV_S} \rho_{Si}(\varepsilon - eV_S)\rho_{graphene}(\varepsilon)T(\varepsilon)\, d\varepsilon \qquad (2.2)$$

to emphasize the effect of the dispersion of the DOS. Here, ρ_{Si} is the DOS of the Si (n^{++}) electrode, $\rho_{graphene}$ is the DOS of graphene acting as the counter electrode in the tunneling process, $\hbar$ is the reduced Plank constant and V_S is the sample bias. $T(\varepsilon)$ is the transmission factor, which varies exponentially as a function of the barrier height. For this as fabricated 'side contact' structure, electrons tunnel from the Si (n^{++}) electrode to the graphene sample first via the vdW gap, followed by an electron-phonon relaxation process to the states near the K/K' points of the graphene before they reach the metal contact.

The 1st and 2nd order ETS for the 'side contact' structure measured at 1.9 K are shown in Fig. 2.12a. The V-shaped 1st order ETS agrees remarkably well with the DOS in graphene, which exhibits a linear dependence of energy[24, 96]. The positions of the dI/dV minima could be determined from the 2nd order ETS to be located approximately at 70 mV, corresponding to the difference between the Fermi level and the Dirac point of the graphene. Note that as the bias voltage is reduced to zero, the Fermi levels of the graphene and Si are aligned and there should be no net flux for the direct tunneling process, corresponding to the zero current density in the J-V_S characteristic shown in Fig. 2.10b. However, the 1st ETS does not necessarily go to a minimum. In our measurement, we observed a local minimum and fine features near the zero bias point, the latter of which is probably due to charge puddles inherently present within the graphene plane[92].

The observed oscillations near the zero bias are smeared out at elevated temperatures as shown in Fig. 2.12b, due to thermal excitation of electrons by phonons in the tunneling process. The band structure of graphene, on the other hand, is not significantly affected by the thermal excitation and thus, even at high temperatures, we can still observe the V-shaped feature with a minimum around 70 mV, although broadened to some extent; this fact confirms our association of the minimum point to the Dirac cone in the graphene. Based on this analysis, the Dirac cone of the graphene is located ~70 meV above the Fermi level, indicating that the graphene is p-doped, which is consistent with the reported observation for graphene supported by a substrate[97, 98].

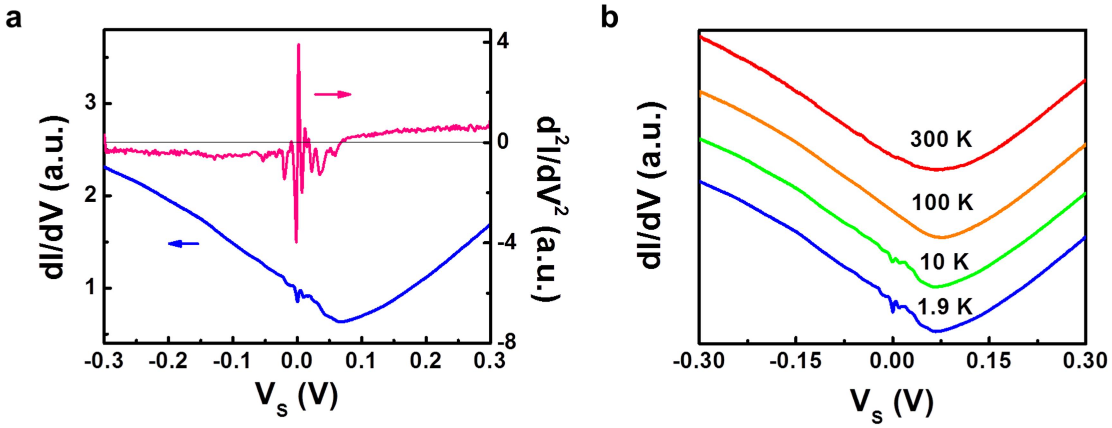

Figure 2.12 Temperature dependent ETS of the 'side contact' device. a, First and second order ETS spectrum from the 'side contact' device. The first order spectrum exhibits a V-shape feature, signature of the DOS distribution for the Dirac fermions in graphene. The position of the Dirac point corresponds to the intercept of the second order spectrum with the x axis. **b**, first order ETS spectrum at various temperatures.

The energy band diagrams of the 'side contact' structure for positive, zero, and negative V_S are shown in Fig. 2.13 a-c, respectively. The grey area indicates the states available in graphene for the tunneling process to and from graphene, and the shaded area illustrates the extra states available with an increase in the absolute value of V_S. Therefore for both cases, the first order ETS, i.e., the conductivity of the tunneling junction, is directly linked to the DOS of graphene as the counter electrode.

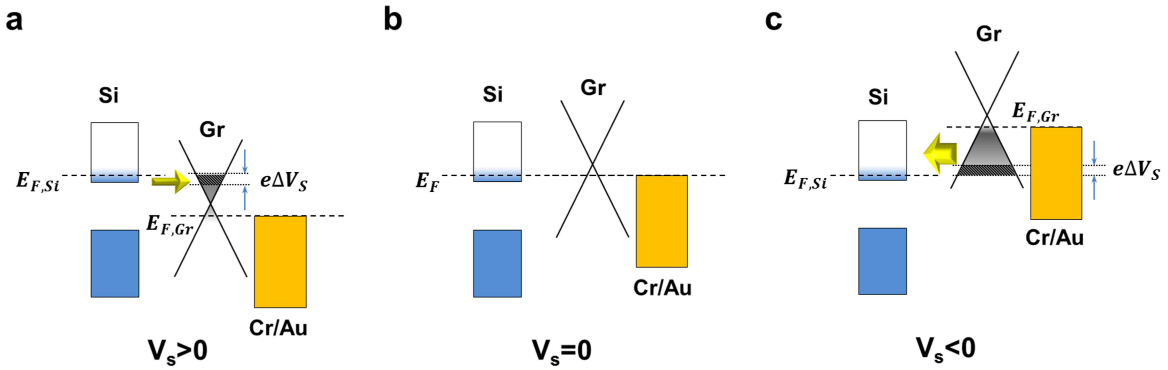

Figure 2.13 Schematic diagrams showing the band alignment at positive (a), zero (b) and negative (c) sample biases. Shaded areas indicate the additional states responsible for the conductivity increase with a small increment in the absolute value of the sample bias.

2.3.3 Gate Control of the ETS

The Dirac point energy relative to the Fermi level of graphene can be tuned by applying a gate voltage, which can be used to unambiguously identify features related to the Dirac cone. For this purpose, a top gate is added to the 'side contact' structure and a schematic diagram of the cross section of the device is shown in Fig. 2.14a. To maximize the tuning effect, the gate electrode is aligned to be directly on top of the exposed Si (n^{++}) region. The first order ETS is shown in Fig. 2.14b for various top gate voltages (V_G). It is clearly seen that the position of the lowest point in the V-shape feature shifts monotonically in respect to the applied V_G, signature of a Dirac-cone related feature. Within the range investigated here, the shift is linear as a function of the applied gate voltage, as shown in Fig. 2.14c. Note that the ETS spectrums in the gated device is much noisier compared to those without the gate dielectric layer on top, presumably due to the strong interface scattering, which also led to the smearing of the zero-bias features given in Fig. 2.14b.

It is worth noting that the observed features are similar to those from previous reports of carrier injection through an artificial gap into vdW materials. Injecting electrons from a metal tip through an air gap using STM, Crommie's group observed the V-shaped feature in the 1st order ETS that is tunable with the application of a gate bias[52]. The 1st order ETS of electron injection through multi-layer *h*-BN into graphene has also been reported, with signature of the Dirac cone feature clearly identified[58]. These results confirm the analogy between the vdW gap formed at the Si/graphene interface and an artificial tunnel barrier, and that the vdW gap is the origin of the observed quantum tunneling behavior.

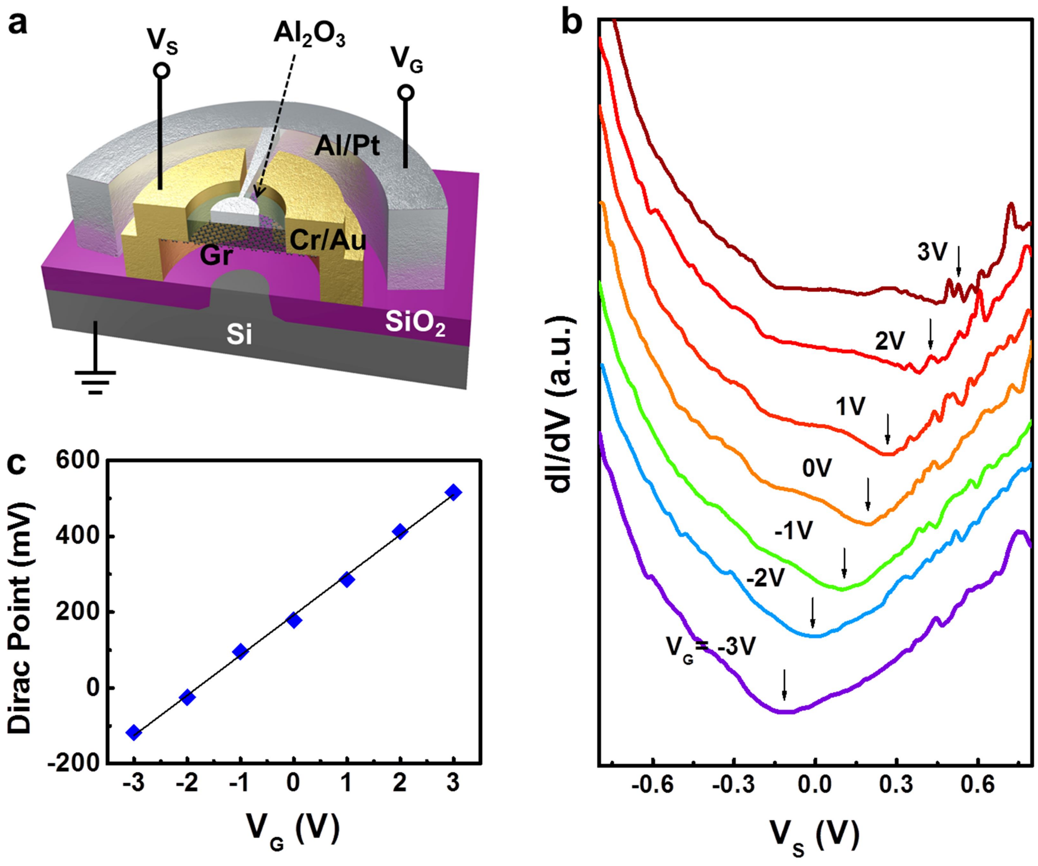

Figure 2.14 Gate controllable 'side contact' ETS. a, Schematic diagram showing a cross-section of the gate controlled side contact structure. **b,** first order ETS spectrum under various gate voltages. Black arrows indicate the position of the Dirac point. Systematic shift in the position of the minimum is observed when tuning the gate bias, further indicating that the origin of the minimum is related to the Dirac cone of graphene. **c,** Shift in the relative position of the

Dirac point of graphene and the Fermi level plotted against the gate voltage, which appears as a linear function.

2.4 Summary

In this chapter, we systematically studied the vertical injection of electrons through the vdW gap and into vdW materials using graphene as a model system. It is found that graphene formed a fully preserved vdW gap with passivated surfaces at the Si/graphene interface which effectively act as a tunnel barrier. When graphene was used as the counter electrode to collect the electrons injected through the vdW gap, the electrons were forced to travel laterally within the graphene, and thus only those that have relaxed to the states near the K/K' points of graphene were selectively collected. This is explicitly demonstrated using low temperature ETS, in which the linear DOS of graphene is found to be the limiting factor governing the injection process. This study could provide a clear theoretical guideline towards the design and analysis of 2D heterostructures and 2D/3D interfaces, in particular, optimizing the contact resistance between metal and vdW materials.

Chapter 3 Vertical Tunneling across vdW Materials

3.1 Motivation

In many emergent device structures, instead of acting as the counter-electrodes, charge or spin carriers travel perpendicularly through the vdW materials, with limited lateral transport[20, 33, 78, 79, 81]. Thus, there has been significant interest in using vdW materials as the quantum tunneling media. For example, graphene and other vdW materials can be applied as the base in hot electron transistors[78, 79, 82]. In this type of device applications, the vdW material is used to control the vertical flow of electrons by tuning the shape of the tunnel barrier (usually SiO_2 or Al_2O_3) sandwiched between graphene and the emitter. In this case, it is the vertical tunneling process that is of importance, and the lateral transport within the vdW material layer is no longer the main concern. Another potential application is to use graphene as a tunnel barrier for spin injection[59, 88]. It is well known that spin polarized electrons can be injected into a semiconductor more effectively through a tunnel barrier, rather than direct injection through a conductor[99, 100] due to conductivity mismatching. The lack of a periodic crystal structure in the normal direction of vdW materials and their thin atomic-scale thickness lead to a dramatically different transport mechanism in the vertical direction from that in the lateral. Thus, most of the elements of the widely accepted models become inapplicable. One striking example is that although graphene is typically treated as a semi-metal or zero-gap semiconductor, it behaves as an insulating tunnel barrier for vertical spin injection[59].

In spite of the recent progress, however, the physical picture of the out-of-plane transport across vdW materials remains mostly unexplored. In particular, the interplay between the in-plane band structure and the out-of-plane transport process, as well as the effect of the interface between the vdW materials and the electrodes remain elusive. In this chapter, we study the important role of graphene as a tunnel barrier through the fabrication of a graphene vertical tunneling device in which the graphene layer together with the vdW gaps serve as the tunneling medium. By purposely excluding the effect of lateral transport from the structure, we provide insight into the vertical transport in single layer graphene and identify the effects from both quantum and classical theories. Due to the transverse momentum mismatch and the atomic thickness of graphene, the vertical tunneling electrons are unable to interact significantly with the intrinsic graphene 2D band structure. Meanwhile, the graphene, being a semi-metal in the lateral direction, can store charges and effectively tune the profile of the tunnel barrier via the quantum capacitance effect, thus imposing an electrical field to control the electrons in a more classical manner. A theoretical model to quantitatively explain the experimental observations and elucidate the role of graphene in vertical tunneling is established. This is followed by a brief discussion of vertical tunneling across few-layer graphene.

3.2 Device Structure for the Study of Vertical Tunneling across Graphene

3.2.1 Fabrication of the 'Top Contact' Structure

Pure out-of-plane transport across the single layer graphene is achieved by constructing a vertical heterostructure in which the graphene is sandwiched between two vertically aligned electrodes, Si (n^{++}) and Cr/Au. The optical image and schematic diagram are given in Fig. 3.1a and 3.1b, respectively. In contrast to the 'side contact' structure form the previous chapter, the top Cr/Au contact is aligned to the Si (n^{++}) injection area in this configuration, so that the electrons are directly collected by the top Cr/Au electrode without lateral transport, and the graphene serves only as a tunneling medium.

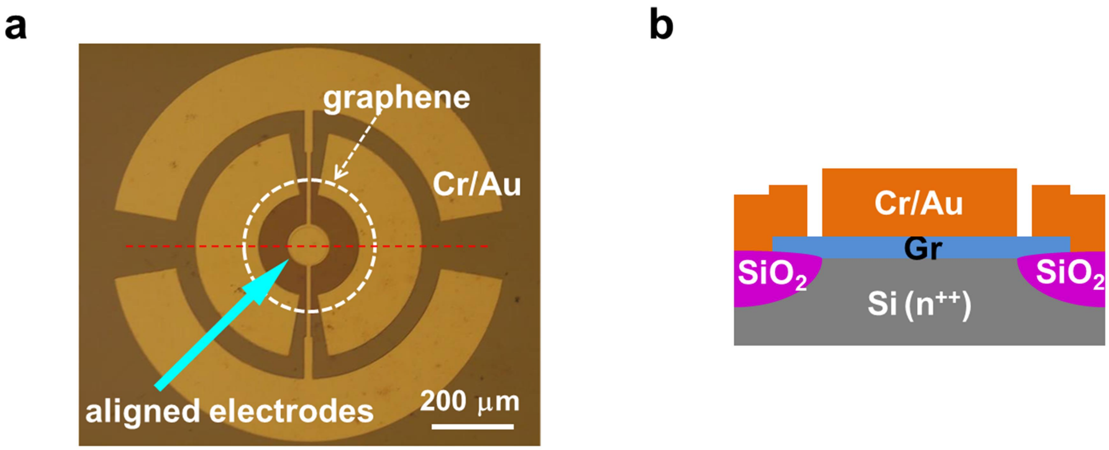

Figure 3.1 Device structure for the investigation of the vertical tunneling through graphene. **a**, Optical image of the fabricated device with the graphene region outlined by the white dash line. The top electrode is aligned to the exposed Si (n^{++}) region, sandwiching the graphene. **b**, Schematic diagram showing the cross section of the vertical tunneling devices. The cross section is cut along the red dash line in **a**.

3.2.2 High Resolution Transmission Electron Microscopy (HRTEM) Analysis of the Vertical Structure

To characterize the various interfaces of the vertical tunneling structure, as well as to identify the presence of the graphene induced vdW gap, a cross-section transmission electron microscopy (TEM) analysis was performed. In this case, a Pt film was deposited on top of the vertical structure to act as a protection layer for the focused ion beam milling process in the sample preparation. The high-angle annular dark field (HAADF) scanning TEM (STEM) image of the sample is shown in Fig. 3.2a. A spatially resolved energy-dispersive X-ray spectroscopy (EDS) mapping of Si, C, Cr and Au (Fig. 3.2b) confirmed the layer components of the vertical structure. The graphene is visible in Fig. 3.2b as a thin line adjacent to the Si substrate. The result of the high resolution STEM (HRSTEM) is shown in Fig. 3.2c for the interfaces between Si/graphene and graphene/Cr. The intensity profile for the cross section of 3.2c is shown in Fig. 3.2d, in which the three distinct material regions can be identified. The monolayer graphene (plus the vdW gap) appears as a nanometer scale gap on top of the atomically flat Si substrate.

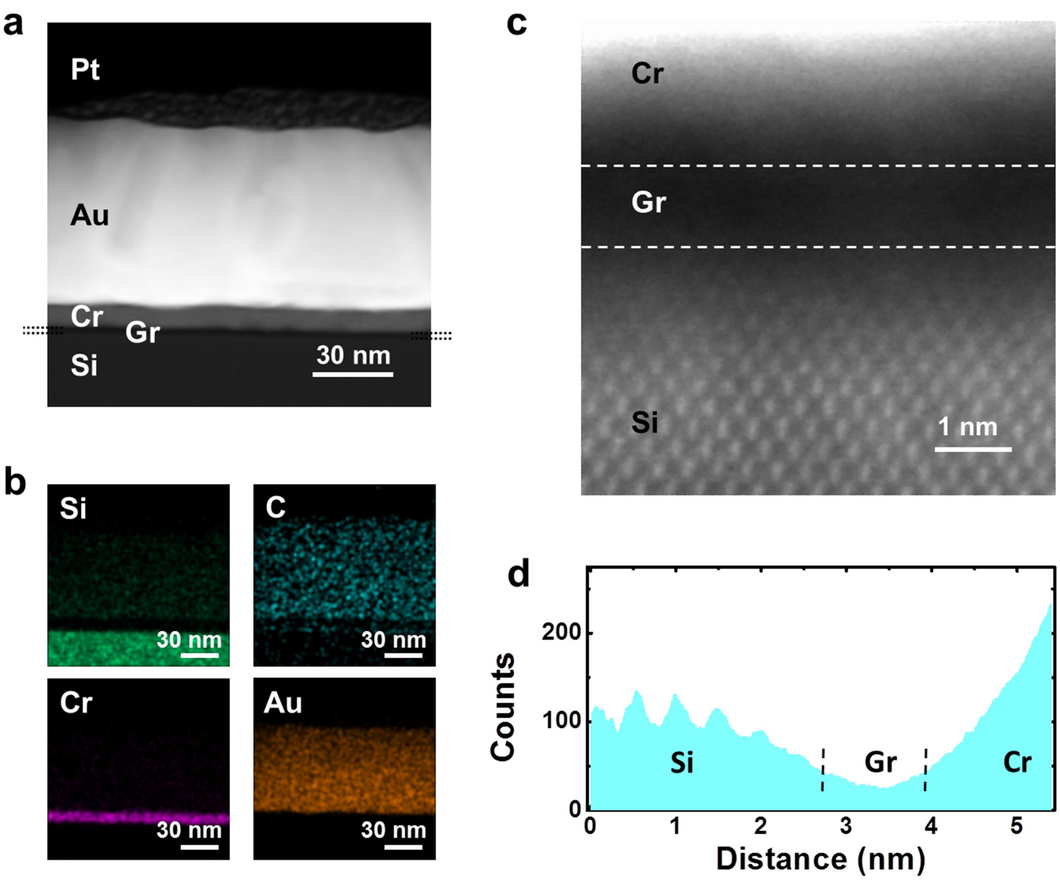

Figure 3.2 Cross-section TEM of the graphene tunneling structure. a, Low magnification HAADF STEM image showing the cross section of the vertical tunneling structure. The monolayer graphene and the vdW gap are visible as a dark line located between Si and Cr, which is outlined by the black dotted line. **b,** Spatially resolved EDS analysis indicating the distribution of Si, C, Cr and Au. **c,** HRSTEM image of the Si/graphene/Cr interface revealing the existence of a gap-like feature as outlined by the white dashed lines. **d,** Height profile from a section of the HRSTEM image in **c**.

3.3 Electrical Characterization of Vertical Tunneling across the Graphene

3.3.1 Temperature Dependence of the *J*-V_S Characteristic

A schematic diagram of the measurement setup of vertical tunneling across graphene is shown in Fig. 3.3a, and the Si (n^{++}) electrode is grounded during measurement, with the tunneling bias applied through the top Cr/Au electrode.

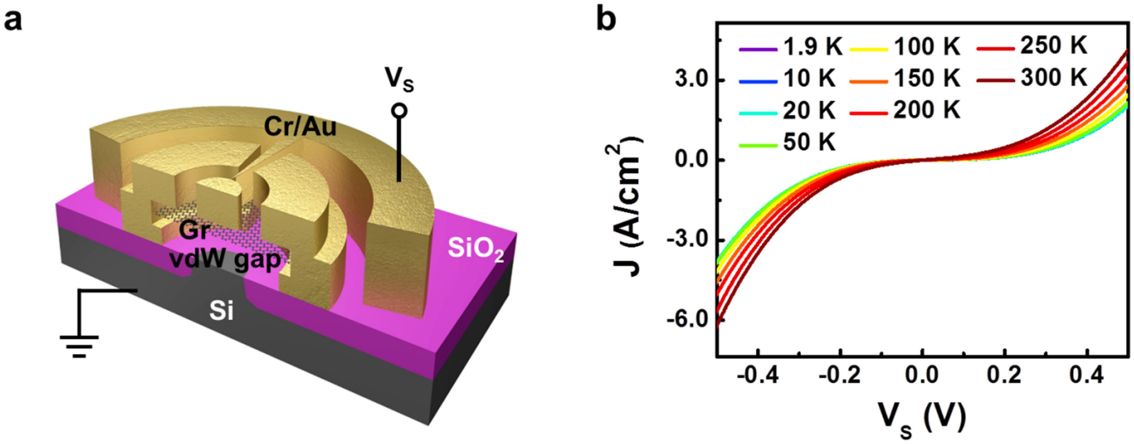

Figure 3.3 Vertical tunneling devices in which graphene acts as a tunnel medium. a, Schematic diagram showing the device structure of the vertical tunneling device. The Si (n^{++}) is grounded during measurements and the bias is applied through the Cr/Au top electrode. **b,** *J*-V_S characteristics at various temperatures showing slightly larger temperature dependence compared to the 'side contact' device.

Fig. 3.3b shows typical *J*-V_S characteristics of the 'top contact' vertical tunneling device at various temperatures. Similar to that of the 'side contact' device, the *J*-V_S curves do not show significant rectification. The temperature dependence of the current density is slightly stronger in the vertical tunneling device than the 'side contact' structure shown in the previous chapter, but it is still insignificant compared to thermally activated processes such as transport over Schottky junctions. The temperature dependence of the current density is presented in Fig. 3.4. It is found that the current density $J \propto T^2$, characteristic of direct tunneling processes such as those for traditional metal-insulator-metal structures[101, 102].

As a sanity check, devices with Cr/Au directly in contact with the Si (n^{++}) is fabricated simultaneously and compared with the vertical structure, and an ohmic behavior is observed, evidence that the tunneling behavior indeed comes from incorporation of the graphene (Fig. 3.5).

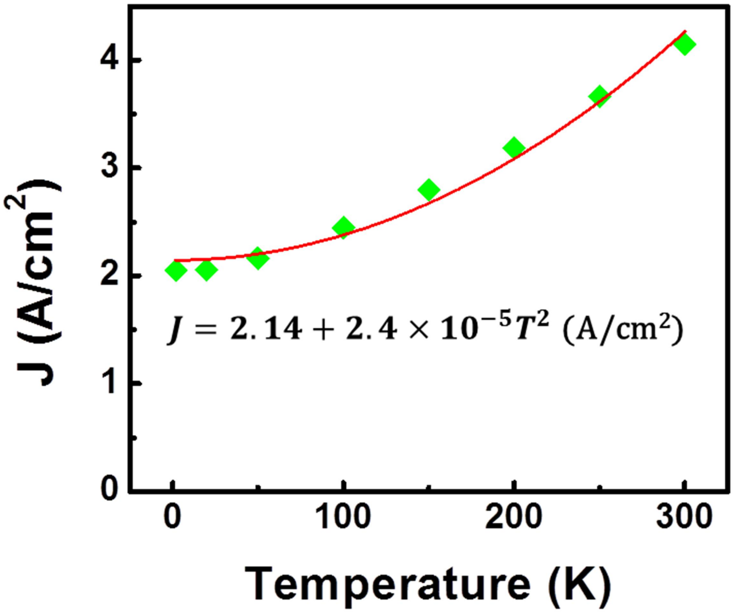

Figure 3.4 J as a function of temperature at $V_S = 0.5\ V$. The data points can be fitted to a parabolic function (red line), identical to that of typical direct tunneling processes through metal-insulator-metal junctions.

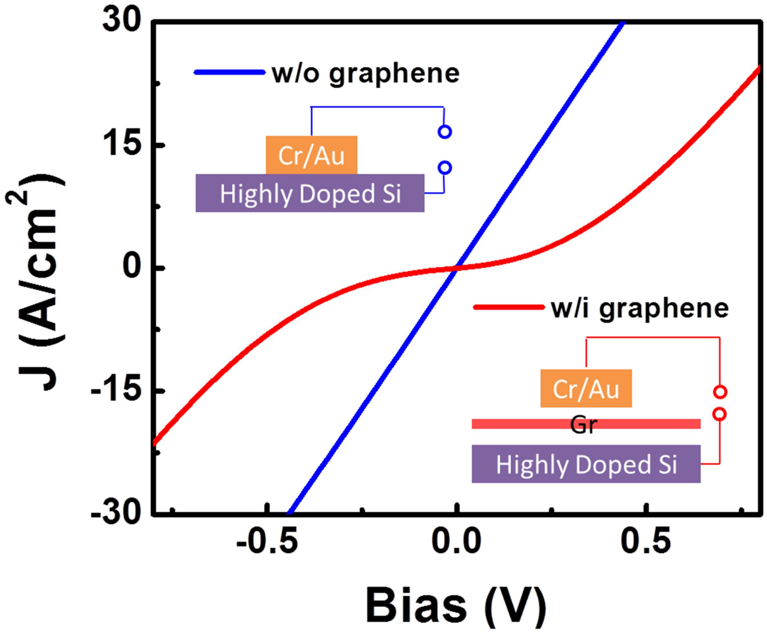

Figure 3.5 Comparison between the J-V_S characteristics of vertical structure with (red) and without (blue) graphene in the middle. Insets show the schematic diagrams of the corresponding structures.

3.3.2 Temperature Dependent ETS Measurements

In addition to the direct tunneling nature of the tunneling current, another significant point to note is that the tunneling current density is one order of magnitude larger than that of the 'side contact' device in the previous chapter. This fact indicates that graphene is almost transparent to electrons, and only a small portion of the electrons are reflected or absorbed by the single layer graphene. Indeed, 1st ETS shown in Fig. 3.6a is dramatically different from that of the 'side contact' device, the most salient difference being the disappearance of the Dirac cone fingerprint with the elimination of lateral transport. Instead, the 1st ETS shows a consistent minimum dI/dV at zero bias, but no other significant feature. There are some weak kinks and bumps, which are barely visible from the 2nd ETS shown in Fig. 3.6b. This observation underscores the fact that the electrons do not interact with the band structure of the graphene significantly during the tunneling process across the graphene, which only acts as a thin tunnel barrier.

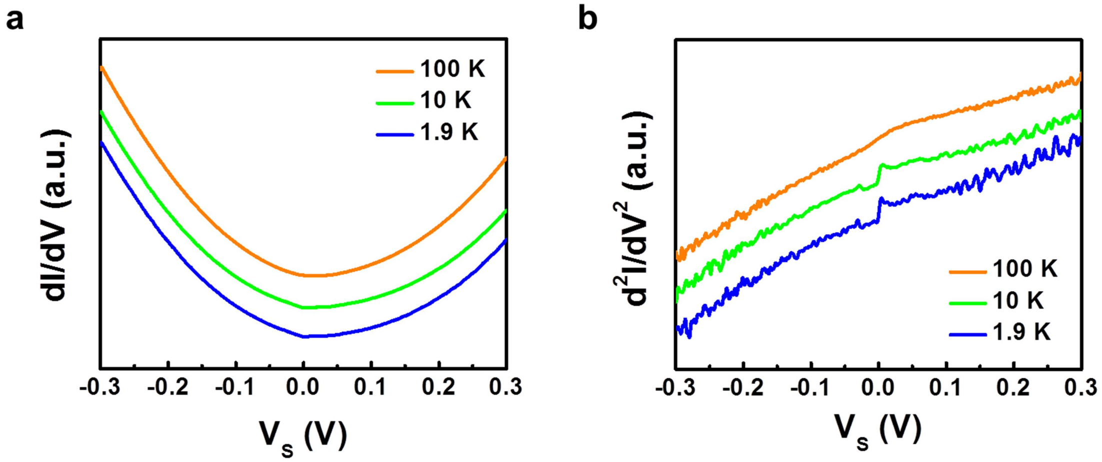

Figure 3.6 Temperature dependent ETS of the vertical tunneling structure. a, First order ETS spectrum at various temperatures showing a consistent minimum at zero bias. No feature related to the lateral band structure of graphene is observed. **b**, Second order ETS spectrum at various temperatures showing reproducible oscillations.

Unlike that of the 'side contact' device, in which the lateral transport demands the conservation of energy and momentum to be met by phonon scattering or other elementary excitations, nearly no momentum relaxation is warranted due to the short transit time across the graphene in this vertical structure. Thus a large amount of electrons will not need to relax to near the K/K' points of the graphene, hence the transport via states near the Dirac cone is no longer applicable. In addition to the atomic thickness of graphene, the large momentum mismatch between injected electrons and the graphene band structure further limit the interactions, as shown in Fig. 3.7, in which the Fermi surface of Si, graphene, and the Au electrode is schematically shown. The momentum of the electrons injected from the valleys near the X point is around 0.98×10^{8} cm^{-1}, while graphene exhibits a Fermi momentum of 1.7×10^{8} cm^{-1}, and thus a large momentum mismatch (red arrow) is present. The same argument can be applied to electrons injected from the Cr/Au electrode, which has a transverse momentum ranging from zero to the Fermi momentum of the metal (1.2×10^8 for Au). As a result, little interaction occurs as the emitted electrons pass through the graphene and are collected by the Cr/Au electrodes; and the collected electrons relax to the available states of the electrodes.

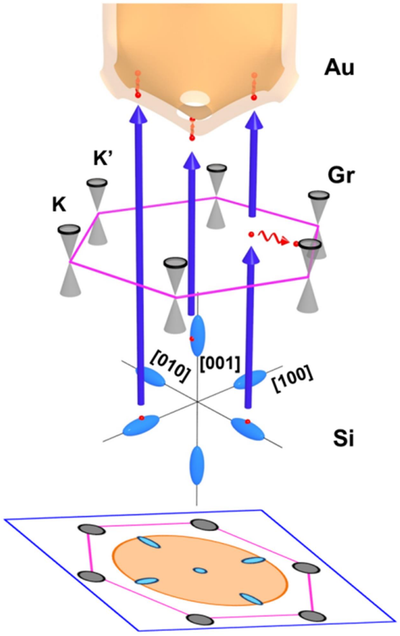

Figure 3.7 Schematic diagram showing the momentum mismatch for the vertical transport of electrons through graphene. The Fermi surfaces of Si (blue ellipses), graphene (black rings in the middle) and the Au electrode of the vertical graphene tunneling structure are plotted. For electrons tunneling from the Si through the graphene to the Au electrode, the majority pass through graphene without interaction with the graphene band structure due to its atomic thickness and the traverse momentum mismatch (red arrow).

3.3.3 Theoretical Calculation based on the Direct Tunneling Model

Since we have established that the vertical tunneling electrons do not interact significantly with the graphene in-plane band structure, and the graphene acts mainly as a tunnel barrier, we can apply the Simmons' direct tunneling model under the Wentzel–Kramers–Brillouin (WKB) approximation to analyze the vertical tunneling process across graphene[103]. The transmission factor, i.e., the probability of electrons penetrating through a potential barrier of height *V (x)* is expressed as:

$$T(E_x) = \exp\left(-\frac{2\sqrt{2m}}{\hbar}\int_0^d \sqrt{V\ (x) - E_x}dx\right) \tag{3.1}$$

in which E_x is the kinetic energy of electrons in the x direction, and d is the thickness of the barrier. m is the free electron mass considering its motion in the vdW gap. The integral can be replaced by an effective barrier height, $\bar{\varphi}$, and a ideality factor, β:

$$T(E_x) = \exp\left(-\frac{2\beta d\sqrt{2m}(\bar{\varphi} - E_x)}{\hbar}\right) \tag{3.2}$$

β is close to 1.

The current density the flows across the barrier is then given by the current flow from electrode 1 to electrode 2, minus the current flow from electrode 2 to electrode 1, as shown in Fig. 3.8. The current density is therefore given as:

$$J = \frac{4\pi m^2 e}{h^3} \int_0^{E_m} T(E_x)dE_x \int_0^{\infty} [f(E) - f(E + eV)]\,\mathrm{d}E_t \tag{3.3}$$

E_t is the traverse energy. Under zero bias, this equation is reduced to:

$$J = J_0\left[\bar{\varphi} \times e^{-\alpha\beta\sqrt{\bar{\varphi}}} - (\bar{\varphi} + eV) \times e^{-\alpha\beta\sqrt{\bar{\varphi}+eV}}\right] \tag{3.4}$$

In which,

$$J_0 = \frac{e}{2\pi h\beta^2 d^2} \tag{3.5}$$

$$\alpha = \frac{4\pi d}{h}\sqrt{2m} \tag{3.6}$$

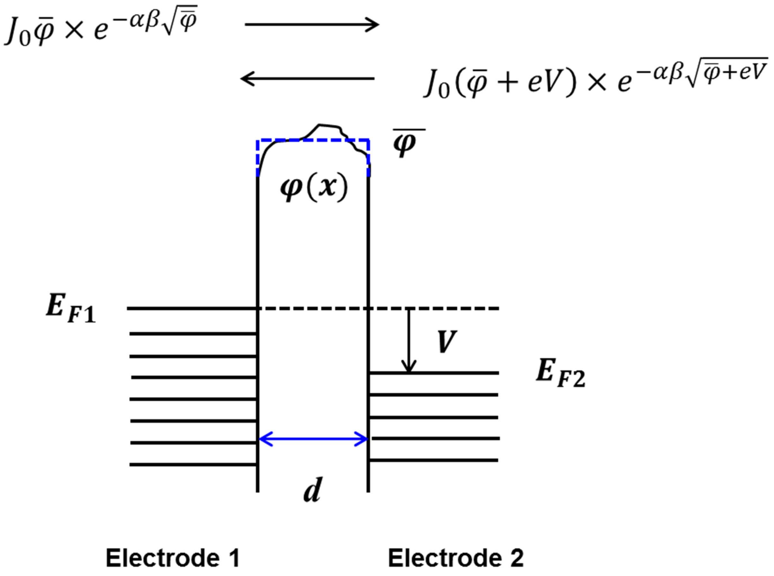

Figure 3.8 Schematic diagram showing the current flow between the two electrodes for direct tunneling.

The effective barrier height is related to the barrier height for electrons injecting from the two electrodes, φ_1 *and* φ_2, as well as the applied voltage, *V*, as shown in Fig. 3.9. Fig. 3.9a plots a schematic band diagram for the tunnel junction with asymmetric electrodes in flat band condition. This trapezoidal barrier can be approximated by an average barrier height:

$$\varphi = \frac{1}{2}(\varphi_1 + \varphi_2) \tag{3.7}$$

as shown in Fig. 3.9b at zero bias. When a bias is applied, the barrier is further lowered by an amount proportional to *V*, and the effective barrier height is:

$$\bar{\varphi} = \varphi - kV = \frac{1}{2}(\varphi_1 + \varphi_2) - keV \tag{3.8}$$

k is 0.5 for a uniform potential drop across the potential barrier, and the *J-V* characteristic is symmetric. It is worth noting that a slight asymmetry is observed for the *J-V* characteristics in our case, a direct consequence of a non-uniform voltage drop across the barrier originating from the electron trapping and quantum capacitance of the graphene layer, as to be discussed in detail later. To reflect this effect, we introduce a k factor into the original Simmons' model under the Wentzel-Kramers-Brillouin (WKB) approximation, as shown in Fig. 3.9c.

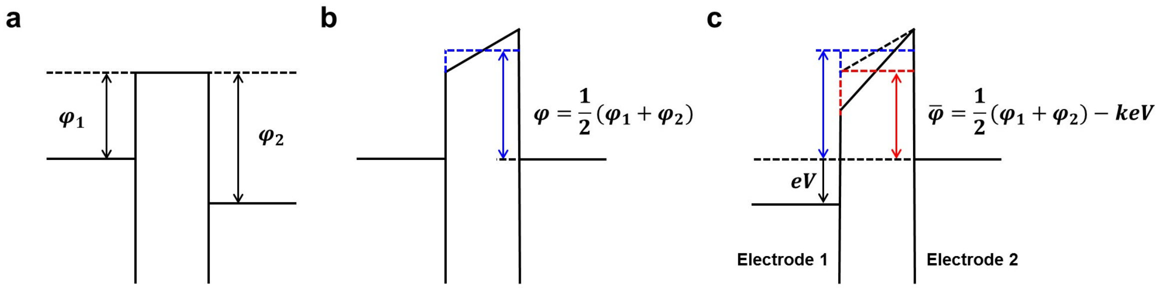

Figure 3.9 Effective potential barrier height of the direct tunneling model. a, Flat band condition for a tunneling junction with asymmetric electrodes. **b,** The zero bias effective barrier height of the tunneling junction with asymmetric electrodes. **c,** The effective barrier height lowering due to the application of a bias.

The *J-V* curve at 1.9 K in Fig. 3.3b is fitted to equation (3.4) as shown in Fig. 3.10. Fitting parameters include an equivalent thickness of 2.3 nm, 0.8 eV average barrier height, and f equals to 0.44 which deviate from 0.5 slightly, to account for the minor asymmetry in the observed *J-V* characteristic. Note φ is much smaller compared to the energy difference from the conduction band of Si (or the work function of Cr) to vacuum, indicating that it is insufficient to consider the vdW gap as a vacuum spacing and ignore the interactions between tunneling electrons and the evanescent surface states. The barrier height lowering stemming from the image charge could further contribute to this effect.

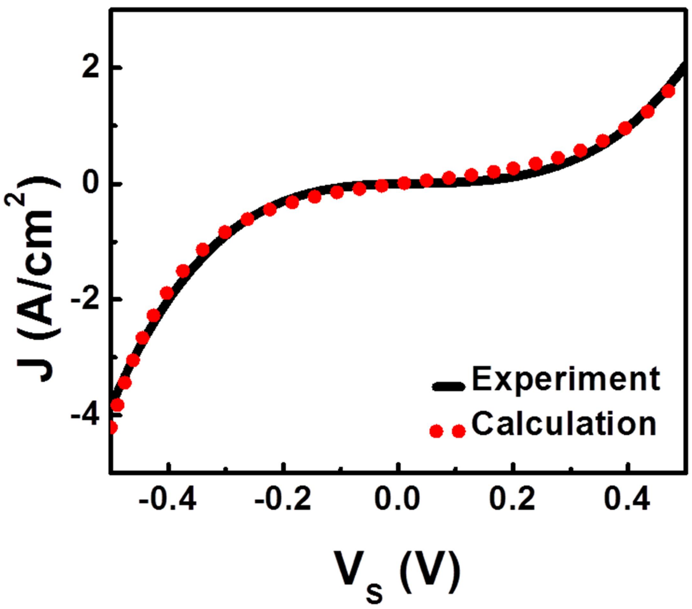

Figure 3.10 *J*-V_S characteristic at 1.9 K (black line) along with the theoretical fit to the direct tunneling model (red dotted line).

3.3.4 Capacitance Model for the Vertical Tunneling across Graphene

Although the momentum and energy mismatch prevent quantum interaction between the tunneling electrons and the graphene band structure, the graphene layer can modify the potential and thus the electrical field of the structure, which leads to the asymmetric tunneling J-V_S feature mentioned before. This is the result of the quantum capacitance effect, in which the Fermi level of graphene can be tuned by the accumulation and depletion of charge carriers within the graphene[104, 105]. The impedance spectroscopy was performed to study this effect, collected in room temperature using an Agilent 4284A Precision LCR meter with the oscillation amplitude set to 10 mV. The frequency response of the resistance and reactance across the gap was measured as shown in Fig. 3.11. At low frequencies, the resistance, Z' saturates while the reactance $-Z''$ tends to zero. As the oscillation frequency is increased, Z' is reduced towards zero, and a single peak of $-Z''$ emerges.

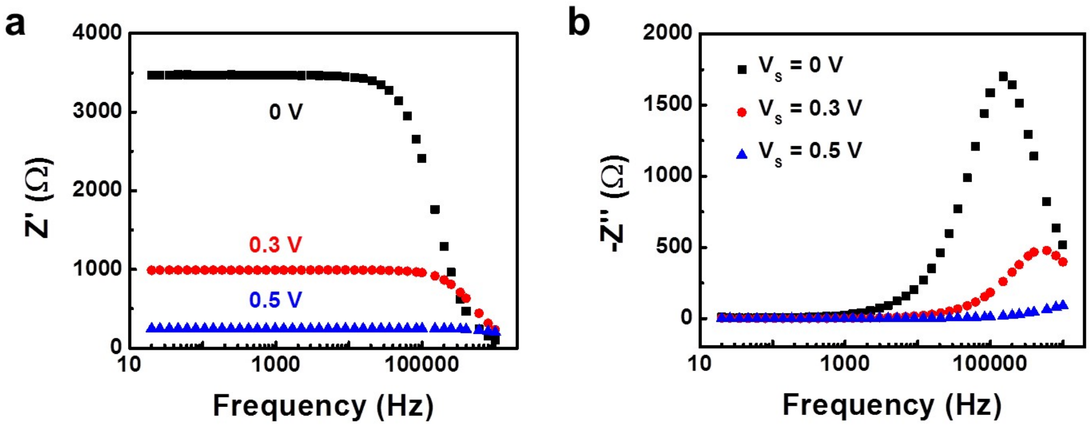

Figure 3.11 Impedance spectroscopy of the graphene vertical tunneling structure. a, Resistance (Z') as a function of frequency for various applied sample biases. **b,** Reactance ($-Z''$) as a function of frequency for various applied sample biases.

The Nyquist plot exhibits a single semicircle that passes through the origin of the plot at the high frequency limit (Fig. 3.12). This behavior can be readily described by an equivalent circuit consisting of a resistor and a capacitor in parallel (solid curves), and the equivalent circuit is plotted in the inset of Fig. 3.12, where C_{Gr} and R_{Gr} represent the capacitance and resistance of the tunneling junction respectively, and C_{Pad} accounts for the capacitance from the surrounding metal contact pads for external circuit connection.

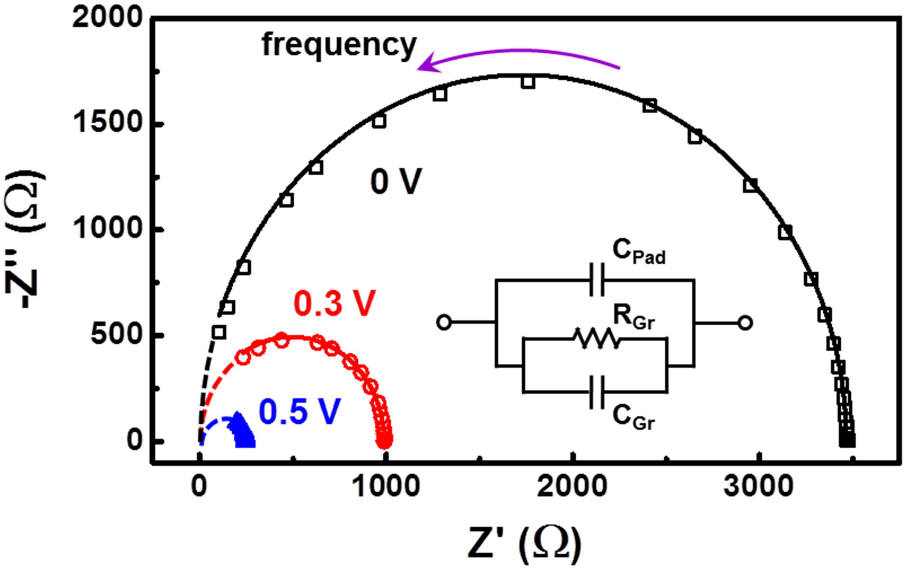

Figure 3.12 Nyquist plot showing $-Z''$ versus Z' for various applied sample biases. A single semi-circle is observed for each curve, and the diameter of the semi-circle is found to decrease with increasing sample bias, consistent with the tunneling nature of the junction. The purple arrow shows the direction of decreasing frequency. Inset shows the proposed equivalent circuit of the graphene vertical structure, in which a resistor, R_{Gr} and a capacitor, C_{Gr} connected in parallel are used to describe the tunnel junction, while C_{Pad} accounts for the capacitance of the contact pads.

The value of R_{Gr} and $C_{total} = C_{Gr} + C_{Pad}$ can be obtained by fitting the frequency response of the reactance for different biases, and the results are shown in Table 3.1. The decrease of the R_{Gr} with increasing bias is expected for the tunneling dominated (as opposed to leakage dominated) transport behavior. The capacitance of the contact pads, C_{pad}, can be experimentally extracted by measuring devices having different areas of the tunnel junction, as shown in Fig. 3.13 and is determined to be 86 pF. It is also found that C_{pad} is independent of the applied bias in the voltage range investigated (inset of Fig. 3.13). Deducting this contribution from C_{total}, C_{Gr} can be determined.

Table 3.1 Summary of the values of R_{Gr}, C_{total} and C_{Gr} at various sample biases for a tunnel junction area of 2.7 × 10^{-4} cm^2.

	R_{Gr} (Ω)	C_{total} (pF)	C_{Gr} (pF)
0 V	**3428**	**306**	**220**
0.3 V	**968.4**	**317**	**231**
0.5 V	**219.0**	**385**	**299**

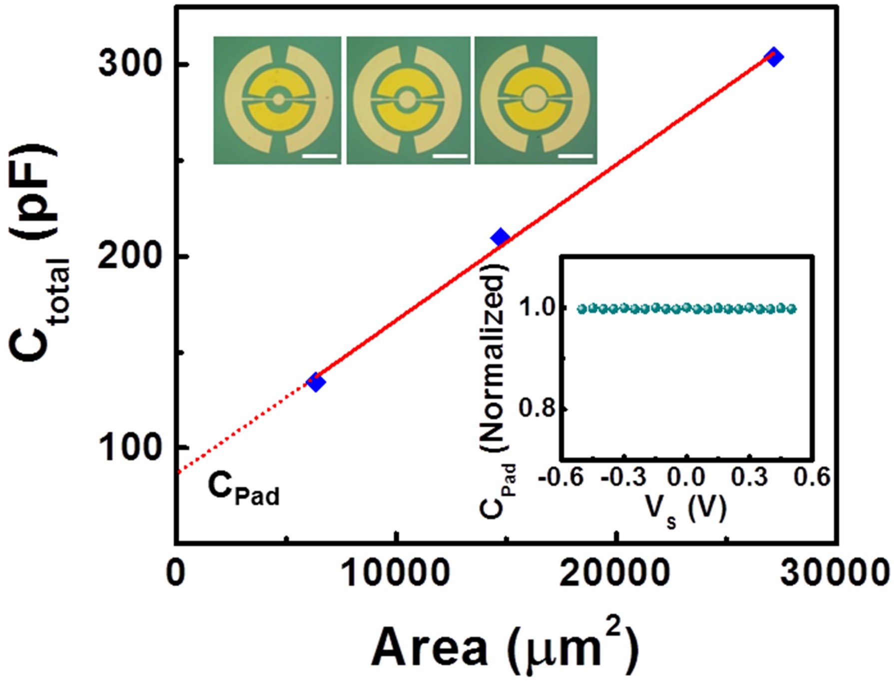

Figure 3.13 The measured parallel capacitance ($C_{total} = C_{Gr} + C_{Pad}$) as a function of the area of the graphene tunnel junction. Insets show optical images of tunnel junctions with different tunnel areas (scale bars, 300 μm) and normalized C_{Pad} as a function of the applied DC bias. The pad capacitance, C_{Pad} is found to be independent of the applied DC bias in the voltage range measured due to the fact that the silicon substrate is heavily doped, and therefore can be treated as a metal.

Deducting the contribution of C_{pad} from C_{total}, C_{Gr} can be determined. The experimental determined C_{Gr} as a function of the V_S is shown in Fig. 3.14. Distinct from a typical parallel plate capacitor, the capacitance of the graphene vertical tunneling structure is a sensitive function of the bias due to the quantum capacitance. Unfortunately, the well-established quantum capacitance model, which can be applied to describe the lateral charging behavior of the graphene and other 2D materials[106, 107], is unsuitable for the vertical structure as it cannot explain the non-linearity in Fig. 3.14.

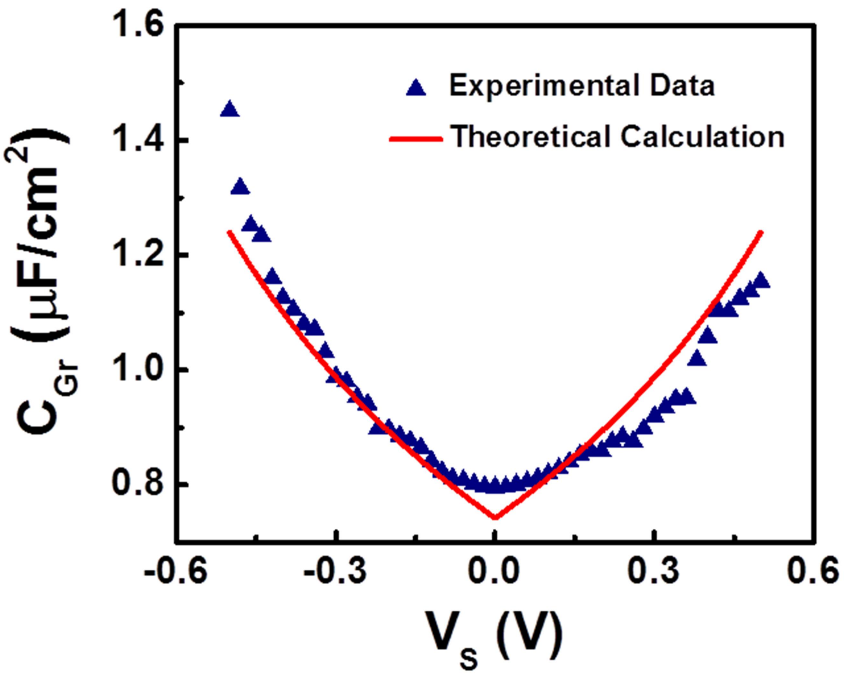

Figure 3.14 Capacitance-voltage characteristic of the graphene vertical tunnel junction. Experimental data of C_{Gr} as a function of the applied sample bias (blue triangles) plotted alongside with the theoretically calculated curve (red solid line).

Herein, we construct a new model to describe the capacitance-voltage characteristic of the graphene and the vdW gap in the vertical direction, which takes into account the atomic thickness and DOS of graphene, as well as the asymmetrical interfaces on the two sides of graphene. The schematic energy diagram is shown in Fig. 3.15a for a positive bias. The slight shift of the Fermi level relative to the Dirac point (~70 meV) is ignored for simplicity. With the application of V_S, a potential drop, ψ_{gap}, results across the fully preserved vdW gap between the Si (n^{++}) interface and the graphene, and charge is induced in the graphene sheet. The limited DOS in the graphene will result in a downward shift of the graphene Fermi level relative to the Dirac point (ψ_{Gr}); this shift is also equal to the voltage drop across the graphene/Cr interface. This is due to the fact that the Fermi levels of the graphene and Cr are aligned as a result of the orbital hybridization between the two materials[108].

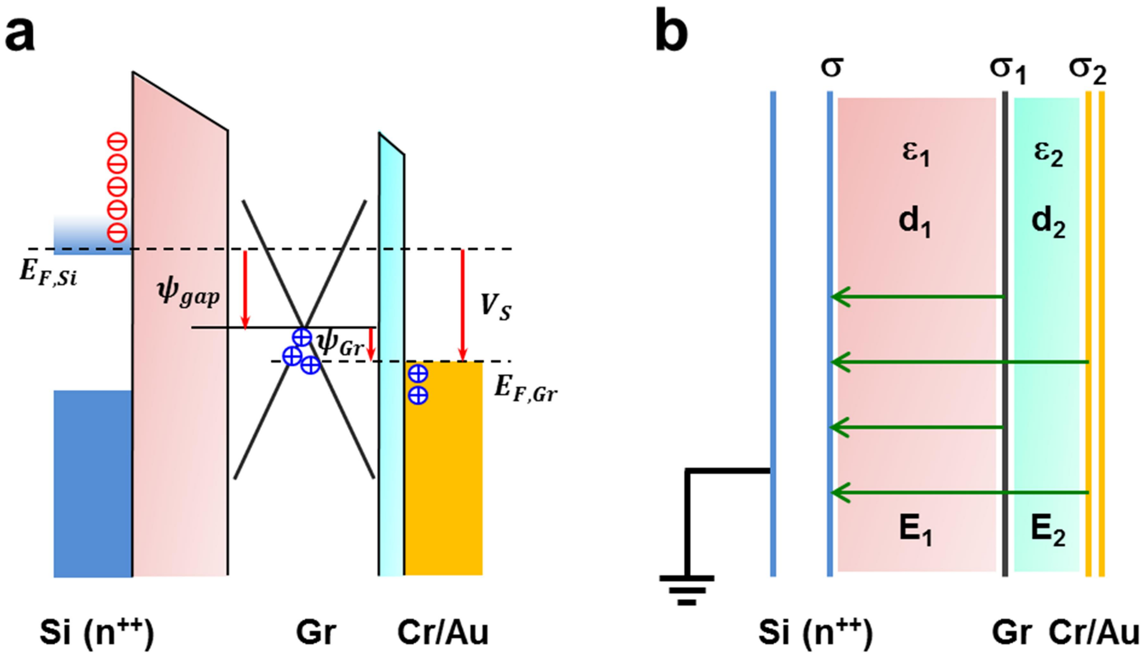

Figure 3.15 Capacitance model of the graphene vertical tunnel junction. a, Schematic diagram depicting the band diagram of the graphene vertical structure. As a result of the limited DOS of graphene, the induced charge is only partially supplied by the graphene, while the rest is supplied by the Cr/Au electrode. This leads to voltage drops on both the vdW gaps between Si (n^{++}) and the graphene, ψ_{gap}, and between the graphene and Cr interface, ψ_{Gr}, the sum of which equals the applied bias. **b,** Schematic diagram of the graphene vertical tunneling junction showing the charge stored on the Si electrode (σ), the graphene single layer (σ_1) as well as on the Cr electrode (σ_2). The graphene cannot completely shield the electric field lines (green) from Cr/Au due to its limited DOS.

Another way of looking at the distribution of the voltage drop across the two interfaces is to consider the charge and electric field distributions, as depicted in Fig. 3.15b. The induced charge is only partially located at the graphene (σ_1), due to its linear DOS, with the rest at the Cr/Au electrode (σ_2), and the sum of which equals the induced charge on the Si electrode ($\sigma = \sigma_1 + \sigma_2$). Thus, the effective electric filed at the two interfaces can be defined using the Gauss's Law as:

$$E_1 = \frac{\sigma}{\varepsilon_1} \qquad E_2 = \frac{\sigma_2}{\varepsilon_2} \tag{3.9}$$

and the voltage drop across the Si/graphene interface, ψ_{gap} can be subsequently obtained as:

$$\psi_{gap} = E_1 d_1 = \frac{\sigma d_1}{\varepsilon_1} \tag{3.10}$$

in which d_1 and ε_1 represent the effective thickness and permittivity of the vdW gap between Si (n^{++}) and graphene. The interface between graphene and the Cr/Au electrode can be similarly described, with the voltage drop equals to:

$$\psi_{Gr} = E_2 d_2 = \frac{\sigma_2 d_2}{\varepsilon_2} = \frac{(\sigma - \sigma_1) d_2}{\varepsilon_2} \tag{3.11}$$

with d_2 and ε_2 representing the effective thickness and permittivity of the hybridized graphene/Cr interface. The charge area density on graphene, σ_1, can be obtained by integrating the DOS of graphene over the range of 0 to $e\psi_{Gr}$:

$$\sigma_1 = e\int_0^{e\psi_{Gr}} f(E)\rho_{Gr}(E)dE = \frac{1}{2}\xi {\psi_{Gr}}^2 \tag{3.12}$$

where

$$\xi = e^2 \frac{2}{\pi} \frac{e}{(\hbar v_F)^2} \tag{3.13}$$

In this expression, $\hbar$ is the reduced plank constant, v_F is the Fermi velocity of the graphene, and V_{Gr} is the Fermi level change in graphene relative to the Dirac point. Note that several approximations are made in obtaining this expression. First, the inherent p-doping of graphene is ignored since the Dirac point has been experimentally determined to be very close to the Fermi level of the graphene. Secondly, the Fermi levels of the graphene and the Cr electrode line up because of the hybridization between the two materials. Finally, a step-like Fermi-Dirac distribution is assumed.

The applied voltage equals the voltage drop across the Si/graphene interface plus that across the graphene/Cr interface:

$$|V_S| = \psi_{gap} + \psi_{Gr} = \frac{\sigma d_1}{\varepsilon_1} + \frac{\sigma d_2}{\varepsilon_2} - \frac{\xi d_2}{2\varepsilon_2}\left(|V_S| - \frac{\sigma d_1}{\varepsilon_1}\right)^2 \qquad (3.14)$$

$$= \frac{\sigma}{C_1} + \frac{\sigma}{C_2} - \frac{\xi}{2C_2}\left(|V_S| - \frac{\sigma}{C_1}\right)^2 \qquad (3.15)$$

C_1 and C_2 are introduced to simplify our expression, and correspond to the effective geometric capacitances of the two interfaces. Solving for σ (V_S) results in:

$$\sigma(V_S) = \frac{C_1^2 C_2}{\beta}\left\{\frac{1}{C_1} + \frac{1}{C_2} - \frac{\xi|V_S|}{C_1 C_2} + \sqrt{(\frac{1}{C_1} + \frac{1}{C_2})^2 - 2\left(\frac{1}{C_1} + \frac{1}{C_2}\right) \times \frac{\xi|V_S|}{C_1 C_2} - \frac{2\xi|V_S|}{C_1^2 C_2}}\ \right\} \qquad (3.16)$$

and the expression for the capacitance across the entire graphene vertical tunneling structure can be obtained:

$$C_{Gr} = \frac{d\sigma}{dV_S} = \frac{\left(\frac{1}{C_1} + \frac{1}{C_2}\right) C_1 + 1}{\sqrt{(\frac{1}{C_1} + \frac{1}{C_2})^2 - 2\left(\frac{1}{C_1} + \frac{1}{C_2}\right) \times \frac{\xi|V_S|}{C_1 C_2} - \frac{2\xi|V_S|}{C_1^2 C_2}}} - C_1 \qquad (3.17)$$

The experimental data in Fig. 3.14 can be readily fitted to this expression, shown as the red curve, except for a slight discrepancy near the zero bias, which has been observed and attributed to charge impurities in the graphene sheet by previous works[105-107]. The fitted C_1 is found to be significantly smaller than C_2, characteristic of a full vdW gap at the Si/graphene interface and an almost disappearing vdW gap at the Cr/graphene interface, respectively. This asymmetry in the two interfaces, together with the quantum capacitance of the graphene, is the physical origin of the asymmetric nature of the tunneling J-V_S characteristics discussed earlier. This is the first model, to the best of our knowledge, to explain the effect of graphene quantum capacitance on purely vertical transport processes, whereas previous ones focus on lateral depletion of graphene due to quantum capacitance.

3.4 Vertical Tunneling across Decoupled Multi-layer Graphene

Vertical stacks of decoupled graphene sheets can be produced by stacking individual graphene sheets using the wet transfer approach. This is an artificial structure different from naturally occurring graphite crystals due to the lack of perfect alignment and contact between individual layers. This structure can be used as a tunable tunnel barrier and electrical contact, dependent of the number of graphene sheets incorporated. Here, we demonstrate decoupled graphene stack of two and three layers as a proof of concept, and compare their tunneling behavior to that of monolayer graphene.

For the fabrication of decoupled multi-layer graphene tunneling structure, graphene is wet transferred onto the Si (n^{++}) substrate patterned with circular injection areas, and this process is repeated until the desired number of layers is reached. This is followed by the deposition of metal electrodes. Similar to our investigation of the monolayer graphene, a ‘top contact’ as well as a ‘side contact’ structure are studied. For the ‘top contact’ structure, electrons tunnel vertically across the graphene sheets and are collected by the Cr/Au electrode vertically aligned to the injection area. For the ‘side contact’ structure, on the other hand, the electrons are forced to relax to the eigenstates of graphene and propagate laterally before collected.

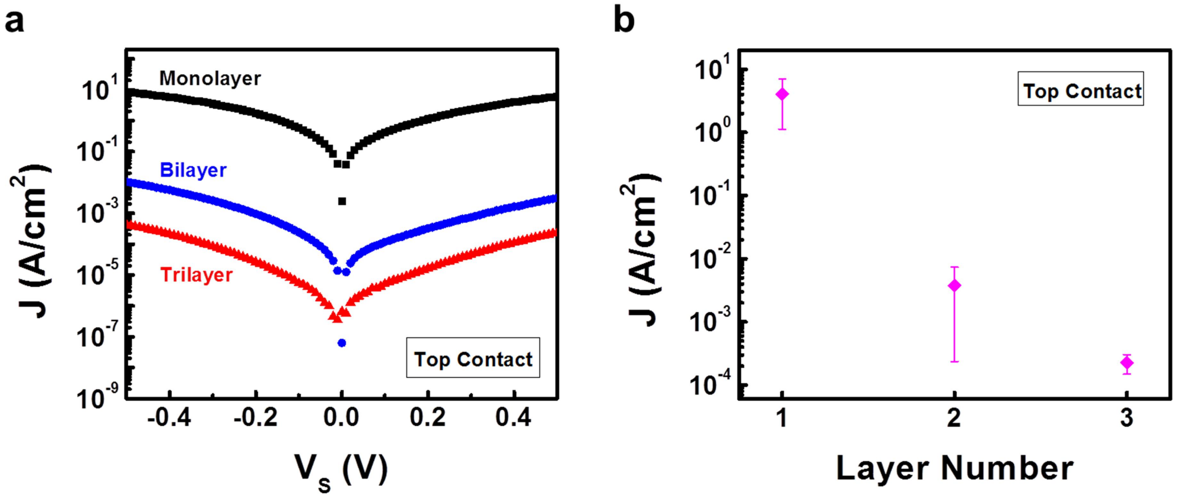

Figure 3.16 Tunneling characteristics of the 'top contact' graphene tunneling structure. a, J-V_S characteristics of vertical tunneling through monolayer, bilayer and trilayer graphene. The device structure is a vertical stack consisting of Si (n^{++})/few layer graphene/Cr/Au, similar to that shown in Fig. 2.24a. Lower current density is observed for thicker graphene, due to the increase in the effective barrier thickness for the direct tunneling process. **b**, J as a function of layer number for the 'top contact structure', i.e., vertical transport across the few layer graphene.

J-V_S characteristics of the 'top contact' monolayer, bilayer and trilayer decoupled graphene sheets are shown in Fig. 3.16a. Consistent with our understanding of the vertical transport across graphene, J decreases dramatically with increasing layer number, equivalent to an increase in the thickness of the barrier in the direct tunneling process. J at 0.5 V for a number of devices is plotted in Fig. 3.16b versus the layer number. J decreases from around 10 A/cm^2 for monolayer, to around 10 mA/cm^2 for bilayer and 0.1 mA/cm^2 for trilayer at a tunneling bias of 0.5 V. The tunneling behavior can be described using the direct tunneling model discussed in detail in section 2.4.3, and the result of the theoretical calculation is shown along with the experimental data in Fig. 3.17a-c.

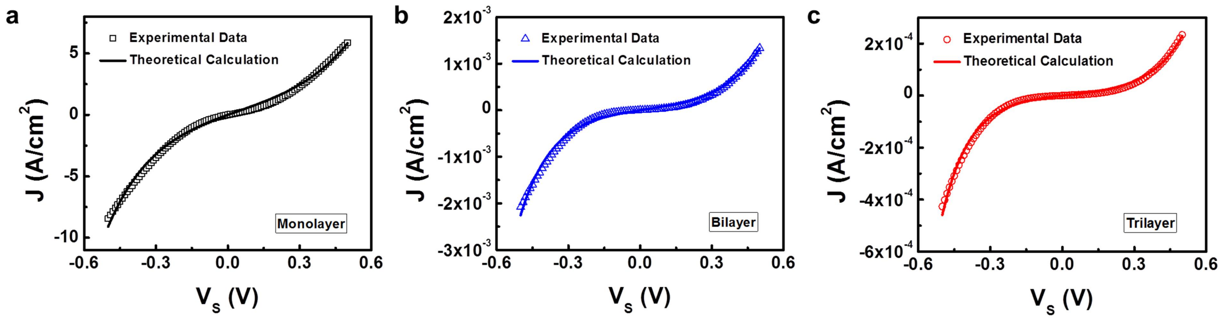

Figure 3.17 Experimental J-V_S curves shown along with theoretical calculation based on the direct tunneling model. a, Experimental (black open dots) and theoretical calculated (black solid line) J-V_S characteristics of vertical tunneling across monolayer graphene. **b**, Experimental (blue open triangles) and theoretical calculated (blue solid line) J-V_S characteristics of vertical tunneling across bilayer decoupled graphene. **c**, Experimental (red open circles) and theoretical calculated (red solid line) J-V_S characteristics of vertical tunneling across trilayer decoupled graphene.

Three fitting parameters are used for each case, the barrier thickness (d), the effective barrier height ($\bar{\varphi}$) and the asymmetry factor (f) to account for the non-uniform potential drop across the barrier. The fitting parameters for the three cases along with the goodness of fit (R-squared) are summarized in Table 3.2. With each additional layer, the barrier thickness increases by a few angstroms, consistent with literature reports of experimentally determined graphene thickness[3]. The monolayer graphene exhibit an equivalent barrier thickness of around 2 nm, consistent with the surface roughness of Si (around 1 nm) plus the graphene thickness. The effective barrier height, on the other hand, is not a sensitive function of the layer number.

Table 3.2 Parameters for the theoretical calculation of the direct tunneling processes across decoupled multi-layer graphene and the R-squared for the fitting to experimental results.

Material	***d*** **(nm)**	$\bar{\varphi}$ **(eV)**	***f***	***R***
Monolayer	2.5	2.1	0.45	0.9954
Bilayer	3.4	1.7	0.46	0.9942
Trilayer	3.7	1.6	0.46	0.9952

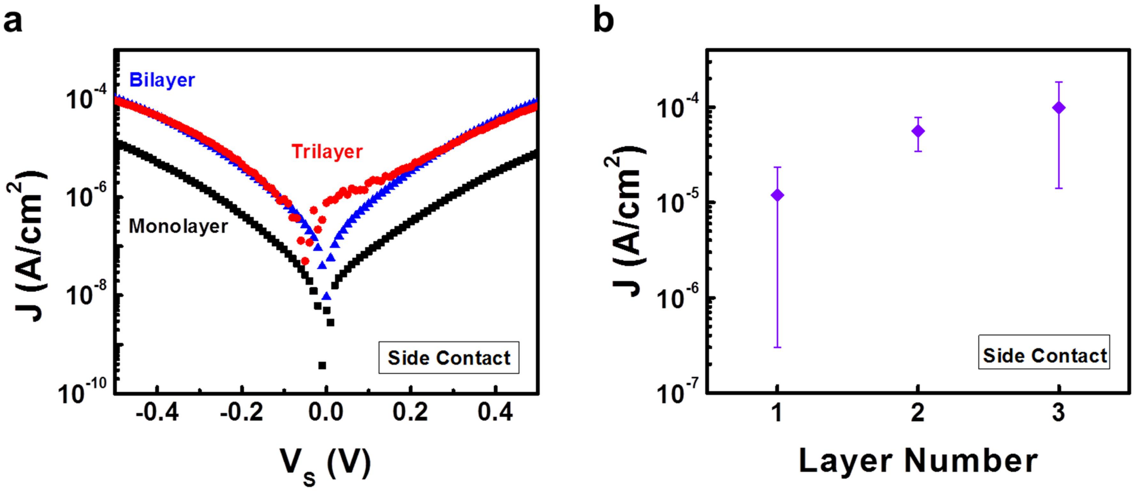

Figure 3.18 Tunneling characteristics of the 'side contact' graphene tunneling structure. a, J-V_S characteristics of the side contact structure of monolayer, bilayer and trilayer graphene. The device structure is similar to that shown in Fig. 3.1b. **b**, J as a function of layer number for the 'side contact' structure, i.e., vertically transporting electrons are required to relax to the eigenstates of few layer graphene and then propagate laterally before collected. An increase in the J is observed with increasing layer number, as a result of the increase in the interaction cross sections between the electrons and graphene sheets.

For the 'side contact' structure, J increases for increasing layer number, as shown in Fig. 3.18a. J as a function the number layer is shown in Fig. 3.18b. During measurement, we have found that J of the 'side contact' structure varies dramatically with graphene quality, condition of the graphene surface (with or without passivation layer), fabrication process and measurement conditions. Thus, it is worth noting that only devices fabricated from sections of the same graphene simultaneously are compared here. For the trilayer case, the current levels of the 'side contact' and the 'top contact' structure are comparable, an indication of saturated interaction between the injected electrons and the graphene sheet. Next we will show that this effect manifest itself in the first order ETS of multi-layer decoupled graphene sheets.

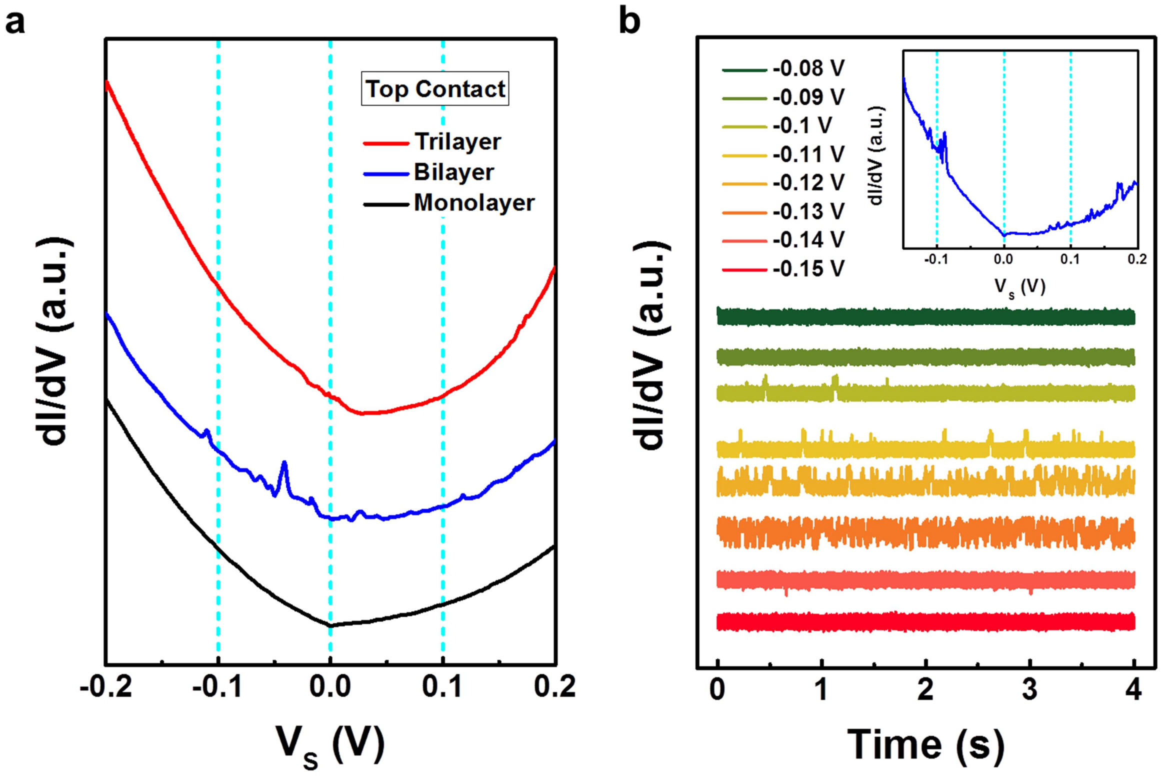

Figure 3.19 First order ETS spectrum of multi-layer decoupled graphene sheets. a, First order ETS spectrums for monolayer, bilayer and trilayer decoupled graphene sheets showing a transition from one without signature of the Dirac cone to one with. **b**, Random telegraphic signal noise observed in a range of sample biases for bilayer graphene sample. Inset shows the corresponding first order ETS spectrum.

The first order ETS spectrum, i.e., the conductivity as a function of sample bias provides convoluted information on the various processes limiting the tunneling process across a barrier. For monolayer graphene, due to the limited interaction between the vertically tunneling electrons and the lateral band structure of graphene, the linear DOS of graphene does not limit the transport. Rather, the vertical transport is determined by the DOS of the two electrodes sandwiching graphene, as well as the bias dependent transmission coefficient. As a result, a first order ETS with a global minimum at zero sample bias is observed, as shown by the black curve in Fig. 3.19a. For the trilayer case on the other hand, much higher degree of interaction is observed, as shown by the red curve in Fig. 3.19a, which is consistent with the previous current level analysis. The position of the Dirac point relative to the Fermi level of graphene is directly correlated to the minimum point in the first order ETS at a positive sample bias, indicative of a p-doped graphene. The bilayer is a transitional state between the monolayer case and the trilayer case in the general contour of the curve (blue curve in Fig. 3.19a), with additional peaks and valleys, signature of traps in the tunnel barrier. To confirm the correlation between the observed features and a trap mediated tunneling process, the random telegraphic noise signal is recorded with an oscilloscope in the sample bias range where the peaks and valleys are observed. The telegraphic noise as a function of time is shown in Fig. 3.19b, with the corresponding ETS spectrum given in the inset. Sudden step-like transitions are observed in the sample bias range probed, signature of the random trapping and release of charge carrier during the tunneling process. While the exact origin of the trap states remain unclear at the moment, we speculate that investigation of these fine features in the ETS spectrum of vertical tunneling across vdW material could be the key to understanding the detail interaction between the vertical propagating electrons and the atomic layers.

3.5 Summary

In summary, we systematically studied the out of plane transport process across graphene. It is found that graphene acts as a tunnel barrier for vertically propagating electrons. In the single layer graphene case, when lateral transport was eliminated in a purely vertical structure, the tunneling electrons interact weakly with the semi-metallic graphene band structure due to the atomic thickness, as well as the mismatch of the transverse momentum. Instead, the graphene acts as a very thin grid and is transparent to vertically tunneling charge carriers, meanwhile, it can still modulate the potential and charge distribution across the tunnel barrier via the quantum capacitance effect and thus control the tunneling current. Multi-layer graphene exhibits an increase in the interaction between the out of plane transport and the in plane band structure, which is shown by tracing the evolution of the low temperature ETS. Our study highlights the potential of vdW materials for use as electron/spin tunnel barriers for high frequency electronics and spintronics. It can also open new avenues for the design and analysis of 2D material heterostructures as well as 2D/bulk material heterostructures.

Chapter 4 High Current Density Graphene Base HETs (GBHETs)

4.1 Motivation

Graphene's unprecedented high mobility has triggered excitement in its application in high speed electronics[5, 109, 110]. Its lack of a bandgap, however, greatly limits its potential application as the channel material in traditional CMOS technology[111]. More recently, graphene has been applied as the base material of vertical transistors such as hot electron transistors (HETs)[80, 91], and potential THz operation has been demonstrated through theoretical simulation[78]. The HET is operated by controlling the flow of hot electrons from the emitter to the collector by tuning the potential of the base region. Similar to BJTs in terms of device structure and equivalent circuit, the continued interest towards this device structure is fueled by the hopes of producing a device that is even faster than the BJTs[72]. In order to achieve a high operation frequency for HETs, a short base transit time and a low base resistance is simultaneously required. In addition to being ultra-thin and highly conductive, the base material also needs to be pin-hole free, to avoid leakage across the emitter and the collector. Graphene is an ideal candidate, with its atomic thickness and high carrier mobility, as well as the ease of growing large area, pin-hole free graphene sheets using CVD.

Experimental demonstrations of such devices have been reported by several groups. Zeng *et al.* injected hot electrons from a heavily doped Si region through SiO_2 as the tunnel barrier into graphene, where they either pass through another barrier (the filter barrier) before being collected, or are scattered back into the base region to form the base current[79]. The injected current density is limited to 10^{-8} A, as a result of the thick SiO_2 tunnel barrier. The turn-on voltage is much higher compared to the filter barrier height, which could be attributed to the energy loss of hot electrons in the SiO_2 tunnel barrier[79]. An alternative structure uses MoS_2 as the base material with record high common base current gain, however with low injection current levels due to the high contact resistance to MoS_2[81].

In reports of graphene vertical transistors so far, graphene has been treated equivalent to an ultra-thin metal. However, due to the anisotropy in the atomic structure of vdW materials and the presence of the vdW gaps, carrier transport in the out-of-plane direction is markedly different from that of the lateral direction. In particular for graphene, while it is a semi-metal with ultra-high mobility in the lateral transport, the vertical transport exhibits a tunneling behavior, as a result of the presence of the vdW gaps and the atomic thickness of graphene, leading to minimal interaction between the vertically propagating carriers and the graphene lateral band structure. This has led to discussions on the contacts to graphene as limited by the transport across vdW gaps[61], as well as graphene's application as magnetic tunnel barriers[59].

In this chapter, we study the carrier injection through the vdW gap formed inherently at the Si (n^{++})/graphene interface as an atomic scale tunnel barrier, thus eliminating the need for the fabrication of artificial tunnel barriers. The Si-graphene vertical transistor functions like an atomic size vacuum tube, where the carriers injected through the atomic scale 'air gap' are either 'captured' by the graphene (similar to the grid in vacuum triode), or are collected by the collector electrode. Current densities as high as 10 A/cm^2 are injected through the vdW gap, and the device exhibits a turn-on voltage comparable to the predicted filter barrier height, indication of a low loss injection for the HETs.

4.2 Basic Operation Principles of HETs

In the operation of HETs, electrons are injected from the emitter, through the tunnel barrier, into the base region, where they either pass through the filter barrier and get collected by the collector, or are reflected back and form the base current. This process is illustrated in Fig. 4.1a, together with a schematic diagram showing the cross-section of a representative device. The HET is sometimes considered as a unipolar version of the BJT, due to their striking resemblance in the device structure (as shown in Fig. 4.1b for an npn BJT), but they are fundamentally different in terms of the origin of the base current. In BJTs, the base current arises from the recombination current with carriers being the opposite sign of the carriers injected in the base region; meanwhile for HETs, the base current consists of injected carriers that have been reflected back by the filter barrier, the base-filter barrier interface, or the filter barrier-collector interface.

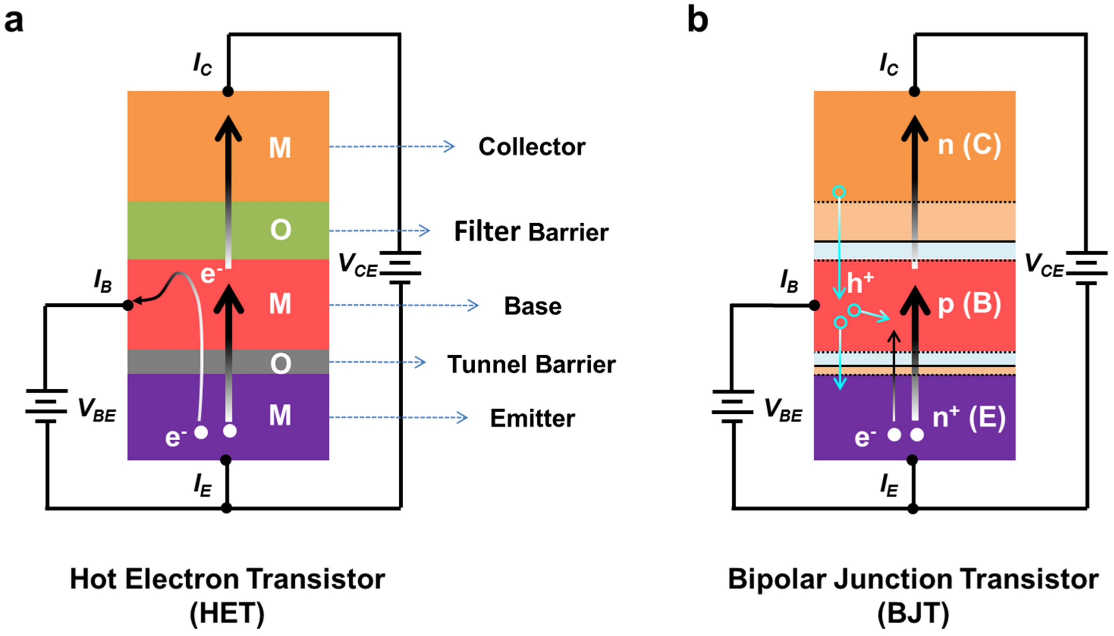

Figure 4.1 The device structures of HETs and its analogy to BJTs. a, Schematic diagram showing the cross section of a MOMOM HET device. Black arrows represent the flow of electrons. **b**, Schematic diagram showing the cross section of a npn BJT device. Black arrows represent the flow of electrons, and the blue arrows represent the flow of holes.

The band structure of the HETs are plotted to illustrate the thermal equilibrium condition (Fig.

3.2), as well as the off (Fig. 3.3) and on state (Fig. 3.4) using MOMOM HETs as an example. Alternative structures such as metal-insulator-metal-semiconductor (MOMS) and semiconductor-metal-semiconductor (SMS) can be discussed similarly. In thermal equilibrium, the Fermi level of the emitter, base and collector are aligned as the materials are in contact, as shown in Fig. 4.2. When a bias lower than the filter barrier is applied across the emitter-base junction (V_{EB}), a small leakage current flows across the filter barrier, the device is in 'off' state as the hot electrons does not have enough energy to reach the collector, as shown in Fig. 4.3. Only when a large enough bias is applied across the emitter-base junction, hot electrons can clear the filter barrier and reach the collector. Ideally, the base region is thin enough for the hot electrons to traverse the base region ballistically and the device is in 'on' state. Due to quantum mechanical reflection and various scattering processes, a portion of the hot electrons will be reflected back into the base region and becomes the base current (as shown in Fig. 4.4)

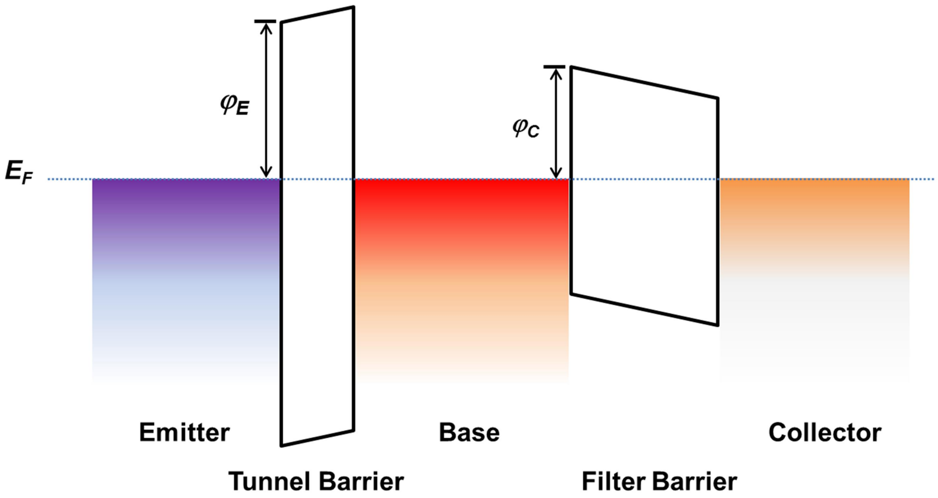

Figure 4.2 Energy band diagram of a typical MOMOM HET in thermal equilibrium. The tunnel barrier height and filter barrier height is denoted as φ_E and φ_C respectively.

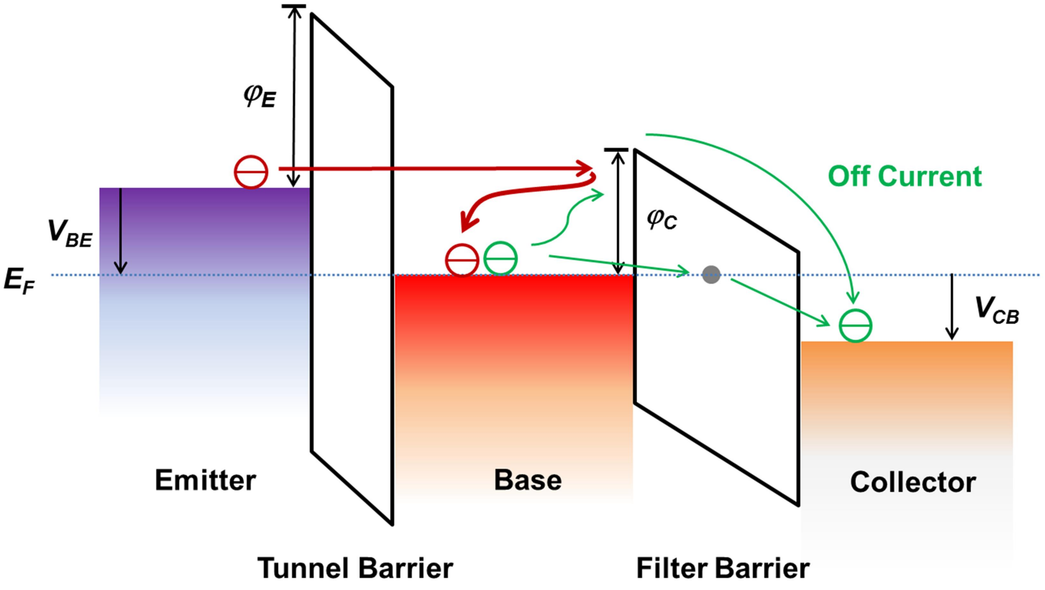

Figure 4.3 Energy band diagram of a typical MOMOM HET in the off state. The hot electrons does not have enough energy to clear the filter barrier. When a bias is applied across the base-collector junction, a small current flows across the filter barrier due to leakage pathways and thermal excitations.

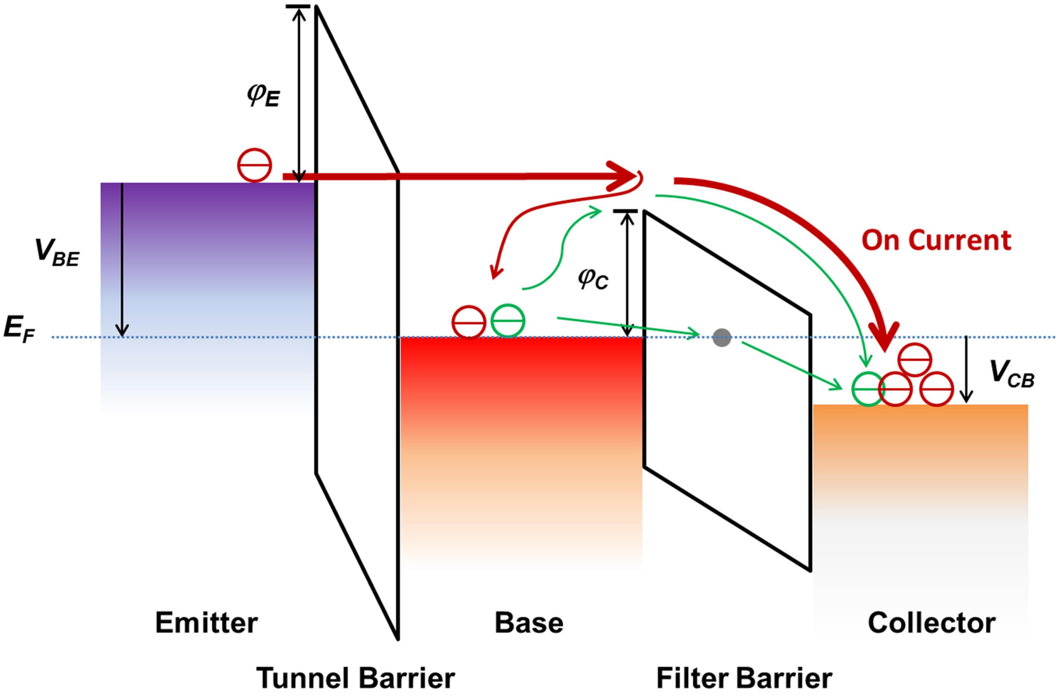

Figure 4.4 Energy band diagram of a typical MOMOM HET in the on state. Hot electrons

are injected through the tunnel barrier with sufficient energy to pass the filter barrier and get collected by the collector electrode. A small portion of the hot electrons will be reflected back into the base region to form the base current, as a result of quantum mechanical reflection and scattering processes.

Two measurement geometries are commonly used to characterize HETs, identical to that of BJTs: the common base measurement (as shown in Fig. 4.5a) and the common emitter measurement (Fig. 4.5b). The common base and the common emitter current gain are among the most important figures of merit for HETs, and are defined as following:

$$\alpha\ (common\ base\ current\ gain) = \frac{I_C}{I_E} \tag{4.1}$$

$$\beta\ (common\ emitter\ current\ gain) = \frac{I_C}{I_B} \tag{4.2}$$

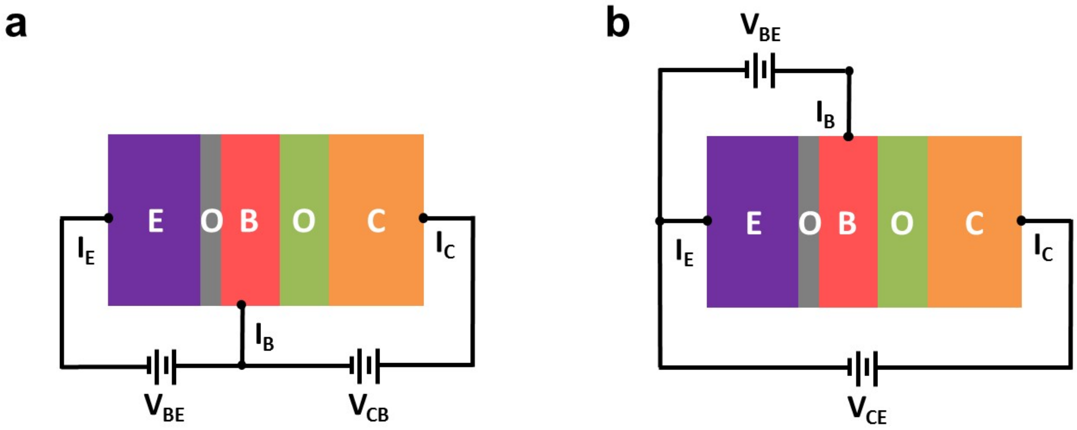

Figure 4.5 Common measurement setups for HETs. a, The common base transistor circuit. **b,** The common emitter transistor circuit.

4.3 Device Structure Design for the High Current Density GBHETs

4.3.1 Ultra-thin Tunnel Barrier for Improved Emitter Current Density (J_E)

Similar to the graphene tunneling structures, Si (n^{++}) is chosen as the emitter electrode, due to the ease to form an atomically flat surface. In previous works, a thin SiO_2 layer is deposited as the tunnel barrier on top of the Si (n^{++}) electrode using a rapid thermal processing (RTP-600xp) system, and the thickness of the oxide layer is controlled to be around 3 nm[79, 81]. This results in an injection current density of around 10^{-4} A/cm^2 for graphene, and 10^{-6} A/cm^2 for MoS_2. Further improving control of the RTP process is possible, and we are successful in achieving deposition of 1 nm of SiO_2 on top of Si (n^{++}), by placing HF treated Si substrate in the RTP furnace and depositing at 800 °C for 3 second. The tunneling current density across this ultra-thin tunnel oxide can be as high as 10 A/cm^2 at 2 V, as shown by the red curve in Fig. 4.6.

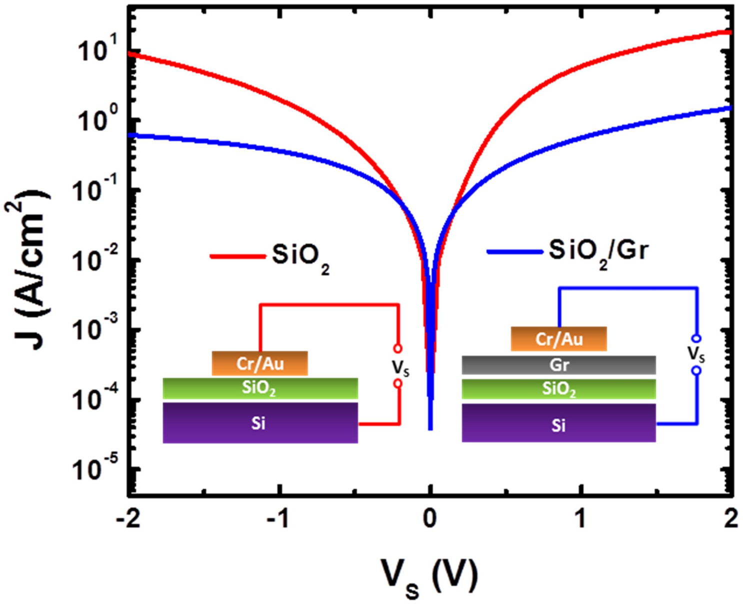

Figure 4.6 *J-V_S* characteristics of vertical tunneling across ultra-thin oxide (red) and ultra-thin oxide plus graphene (blue). Insets show the schematic diagrams of the corresponding structures.

As have been discussed in Chapter 3, the vertical transport across graphene is of a tunneling nature, different from the semi-metallic behavior commonly observed in the lateral direction. Therefore when graphene as the base material is added on top of the ultra-thin oxide, vertical tunneling current density is reduced by more than one order of magnitude as shown by the blue curve in Fig. 4.6.

Similar phenomenon is observed for *h*-BN as the tunnel barrier. CVD grown *h*-BN using Cu foil as the substrate can be wet transferred onto Si (n^{++}) substrates using similar processes as the transfer of graphene. For tri-layer *h*-BN, the tunneling current density across it is around 100 A/cm^2 at 1 V as shown in Fig. 4.7. However, when graphene is added onto the stack to assume the role of the base material, the current density drops to around 1 A/cm^2, as shown in Fig. 4.7.

Based on these two observations, it can be concluded that graphene's role as a tunnel barrier in the vertical transport needs to be taken into account when designing the emitter-base junction of GBHETs, as well as when evaluating the injection current achievable.

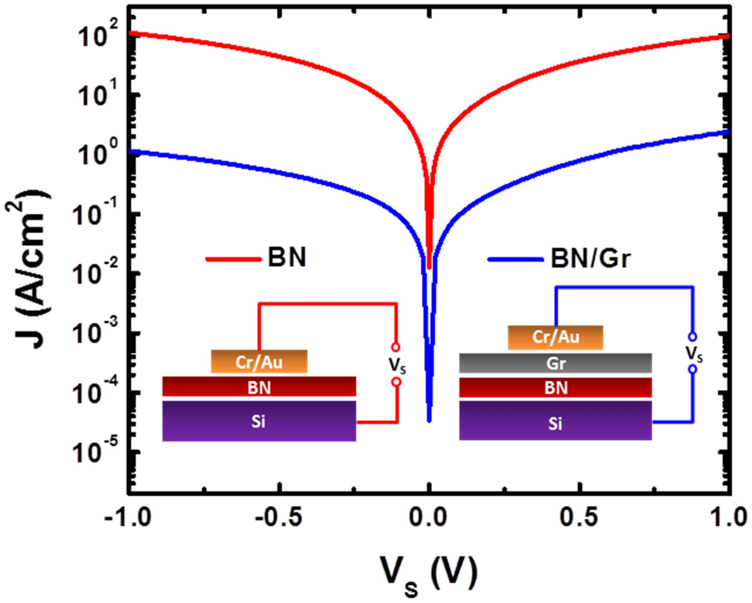

Figure 4.7 J-V_S characteristics of vertical tunneling across tri-layer *h*-BN (red) and *h*-BN

plus graphene (blue). Insets show the schematic diagrams of the corresponding structures.

4.3.2 Graphene and the vdW Gap as the Tunnel Barrier

To maximize the vertical injection current, graphene is placed directly into contact with Si (n^{++}) as the emitter-base junction. The vdW gap formed between the atomically flat Si surface and graphene, as well as graphene itself can induce a tunneling behavior for hot electrons injected from the Si (n^{++}) emitter upon the filter barrier. As discussed in detail in Chapter 3, due to the large momentum mismatch between Si and graphene as well as the atomic thickness of graphene, most of the injected hot electrons pass through graphene without interacting with the lateral band structure of graphene, which is ideal for achieving a high current gain for HETs. The injected current density (J_E) can be as high as 100 A/cm^2, as illustrated by the black curve in Fig. 4.8a.

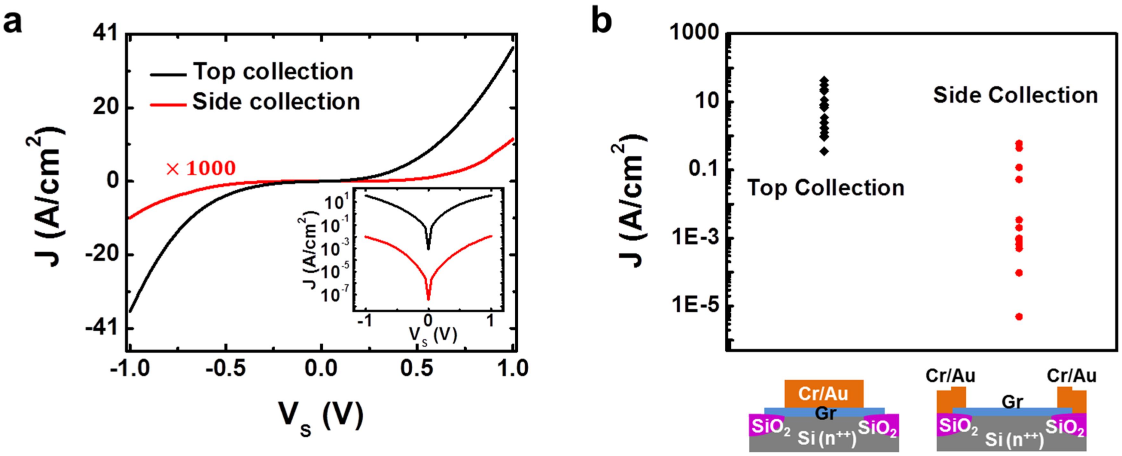

Figure 4.8 Comparison of the top and side collection of electron tunneling into graphene. a, J-V_S characteristics for the top and side collection structure. Inset shows the same curve in logarithmic scale. **b,** Distribution of the current density for the top collection and side collection plotted together for comparison. All the current density is measured at a bias of 0.5 V. Schematic diagrams of the two structures are also given.

The lateral current to the base contact on the other hand, is dependent on the process in which the hot electrons relax to the states near the K (K') points of graphene with the assistance of phonons or other elemental excitations. This process occurs at a much smaller rate, as can be seen from the significantly smaller current density for the ‘side contact’ structure, as shown by the red curve in Fig. 4.8a. Therefore, the hot electrons reflected back into the base region needs to acquire the lateral momentum corresponding to the Dirac-Fermions in graphene at K (K’) reciprocal lattice points to propagate laterally through the base region to the base contact, via a phonon or other elemental excitations assisted processes. Note these processes is very sensitive to material quality, as well as device processing and measurement conditions, therefore a much wider statistical distribution in the current density of the ‘side’ contact structure is observed compared to that of the vertical tunneling case (Fig. 4.8b).

4.3.3 Filter Barrier Design

The HETs are switched on when the hot electrons acquire enough energy to surpass the filter barrier and reach the collector, controlled by the application of V_{BE}. The V_{BE} at which the HET is turned on has been found to be significantly higher than the filter barrier height as shown previously by Zeng *et al.* in one of the first demonstrations of GBHETs, as shown in Fig. 4.9[79]. While a filter barrier height of around 3 eV is formed at the Al_2O_3/graphene interface, the HET was switched on at a V_{BE} of more than 4.5 V. The discrepancy was attributed to the fact that the kinetic energy of the hot electrons exhibit a distribution centered below the applied V_{BE}, due to energy loss from the scattering processes in the tunnel barrier. Thus, a larger excess energy is needed, i.e., V_{BE} needs to exceed the filter barrier height by an amount related to the tunnel barrier thickness and interface properties.

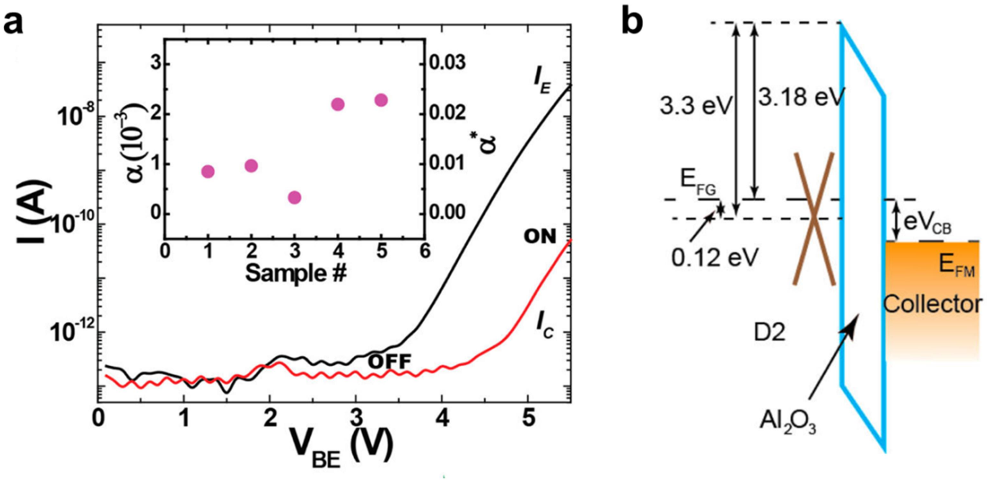

Figure 4.9 Transition between on and off state of GBHET with SiO_2 as the tunnel barrier. **a,** Input and transfer characteristics of GBHET with SiO_2 as the tunnel barrier. Transition between the on and off state is observed at a V_{BE} of 4.5 V. **b,** Energy band diagram of the GBHET with SiO_2 as the tunnel barrier. The filter barrier height is around 3 eV. Adapted with permission from ref. (79). Copyright 2013 ACS.

The upper limit of the V_{EB} is defined by the break-down voltage of the Si (n^{++})/graphene junction. The J_E as a function of V_{BE} is plotted in Fig. 4.10a and the break-down voltage is around 2 V. This placed a stringent requirement on the upper limit of the filter barrier height, φ_C, as φ_C needs to be smaller than the breakdown voltage (as shown in Fig. 4.10b). Table 4.1 lists literature values of the bandgap and electron affinity for various insulators and semiconductors. Rough estimates of the filter barrier height when coupled with the graphene base material is simultaneously given, which assumes a graphene work function of 4.6 eV and minimal interfacial dipole. A few oxides holds promise as suitable filter barrier materials for the proposed high current density GBHETs, including ZnO, TiO_2 and ZrO_2. vdW semiconductors such as MoS_2 and $MoTe_2$ also exhibit small filter barrier heights when coupled with graphene. While large area growth of multi-layer TMD materials have been recently demonstrated using CVD, vertical transport across these materials are characterized by a high leakage current due to defects and pinhole formation. Further improvement on the material quality could enable HETs consisting entirely of vdW materials with atomically flat interfaces to minimize back scattering, hence achieving high current gains. For this chapter, we will limit our discussion to oxide grown using ALD as the filter barrier materials.

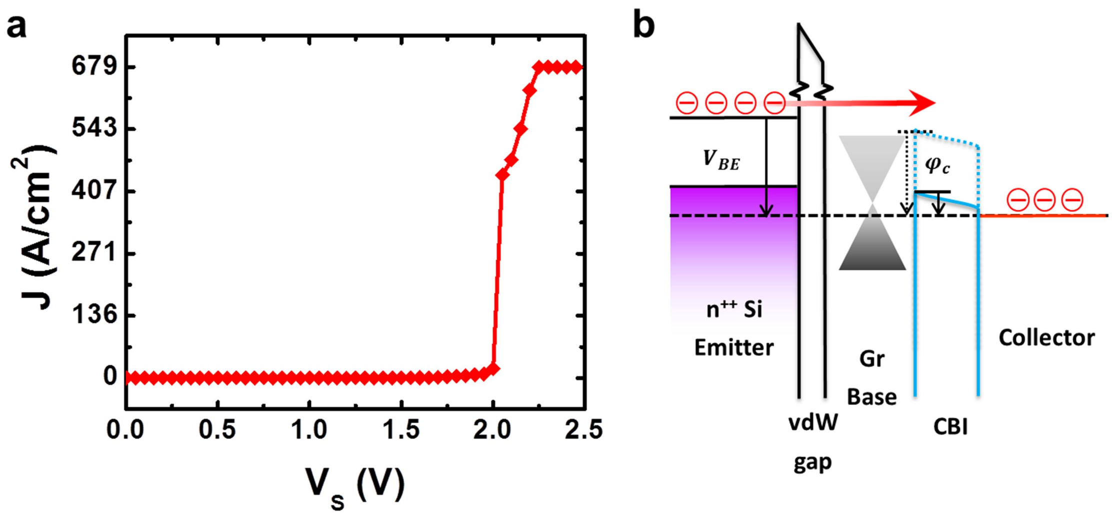

Figure 4.10 Limitation on the filter barrier height for high current gain GBHET. a, Breakdown behavior of the Si-graphene junction at around 2 V. **b,** Energy band diagram for the on state of GBHET. The highest applicable V_{BE} is limited to below 2 V, which sets a limit on the φ_C.

Table 4.1 Literature values of the bandgap and electron affinity for various insulators and semiconductors. *Exact value of the electron affinity (χ) depends on the deposition process.

Material	E_G (eV)	χ (eV)	φ_C (eV)	Material	E_G (eV)	χ (eV)	φ_C (eV)
SiO_2	9.0[112]	0.9[112]	3.7	**ZnO**	3.3[113]	4.2[114]	0.4
Al_2O_3	8.8[112]	1.6~2.6[115, 116]*	2.0~3.0	**Si**	1.1	4.0	0.6
HfO_2	6.0[112]	2.0~2.5[117, 118]	2.1~2.6	**BN**	5.9[119]	< 0[120]	>4.6
ZrO_2	5.8[112]	2.5~3.3[112, 121, 122]	1.3~2.1	**$MoTe_2$**	0.96[123]	4.1[124]	0.5
TiO_2	3.1[112]	3.9~4.2[112, 125]	0.4~0.7	**MoS_2**	1.90[34]	4.0[124]	0.6

4.4 ZnO as the Filter Barrier of the High Current Density GBHETs

4.4.1 Input Characteristics of the GBHETs with ZnO as the Filter Barrier

Thin films of ZnO are deposited using an ALD system (Fiji by Ultratech) at 200 °C and 100 °C on top of HF treated Si (n^{++}) to evaluate the leakage current level around the ZnO layer. *J-V* characteristics are shown in Fig. 4.11a, and the ZnO layer grown at 100 °C exhibits a much lower leakage current. The lower leakage current stems from the amorphous nature of the ZnO deposited at low temperature, compared to the less uniform polycrystalline ZnO deposited at higher temperatures, as shown in Fig. 4.11 b. Thus, ZnO layers deposited at 100 °C are adopted as the filter barrier for the GBHET discussed in this section.

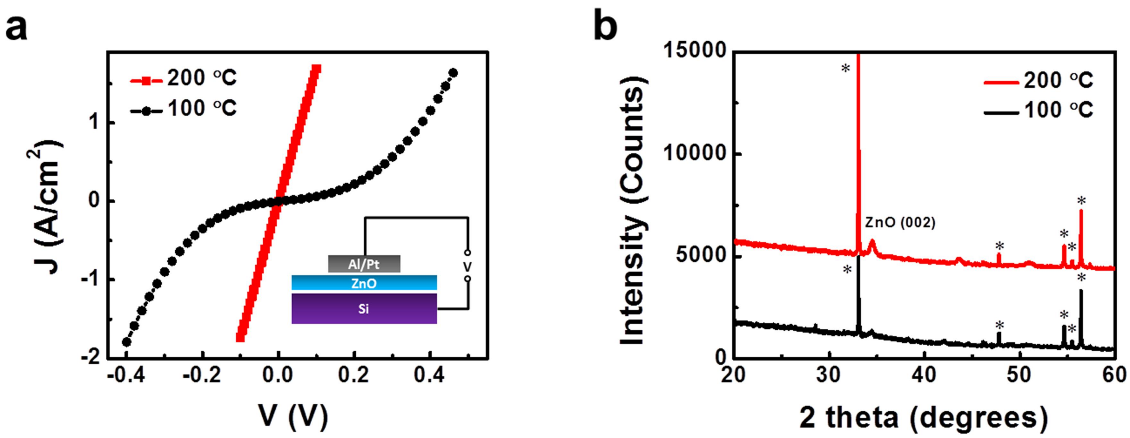

Figure 4.11 ALD deposited ZnO as the filter barrier of high current density GBHET. a, Leakage current across ZnO deposited at different temperatures. **b,** XRD spectra of ZnO deposited at different temperatures. Substrate peaks are marked with asterisks. ZnO grown at higher temperature exhibits characteristic peaks, indication of a polycrystalline material.

The top-down optical micrograph of the GBHET is shown in Fig. 4.12a, and a schematic diagram of the cross section of the device in common base measurement configuration is shown in Fig. 4.12b. Si (n^{++}) substrates with a doping density of $10^{19}/cm^3$ is chosen as the substrate and the emitter electrode. To achieve a well-defined injection area and isolate individual devices, field oxides are deposited using the LOCOS (local oxidation of the silicon) method. This is followed by HF treatment of the patterned Si substrate, and the CVD grown graphene base materials is immediately transferred onto the Si substrate to ensure a clean vdW interface between the Si emitter and graphene base. Cr/Au are deposited onto graphene as the base electrode, and low temperature ALD ZnO is deposited as the filter barrier, and Pt/Al layers are deposited as the collector electrode.

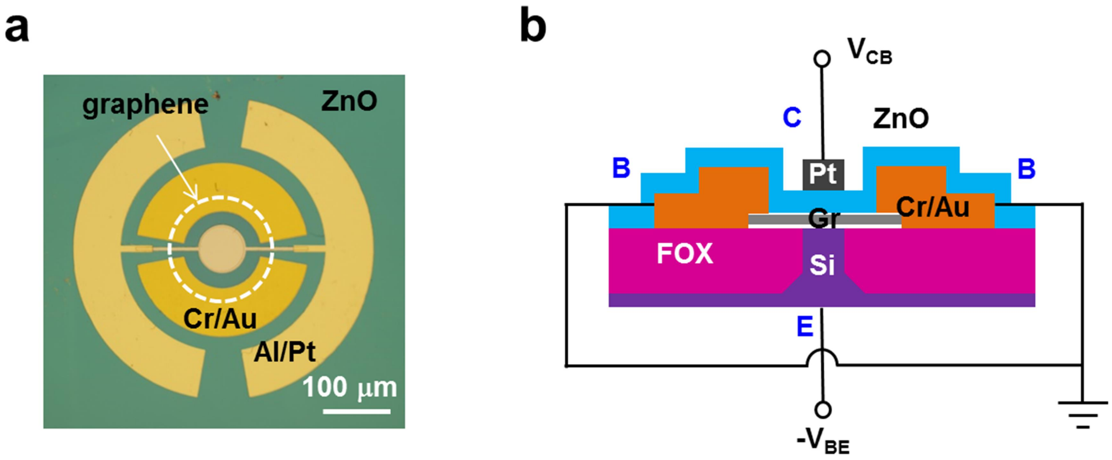

Figure 4.12 Device structure of the GBHET with ZnO as the filter barrier. a, Top-view optical image of GBHET with ZnO as the filter barrier. The graphene region is indicated by the white dash line. **b,** Schematic diagram showing the cross section of GBHET with ZnO as the filter barrier.

Fig. 4.13 shows the schematic band diagram of the GBHET in the thermal equilibrium (a) and the on state (analogous to the forward active mode of BJT). As a result of the low lying conduction band of ZnO, a small filter barrier height of around 0.4 eV is formed at the graphene/ZnO base/collector interface. Hot electrons are injected by applying a positive bias to the base-emitter tunneling junction, and the device is switched to the on state when the injected electrons have enough energy to pass through the filter barrier as shown in Fig. 4.13b. Positive collector-base voltages can be applied to tune the effective width and height of the filter barrier.

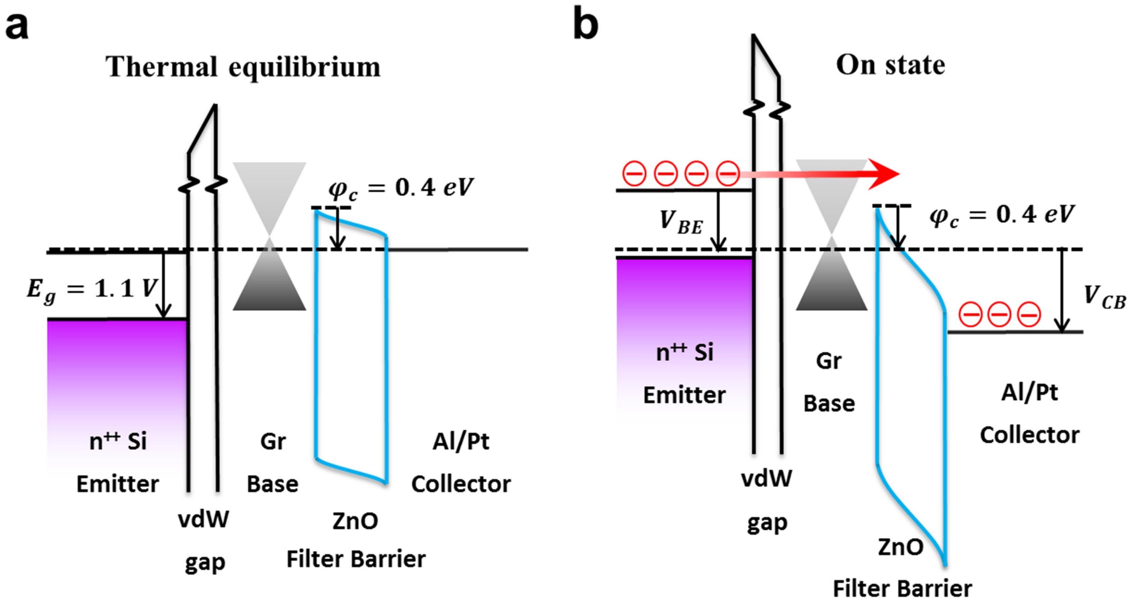

Figure 4.13 Schematic band diagram of the GBHET with ZnO as the filter barrier. a, Schematic band diagram of the GBHET in the thermal equilibrium. **b,** Schematic band diagram of the GBHET in the on state.

4.4.2 Transfer Characteristics of the GBHETs with ZnO as the Filter Barrier

The GBHET is measured in a common base configuration as shown in Fig. 4.12b. All measurements shown in this section is carried out at 1.9 K in a PPMS system, in order to reduce effects from thermally activated processes. The input characteristics (J_E-V_{BE}) of the GBHET is shown in Fig. 4.14a for various collector voltages (V_{CB}), and the current injected from the Si through the vdW gap to the graphene is of a tunneling nature, and current level does not change significantly with different collector biases. The transfer characteristics (J_C-V_{BE}) are shown in Fig. 4.14b. For V_{CB} = 0, the collector current starts to increase from zero around an injection voltage around 0.5 V, which is consistent with a filter barrier height of 0.4 V formed at the graphene/ZnO interface. The small difference between the turn-on voltage and the filter barrier height is evidence that minimal energy loss occurs during the electrons' vertical injection through the vdW gap and the graphene base region. With increasing V_{CB}, the collector current increases, and the collector current consists of two components: the leakage current across the ZnO filter barrier from the applied V_{CB}, and the hot electron current that passes through the filter barrier and into the collector. The leakage current component is not a sensitive function of V_{BE}, thus they can be deducted to evaluate the pure hot electron contribution to the collector current, ΔJ_C, as shown in Fig. 4.14c. Plotting J_E along with ΔJ_C as a function of V_{BE}, a common base current gain of 21.9 % is obtained (Fig. 4.14d), significantly higher than those from previous reports of GBHETs.

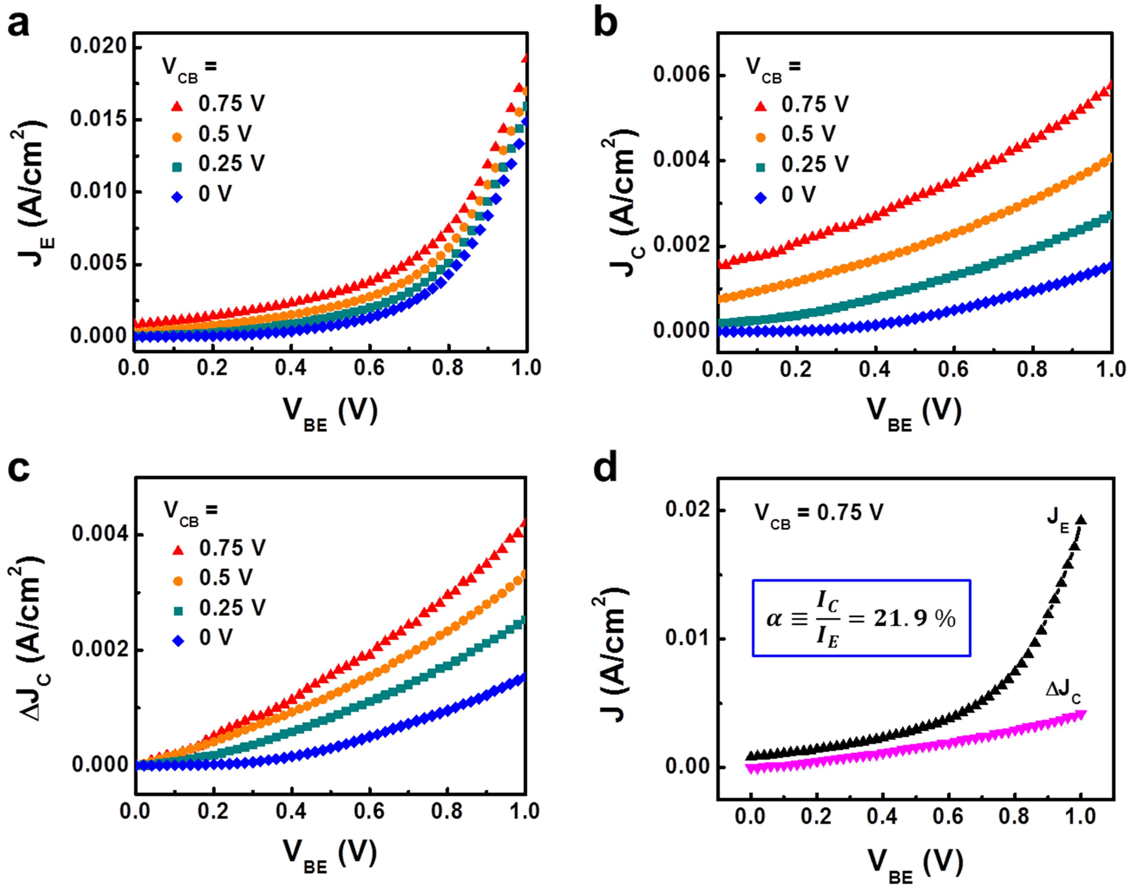

Figure 4.14 Input and transfer characteristics of the GBHET with ZnO as the filter barrier. **a,** J_E as a function of V_{BE} at various V_{CB}. **b,** J_C as a function of V_{BE} at various V_{CB}. **c,** the hot electron contribution of J_C (ΔJ_C) as a function of V_{BE} at various V_{CB}. **d,** J_E and ΔJ_C as a function of V_{BE} at V_{CB}=0.75 V. Inset shows the calculated common base current gain (α).

4.4.3 Output Characteristics of the GBHETs with ZnO as the Filter Barrier

The injection current J_E as a function V_{CB} is plotted in Fig. 4.15a. Consistent with the input characteristics shown in Fig. 4.14a, J_E does not vary significantly with increasing V_{CB}, but a slight increase is observed. In order to understand how the collector voltage can affect the injection current, a schematic diagram of the DC equivalent circuit of the GBHET is shown in Fig. 4.15b. When V_{BE} is close to zero, electrons flow from both the emitter and the base towards the collector electrode, and the current direction is shown in the upper panel in Fig. 4.15c. When V_{BE} is increased, the current direction in the base region changes and the electrons travel from the emitter to either the base electrode or the collector, as shown in the lower panel of Fig. 4.15c. In either case, changes in V_{CB} will lead to changes in the base current J_B, which in turn changes the voltage drop across the tunnel barrier, thus changing the injection current. This instability in the injection current can potentially be eliminated by reducing the base resistance or the base current.

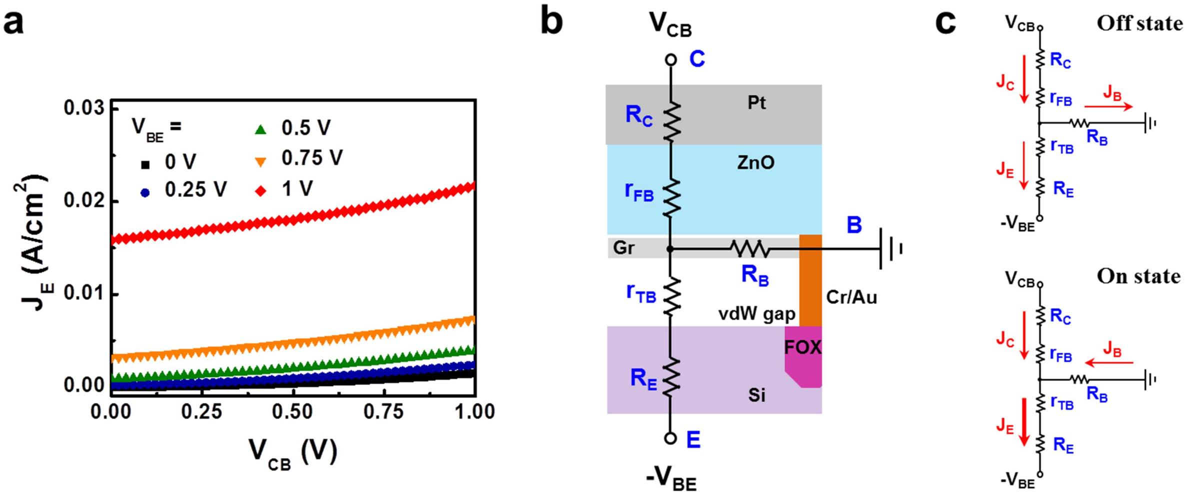

Figure 4.15 The dependence of J_E as a function of V_{CB}. a, J_E as a function of V_{CB} at various V_{BE}. **b,** Schematic diagram showing the DC equivalent circuit model of the GBHET. **c,** Schematic diagram of the DC equivalent circuit model showing the current direction in the off state and on state.

The output characteristic (J_C-V_{CB}) of the GBHET is shown in Fig. 4.16a, and the hot electron contribution to the collector current is shown in Fig. 4.16b. For injection voltages (V_{BE}) higher than 0.5 V, some of the hot electrons can pass through the filter barrier even when the collector voltage (V_{CB}) is zero. With increasing V_{CB}, the collector current increases as a result of a lower effective filter barrier height. The common base current gain (α) as a function V_{CB} is shown in Fig. 4.16c, it is shown that α can be tuned over a wide range by changing the V_{CB}.

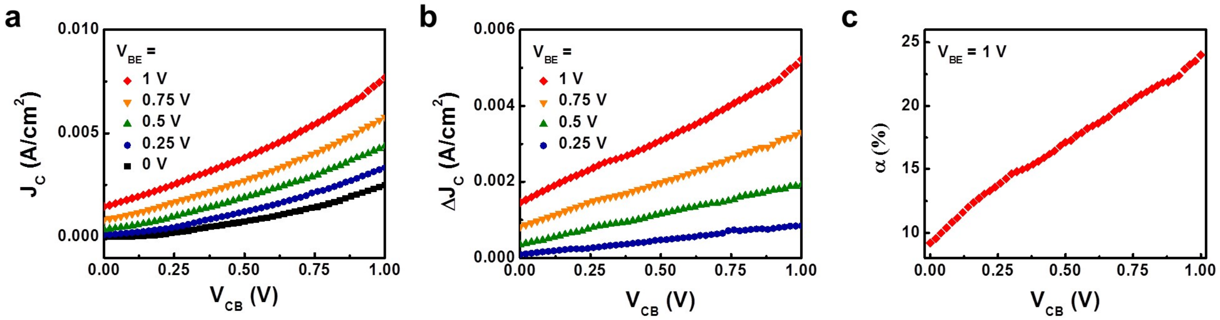

Figure 4.16 Output characteristics of the GBHET with ZnO as the filter barrier. a, J_C as a function of V_{CB} at various V_{BE}. **b,** ΔJ_C as a function of V_{CB} at various V_{BE}. **c,** α as a function of V_{CB} at $V_{BE} = 1$ V.

4.4.4 Common Emitter Characteristics of the GBHETs with ZnO as the Filter Barrier

The common emitter characteristics of the GBHETs is also measured, and the result is shown in Fig. 4.17. The measurement setup is shown in the inset of Fig. 4.17b. In this configuration, the emitter is grounded, and the injection voltage (V_{BE}) is applied to the base region, while a collector-emitter voltage (V_{CE}) is applied to the collector. Similar to the common base configuration, the injection current (J_E) varies with V_{CE}, as a result of variation in the voltage drop across the tunnel barrier, as shown in Fig. 4.17a. J_C as a function of V_{CE} is shown in Fig 4.17b. While higher J_C is observed with higher V_{BE} for the same V_{CB}, there is not a significant increase in the J_C for the same V_{CE}, as a result of the decrease in the leakage current across the ZnO layer.

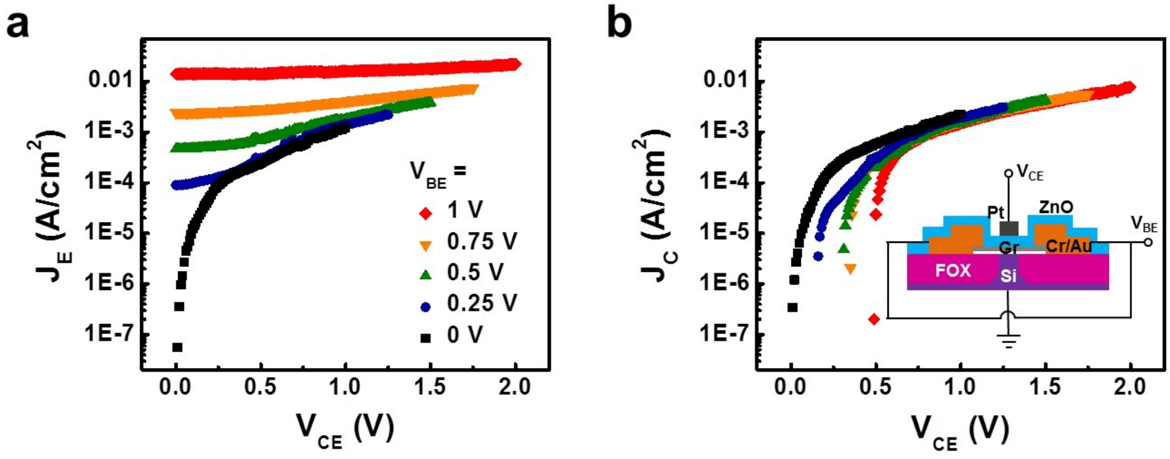

Figure 4.17 Common emitter characteristics of the GBHET with ZnO as the filter barrier. a, J_E as a function of V_{CE} at various V_{BE}. **b,** J_C as a function of V_{CE} at various V_{BE}. Inset shows a schematic diagram of the common emitter measurement setup.

4.5 Conclusions

In this chapter, GBHET with vdW gap as the tunnel barrier is demonstrated. As presented in the previous chapters, the fully preserved vdW gap formed at the interface between Si (n^{++}) and graphene can act effectively as a tunnel barrier. Therefore no additional barrier is needed when Si (n^{++}) is adopted as the emitter and graphene as the base region of the HET. In addition, the vertically injected hot electrons can propagate vertically through graphene without significant interaction, thus graphene can act as a highly efficient base material for HETs, with lower loss due to scattering. The atomically thin graphene leads to minimized base transit times, essential to potential high frequency applications. Much improved injected current density is achieved, with a common base current gain of more than 20%. The turn-on voltage is approximately equal to the filter barrier height formed between the graphene base and the ZnO filter barrier, evidence that minimal loss is achieved in this structure.

Chapter 5 Conclusions and Future Works

5.1 Conclusions

In this dissertation, we report the important process of electron tunneling through the vdW gap using graphene as a model material, as well as its application in HETs. We found that a fully preserved vdW gap is retained at the interface of the hydrogen terminated silicon and the graphene; therefore the graphene can effectively act as a tunnel barrier. By constructing a vertical heterostructure in which the graphene is sandwiched between two vertically aligned electrodes, pure out-of-plane transport across the single layer graphene is achieved. We found that graphene and the vdW gap act together as a tunnel barrier to propagating electrons, with minimal interaction between tunneling electrons and the in-plane band structure as a result of the transverse momentum mismatch. Meanwhile, the tunneling process is modified by the semi-metallic in-plane transport property of graphene, through the ability of the graphene layer to control the charge and potential distribution via the quantum capacitance effect. Coupling between the in-plane charge transport within the basal plane of graphene and the vertical tunneling process is also explored, by tracking the evolution of low temperature electron tunneling spectrums. Based on these results, we are able to construct the very first comprehensive model for the out-of-plane transport across 2D materials.

To explore the potential application of graphene in vertical devices, graphene is applied as the base material of HETs, with the fully preserved vdW gap as the tunnel barrier. Elimination of an artificial tunnel barrier is successfully achieved, which leads to highly improved current density, current gain and significantly reduced turn-on voltage. Note that this work only serves as a prototype for tunneling across the vdW gap as the emitter-base junction for HETs. Improvement on the graphene/metal oxide interface and suppression of the leakage current across the metal oxide filter barrier will push the current density and current gain towards practical levels suitable for potential high frequency applications.

5.2 Suggested Future Works

Vertical transport of vdW materials is a fascinating field with many interesting topics yet to discover. In this dissertation, the vertical transport behavior of single layer graphene and decoupled multi-layer graphene with random stacking orientation has been investigated. For coupled multi-layer graphene sheets, the transport behavior could be very different, and it is expected that a critical layer number exists for the transition towards the typical metallic behavior of graphite. Similar experiments can be conducted on semiconducting vdW materials and topological insulators, which will further our understanding of the out of plane transport of vdW materials, and its relation to their lateral band structure.

The vertical transport across vdW gaps is inherent to all vdW material based devices, thus it is critical to understand how it affects the characteristics and performance of these devices. It has been proposed that injection through the vdW gaps affects the contact resistance of metal contacts to vdW materials, whether it is the limiting factor for various vdW materials remains to be determined. Investigations on how to eliminate this effect is also critical to vdW material's application in electronic devices. Another interesting topic is how the vdW gaps affect the characteristics of opto-electronics based on vdW heterostructures. In such devices, the excitons are formed at the interface of two vdW layer separated by the vdW gap. Thus the vdW gap could significantly alter the opto-electronics' behavior.

While the HETs demonstrated here exhibits improved current density and current gain, they are still low compared to that of THETA. This is primary due to the fact that although the vdW gaps promote a clean interface between vdW materials, the growth of 3D materials on top of these 2D materials could be difficult due to a lack of nucleation sites. How to grow high quality 3D layers (such as metal oxides) without compromising the properties of vdW materials is critical to achieve a high current gain for vdW materials based HETs. On the other hand, constructing a HET structure consisted solely of vdW materials is another promising way to achieve clean interfaces between the emitter, base and collector, thus reducing back scattering and energy loss for the hot electrons. Currently the limitation is the inability to grow large area, pin-hole free 2D insulators (such as *h*-BN) and semiconductors (such as TMD materials). With the continued effort in this community to improve the quality of bottom-up synthesized, large area vdW materials, this could be another promising direction towards vdW HETs with high current density, high current density and high frequency operation.

Reference

1. Novoselov, K. S.; Geim, A. K.; Morozov, S. V.; Jiang, D.; Zhang, Y.; Dubonos, S. V.; Grigorieva, I. V.; Firsov, A. A., Electric Field Effect in Atomically Thin Carbon Films. *Science* **2004,** *306* (5696), 666-669.

2. Geim, A. K.; Novoselov, K. S., The rise of graphene. *Nat. Mater.* **2007,** *6* (3), 183-191.

3. Novoselov, K. S.; Jiang, D.; Schedin, F.; Booth, T. J.; Khotkevich, V. V.; Morozov, S. V.; Geim, A. K., Two-dimensional atomic crystals. *PNAS* **2005,** *102* (30), 10451-10453.

4. Park, J.; Mitchel, W. C.; Grazulis, L.; Smith, H. E.; Eyink, K. G.; Boeckl, J. J.; Tomich, D. H.; Pacley, S. D.; Hoelscher, J. E., Epitaxial Graphene Growth by Carbon Molecular Beam Epitaxy (CMBE). *Adv. Mat.* **2010,** *22* (37), 4140-4145.

5. Lin, Y.-M.; Dimitrakopoulos, C.; Jenkins, K. A.; Farmer, D. B.; Chiu, H.-Y.; Grill, A.; Avouris, P., 100-GHz Transistors from Wafer-Scale Epitaxial Graphene. *Science* **2010,** *327* (5966), 662-662.

6. Li, X.; Cai, W.; An, J.; Kim, S.; Nah, J.; Yang, D.; Piner, R.; Velamakanni, A.; Jung, I.; Tutuc, E.; Banerjee, S. K.; Colombo, L.; Ruoff, R. S., Large-Area Synthesis of High-Quality and Uniform Graphene Films on Copper Foils. *Science* **2009,** *324* (5932), 1312-1314.

7. Hernandez, Y.; Nicolosi, V.; Lotya, M.; Blighe, F. M.; Sun, Z.; De, S.; McGovern, I. T.; Holland, B.; Byrne, M.; Gun'Ko, Y. K.; Boland, J. J.; Niraj, P.; Duesberg, G.; Krishnamurthy, S.; Goodhue, R.; Hutchison, J.; Scardaci, V.; Ferrari, A. C.; Coleman, J. N., High-yield production of graphene by liquid-phase exfoliation of graphite. *Nat. Nano.* **2008,** *3* (9), 563-568.

8. Bae, S.; Kim, H.; Lee, Y.; Xu, X.; Park, J.-S.; Zheng, Y.; Balakrishnan, J.; Lei, T.; Ri Kim, H.; Song, Y. I.; Kim, Y.-J.; Kim, K. S.; Ozyilmaz, B.; Ahn, J.-H.; Hong, B. H.; Iijima, S., Roll-to-roll production of 30-inch graphene films for transparent electrodes. *Nat. Nano.* **2010,** *5* (8), 574-578.

9. Wang, Q. H.; Kalantar-Zadeh, K.; Kis, A.; Coleman, J. N.; Strano, M. S., Electronics and optoelectronics of two-dimensional transition metal dichalcogenides. *Nat. Nano.* **2012,** *7* (11), 699-712.

10. Li, L.; Yu, Y.; Ye, G. J.; Ge, Q.; Ou, X.; Wu, H.; Feng, D.; Chen, X. H.; Zhang, Y., Black phosphorus field-effect transistors. *Nat. Nano.* **2014,** *9* (5), 372-377.

11. Pacilé, D.; Meyer, J. C.; Girit, Ç. Ö.; Zettl, A., The two-dimensional phase of boron nitride: Few-atomic-layer sheets and suspended membranes. *Appl. Phys. Lett.* **2008,** *92* (13), 133107.

12. Geim, A. K.; Grigorieva, I. V., Van der Waals heterostructures. *Nature* **2013,** *499* (7459), 419-425.

13. Du, X.; Skachko, I.; Barker, A.; Andrei, E. Y., Approaching ballistic transport in suspended graphene. *Nat. Nano.* **2008,** *3* (8), 491-495.

14. Xu, K.; Chen, P.; Li, X.; Wu, C.; Guo, Y.; Zhao, J.; Wu, X.; Xie, Y., Ultrathin Nanosheets of Vanadium Diselenide: A Metallic Two-Dimensional Material with Ferromagnetic Charge-Density-Wave Behavior. *Angew. Chem. Int. Ed.* **2013,** *52* (40), 10477-10481.

15. Lebègue, S.; Björkman, T.; Klintenberg, M.; Nieminen, R. M.; Eriksson, O., Two-Dimensional Materials from Data Filtering and Ab Initio Calculations. *Phys. Rev. X* **2013,** *3* (3), 031002.

16. Xiu, F.; He, L.; Wang, Y.; Cheng, L.; Chang, L.-T.; Lang, M.; Huang, G.; Kou, X.; Zhou, Y.; Jiang, X.; Chen, Z.; Zou, J.; Shailos, A.; Wang, K. L., Manipulating surface states in topological insulator nanoribbons. *Nat. Nano.* **2011,** *6* (4), 216-221.

17. Novoselov, K. S.; Mishchenko, A.; Carvalho, A.; Castro Neto, A. H., 2D materials and van der Waals heterostructures. *Science* **2016,** *353* (6298).

18. Withers, F.; Del Pozo-Zamudio, O.; Mishchenko, A.; Rooney, A. P.; Gholinia, A.; Watanabe, K.; Taniguchi, T.; Haigh, S. J.; Geim, A. K.; Tartakovskii, A. I.; Novoselov, K. S., Light-emitting diodes by band-structure engineering in van der Waals heterostructures. *Nat. Mater.* **2015,** *14* (3), 301-306.

19. Gong, Y.; Lin, J.; Wang, X.; Shi, G.; Lei, S.; Lin, Z.; Zou, X.; Ye, G.; Vajtai, R.; Yakobson, B. I.; Terrones, H.; Terrones, M.; Tay, Beng K.; Lou, J.; Pantelides, S. T.; Liu, Z.; Zhou, W.; Ajayan, P. M., Vertical and in-plane heterostructures from WS_2/MoS_2 monolayers. *Nat. Mater.* **2014,** *13* (12), 1135-1142.

20. Georgiou, T.; Jalil, R.; Belle, B. D.; Britnell, L.; Gorbachev, R. V.; Morozov, S. V.; Kim, Y.-J.; Gholinia, A.; Haigh, S. J.; Makarovsky, O.; Eaves, L.; Ponomarenko, L. A.; Geim, A. K.; Novoselov, K. S.; Mishchenko, A., Vertical field-effect transistor based on graphene-WS_2 heterostructures for flexible and transparent electronics. *Nat. Nano.* **2013,** *8* (2), 100-103.

21. Li, M.-Y.; Shi, Y.; Cheng, C.-C.; Lu, L.-S.; Lin, Y.-C.; Tang, H.-L.; Tsai, M.-L.; Chu, C.-W.; Wei, K.-H.; He, J.-H.; Chang, W.-H.; Suenaga, K.; Li, L.-J., Epitaxial growth of a monolayer WSe_2-MoS_2 lateral p-n junction with an atomically sharp interface. *Science* **2015,** *349* (6247), 524.

22. Mudd, G. W.; Svatek, S. A.; Hague, L.; Makarovsky, O.; Kudrynskyi, Z. R.; Mellor, C. J.; Beton, P. H.; Eaves, L.; Novoselov, K. S.; Kovalyuk, Z. D.; Vdovin, E. E.; Marsden, A. J.; Wilson, N. R.; Patanè, A., High Broad-Band Photoresponsivity of Mechanically Formed InSe–Graphene van der Waals Heterostructures. *Adv. Mater.* **2015,** *27* (25), 3760-3766.

23. Castro Neto, A. H.; Guinea, F.; Peres, N. M. R.; Novoselov, K. S.; Geim, A. K., The electronic properties of graphene. *Rev. Mod. Phys.* **2009,** *81* (1), 109-162.

24. Wallace, P. R., The Band Theory of Graphite. *Phys. Rev.* **1947,** *71* (9), 622-634.

25. Novoselov, K. S.; Geim, A. K.; Morozov, S. V.; Jiang, D.; Katsnelson, M. I.; Grigorieva, I. V.; Dubonos, S. V.; Firsov, A. A., Two-dimensional gas of massless Dirac fermions in graphene. *Nature* **2005,** *438* (7065), 197-200.

26. Katsnelson, M. I.; Novoselov, K. S.; Geim, A. K., Chiral tunnelling and the Klein paradox in graphene. *Nat. Phys.* **2006,** *2* (9), 620-625.

27. Tran, T. T.; Bray, K.; Ford, M. J.; Toth, M.; Aharonovich, I., Quantum emission from hexagonal boron nitride monolayers. *Nat. Nano.* **2016,** *11* (1), 37-41.

28. Watanabe, K.; Taniguchi, T.; Kanda, H., Direct-bandgap properties and evidence for ultraviolet lasing of hexagonal boron nitride single crystal. *Nat. Mater.* **2004,** *3* (6), 404-409.

29. Britnell, L.; Gorbachev, R. V.; Jalil, R.; Belle, B. D.; Schedin, F.; Katsnelson, M. I.; Eaves, L.; Morozov, S. V.; Mayorov, A. S.; Peres, N. M. R.; Castro Neto, A. H.; Leist, J.; Geim, A. K.; Ponomarenko, L. A.; Novoselov, K. S., Electron Tunneling through Ultrathin Boron Nitride Crystalline Barriers. *Nano Lett.* **2012,** *12* (3), 1707-1710.

30. Dean, C. R.; Young, A. F.; MericI; LeeC; WangL; SorgenfreiS; WatanabeK; TaniguchiT; KimP; Shepard, K. L.; HoneJ, Boron nitride substrates for high-quality graphene electronics. *Nat. Nano.* **2010,** *5* (10), 722-726.

31. Kim, K. K.; Hsu, A.; Jia, X.; Kim, S. M.; Shi, Y.; Dresselhaus, M.; Palacios, T.; Kong, J., Synthesis and Characterization of Hexagonal Boron Nitride Film as a Dielectric Layer for Graphene Devices. *ACS Nano* **2012,** *6* (10), 8583-8590.

32. Britnell, L.; Gorbachev, R. V.; Jalil, R.; Belle, B. D.; Schedin, F.; Mishchenko, A.; Georgiou, T.; Katsnelson, M. I.; Eaves, L.; Morozov, S. V.; Peres, N. M. R.; Leist, J.; Geim, A. K.; Novoselov, K. S.; Ponomarenko, L. A., Field-Effect Tunneling Transistor Based on Vertical Graphene Heterostructures. *Science* **2012,** *335* (6071), 947-950.

33. Mishchenko, A.; Tu, J. S.; Cao, Y.; Gorbachev, R. V.; Wallbank, J. R.; Greenaway, M. T.; Morozov, V. E.; Morozov, S. V.; Zhu, M. J.; Wong, S. L.; Withers, F.; Woods, C. R.; Kim, Y. J.; Watanabe, K.; Taniguchi, T.; Vdovin, E. E.; Makarovsky, O.; Fromhold, T. M.; Fal'ko, V. I.; Geim, A. K.; Eaves, L.; Novoselov, K. S., Twist-controlled resonant tunnelling in graphene/boron nitride/graphene heterostructures. *Nat. Nano.* **2014,** *9* (10), 808-813.

34. Mak, K. F.; Lee, C.; Hone, J.; Shan, J.; Heinz, T. F., Atomically Thin MoS_2: A New Direct-Gap Semiconductor. *Phys. Rev. Lett.* **2010,** *105* (13), 136805.

35. Asahina, H.; Morita, A., Band structure and optical properties of black phosphorus. *J. Phys. C: Solid State Phys.* **1984,** *17* (11), 1839.

36. Splendiani, A.; Sun, L.; Zhang, Y.; Li, T.; Kim, J.; Chim, C.-Y.; Galli, G.; Wang, F., Emerging Photoluminescence in Monolayer MoS_2. *Nano Lett.* **2010,** *10* (4), 1271-1275.

37. Zhao, W.; Ghorannevis, Z.; Chu, L.; Toh, M.; Kloc, C.; Tan, P.-H.; Eda, G., Evolution of Electronic Structure in Atomically Thin Sheets of WS_2 and WSe_2. *ACS Nano* **2013,** *7* (1), 791-797.

38. Radisavljevic, B.; Radenovic, A.; Brivio, J.; Giacometti, V.; Kis, A., Single-layer MoS_2 transistors. *Nat. Nano.* **2011,** *6* (3), 147-150.

39. Zeng, H.; Dai, J.; Yao, W.; Xiao, D.; Cui, X., Valley polarization in MoS_2 monolayers by optical pumping. *Nat. Nano.* **2012,** *7* (8), 490-493.

40. Mak, K. F.; He, K.; Shan, J.; Heinz, T. F., Control of valley polarization in monolayer MoS_2 by optical helicity. *Nat. Nano.* **2012,** *7* (8), 494-498.

41. Costanzo, D.; Jo, S.; Berger, H.; Morpurgo, A. F., Gate-induced superconductivity in atomically thin MoS_2 crystals. *Nat. Nano.* **2016,** *11* (4), 339-344.

42. Lu, J. M.; Zheliuk, O.; Leermakers, I.; Yuan, N. F. Q.; Zeitler, U.; Law, K. T.; Ye, J. T., Evidence for two-dimensional Ising superconductivity in gated MoS_2. *Science* **2015,** *350* (6266), 1353-1357.

43. Barja, S.; Wickenburg, S.; Liu, Z.-F.; Zhang, Y.; Ryu, H.; Ugeda, M. M.; Hussain, Z.; Shen, Z.-X.; Mo, S.-K.; Wong, E.; Salmeron, M. B.; Wang, F.; Crommie, M. F.; Ogletree, D. F.; Neaton, J. B.; Weber-Bargioni, A., Charge density wave order in 1D mirror twin boundaries of single-layer $MoSe_2$. *Nat. Phys.* **2016,** *12* (8), 751-756.

44. Zhang, H.; Liu, C.-X.; Qi, X.-L.; Dai, X.; Fang, Z.; Zhang, S.-C., Topological insulators in Bi_2Se_3, Bi_2Te_3 and Sb_2Te_3 with a single Dirac cone on the surface. *Nat. Phys.* **2009,** *5* (6), 438-442.

45. Chen, Y. L.; Chu, J.-H.; Analytis, J. G.; Liu, Z. K.; Igarashi, K.; Kuo, H.-H.; Qi, X. L.; Mo, S. K.; Moore, R. G.; Lu, D. H.; Hashimoto, M.; Sasagawa, T.; Zhang, S. C.; Fisher, I. R.; Hussain, Z.; Shen, Z. X., Massive Dirac Fermion on the Surface of a Magnetically Doped Topological Insulator. *Science* **2010,** *329* (5992), 659-662.

46. Li, C. H.; van 't Erve, O. M. J.; Robinson, J. T.; LiuY; LiL; Jonker, B. T., Electrical detection of charge-current-induced spin polarization due to spin-momentum locking in Bi_2Se_3. *Nat. Nano.* **2014,** *9* (3), 218-224.

47. Hsieh, D.; Qian, D.; Wray, L.; Xia, Y.; Hor, Y. S.; Cava, R. J.; Hasan, M. Z., A topological Dirac insulator in a quantum spin Hall phase. *Nature* **2008,** *452* (7190), 970-974.

48. Hsieh, D.; Xia, Y.; Qian, D.; Wray, L.; Dil, J. H.; Meier, F.; Osterwalder, J.; Patthey, L.; Checkelsky, J. G.; Ong, N. P.; Fedorov, A. V.; Lin, H.; Bansil, A.; Grauer, D.; Hor, Y. S.; Cava, R. J.; Hasan, M. Z., A tunable topological insulator in the spin helical Dirac transport regime. *Nature* **2009,** *460* (7259), 1101-1105.

49. Qu, D.-X.; Hor, Y. S.; Xiong, J.; Cava, R. J.; Ong, N. P., Quantum Oscillations and Hall Anomaly of Surface States in the Topological Insulator Bi_2Te_3. *Science* **2010,** *329* (5993), 821-824.

50. Fan, Y.; Upadhyaya, P.; Kou, X.; Lang, M.; Takei, S.; Wang, Z.; Tang, J.; He, L.; Chang, L.-T.; Montazeri, M.; Yu, G.; Jiang, W.; Nie, T.; Schwartz, R. N.; Tserkovnyak, Y.; Wang, K. L., Magnetization switching through giant spin–orbit torque in a magnetically doped topological insulator heterostructure. *Nat. Mater.* **2014,** *13* (7), 699-704.

51. Voigtlaender, B., *Scanning Probe Microscopy*. Springer Berlin Heidelberg: 2015.

52. Zhang, Y.; Brar, V. W.; Wang, F.; Girit, C.; Yayon, Y.; Panlasigui, M.; Zettl, A.; Crommie, M. F., Giant phonon-induced conductance in scanning tunnelling spectroscopy of gate-tunable graphene. *Nat. Phys.* **2008,** *4* (8), 627-630.

53. Wehling, T. O.; Grigorenko, I.; Lichtenstein, A. I.; Balatsky, A. V., Phonon-Mediated Tunneling into Graphene. *Phys. Rev. Lett.* **2008,** *101* (21), 216803.

54. Deshpande, A.; Bao, W.; Miao, F.; Lau, C. N.; LeRoy, B. J., Spatially resolved spectroscopy of monolayer graphene on SiO_2. *Phys. Rev. B* **2009,** *79* (20), 205411.

55. Xue, J.; Sanchez-Yamagishi, J.; Bulmash, D.; Jacquod, P.; Deshpande, A.; Watanabe, K.; Taniguchi, T.; Jarillo-Herrero, P.; LeRoy, B. J., Scanning tunnelling microscopy and spectroscopy of ultra-flat graphene on hexagonal boron nitride. *Nat. Mater.* **2011,** *10* (4), 282-285.

56. Jung, S.; Rutter, G. M.; Klimov, N. N.; Newell, D. B.; Calizo, I.; Hight-Walker, A. R.; Zhitenev, N. B.; Stroscio, J. A., Evolution of microscopic localization in graphene in a magnetic field from scattering resonances to quantum dots. *Nat. Phys.* **2011,** *7* (3), 245-251.

57. Li, G.; Luican, A.; Andrei, E. Y., Scanning Tunneling Spectroscopy of Graphene on Graphite. *Phys. Rev. Lett.* **2009,** *102* (17), 176804.

58. Jung, S.; Park, M.; Park, J.; Jeong, T.-Y.; Kim, H.-J.; Watanabe, K.; Taniguchi, T.; Ha, D. H.; Hwang, C.; Kim, Y.-S., Vibrational Properties of h-BN and h-BN-Graphene Heterostructures Probed by Inelastic Electron Tunneling Spectroscopy. *Sci. Rep.* **2015,** *5*, 16642.

59. Cobas, E.; Friedman, A. L.; van't Erve, O. M. J.; Robinson, J. T.; Jonker, B. T., Graphene As a Tunnel Barrier: Graphene-Based Magnetic Tunnel Junctions. *Nano Lett.* **2012,** *12* (6), 3000-3004.

60. International Technology Roadmap for Semiconductors. www.itrs.net, **2012**.

61. Allain, A.; Kang, J.; Banerjee, K.; Kis, A., Electrical contacts to two-dimensional semiconductors. *Nat. Mater.* **2015,** *14* (12), 1195-1205.

62. Cohen, S. S., Contact resistance and methods for its determination. *Thin Solid Films* **1983,** *104* (3), 361-379.

63. Wang, L.; Meric, I.; Huang, P. Y.; Gao, Q.; Gao, Y.; Tran, H.; Taniguchi, T.; Watanabe, K.; Campos, L. M.; Muller, D. A.; Guo, J.; Kim, P.; Hone, J.; Shepard, K. L.; Dean, C. R., One-Dimensional Electrical Contact to a Two-Dimensional Material. *Science* **2013,** *342* (6158), 614-617.

64. Popov, I.; Seifert, G.; Tománek, D., Designing Electrical Contacts to MoS_2 Monolayers: A Computational Study. *Phys. Rev. Lett.* **2012,** *108* (15), 156802.

65. Gong, C.; Colombo, L.; Wallace, R. M.; Cho, K., The Unusual Mechanism of Partial Fermi Level Pinning at Metal–MoS_2 Interfaces. *Nano Lett.* **2014,** *14* (4), 1714-1720.

66. Leong, W. S.; Nai, C. T.; Thong, J. T. L., What Does Annealing Do to Metal–Graphene Contacts? *Nano Lett.* **2014,** *14* (7), 3840-3847.

67. Kappera, R.; Voiry, D.; Yalcin, S. E.; Branch, B.; Gupta, G.; Mohite, A. D.; Chhowalla, M., Phase-engineered low-resistance contacts for ultrathin MoS_2 transistors. *Nat. Mater.* **2014,** *13* (12), 1128-1134.

68. Mishchenko, A.; Tu, J. S.; CaoY; Gorbachev, R. V.; Wallbank, J. R.; Greenaway, M. T.; Morozov, V. E.; Morozov, S. V.; Zhu, M. J.; Wong, S. L.; Withers, F.; Woods, C. R.; Kim, Y. J.; Watanabe, K.; Taniguchi, T.; Vdovin, E. E.; Makarovsky, O.; Fromhold, T. M.; Fal'ko, V. I.; Geim, A. K.; Eaves, L.; Novoselov, K. S., Twist-controlled resonant tunnelling in graphene/boron nitride/graphene heterostructures. *Nat. Nano.* **2014,** *9* (10), 808-813.

69. Lin, Y.-C.; Ghosh, R. K.; Addou, R.; Lu, N.; Eichfeld, S. M.; Zhu, H.; Li, M.-Y.; Peng, X.; Kim, M. J.; Li, L.-J.; Wallace, R. M.; Datta, S.; Robinson, J. A., Atomically thin resonant tunnel diodes built from synthetic van der Waals heterostructures. *Nat. Comm.* **2015,** *6*, 7311.

70. Sarkar, D.; Xie, X.; Liu, W.; Cao, W.; Kang, J.; Gong, Y.; Kraemer, S.; Ajayan, P. M.; Banerjee, K., A subthermionic tunnel field-effect transistor with an atomically thin channel. *Nature* **2015,** *526* (7571), 91-95.

71. Britnell, L.; Ribeiro, R. M.; Eckmann, A.; Jalil, R.; Belle, B. D.; Mishchenko, A.; Kim, Y.-J.; Gorbachev, R. V.; Georgiou, T.; Morozov, S. V.; Grigorenko, A. N.; Geim, A. K.; Casiraghi, C.; Neto, A. H. C.; Novoselov, K. S., Strong Light-Matter Interactions in Heterostructures of Atomically Thin Films. *Science* **2013,** *340* (6138), 1311-1314.

72. Sze, S. M., *Physics of semiconductor devices*. 1981.

73. Mead, C. A., The tunnel-emission amplifier. *Proc. IEEE* **1960,** *48* (3), 359-361.

74. Spratt, J. P.; Schwarz, R. F.; Kane, W. M., Hot Electrons in Metal Films: Injection and Collection. *Phys. Rev. Lett.* **1961,** *6* (7), 341-342.

75. Heiblum, M., Tunneling hot electron transfer amplifiers (theta): Amplifiers operating up to the infrared. *Solid State Electron* **1981,** *24* (4), 343-366.

76. Heiblum, M.; Thomas, D. C.; Knoedler, C. M.; Nathan, M. I., Tunneling hot ‐ electron transfer amplifier: A hot ‐ electron GaAs device with current gain. *Appl. Phys. Lett.* **1985,** *47* (10), 1105-1107.

77. Chun-Yen, C.; Liu, W. C.; Jame, M. S.; Wang, Y. H.; Luryi, S.; Sze, S. M., Induced base transistor fabricated by molecular beam epitaxy. *IEEE Electron Device Lett.* **1986,** *7* (9), 497-499.

78. Mehr, W.; Dabrowski, J.; Christoph Scheytt, J.; Lippert, G.; Xie, Y.-H.; Lemme, M. C.;

Ostling, M.; Lupina, G., Vertical Graphene Base Transistor. *IEEE Electron Devic. Lett.* **2012,** *33* (5), 691-693.

79. Zeng, C.; Song, E. B.; Wang, M.; Lee, S.; Torres, C. M.; Tang, J.; Weiller, B. H.; Wang, K. L., Vertical Graphene-Base Hot-Electron Transistor. *Nano Lett.* **2013,** *13* (6), 2370-2375.

80. Vaziri, S.; Lupina, G.; Henkel, C.; Smith, A. D.; Östling, M.; Dabrowski, J.; Lippert, G.; Mehr, W.; Lemme, M. C., A Graphene-Based Hot Electron Transistor. *Nano Lett.* **2013,** *13* (4), 1435-1439.

81. Torres, C. M.; Lan, Y.-W.; Zeng, C.; Chen, J.-H.; Kou, X.; Navabi, A.; Tang, J.; Montazeri, M.; Adleman, J. R.; Lerner, M. B.; Zhong, Y.-L.; Li, L.-J.; Chen, C.-D.; Wang, K. L., High-Current Gain Two-Dimensional MoS_2-Base Hot-Electron Transistors. *Nano Lett.* **2015,** *15* (12), 7905-7912.

82. Lan, Y.-W.; Torres, J. C. M.; Zhu, X.; Qasem, H.; Adleman, J. R.; Lerner, M. B.; Tsai, S.-H.; Shi, Y.; Li, L.-J.; Yeh, W.-K.; Wang, K. L., Dual-mode operation of 2D material-base hot electron transistors. *Sci. Rep.* **2016,** *6*, 32503.

83. Vaziri, S.; Belete, M.; Dentoni Litta, E.; Smith, A. D.; Lupina, G.; Lemme, M. C.; Ostling, M., Bilayer insulator tunnel barriers for graphene-based vertical hot-electron transistors. *Nanoscale* **2015,** *7* (30), 13096-13104.

84. Lan, Y.-W.; Torres, C. M.; Tsai, S.-H.; Zhu, X.; Shi, Y.; Li, M.-Y.; Li, L.-J.; Yeh, W.-K.; Wang, K. L., Atomic-Monolayer MoS_2 Band-to-Band Tunneling Field-Effect Transistor. *Small* **2016,** *12* (41), 5676-5683.

85. Cheng, R.; Li, D.; Zhou, H.; Wang, C.; Yin, A.; Jiang, S.; Liu, Y.; Chen, Y.; Huang, Y.; Duan, X., Electroluminescence and Photocurrent Generation from Atomically Sharp WSe_2/MoS_2 Heterojunction p–n Diodes. *Nano Lett.* **2014,** *14* (10), 5590-5597.

86. Furchi, M. M.; Pospischil, A.; Libisch, F.; Burgdörfer, J.; Mueller, T., Photovoltaic Effect in an Electrically Tunable van der Waals Heterojunction. *Nano Lett.* **2014,** *14* (8), 4785-4791.

87. Lee, C.-H.; Lee, G.-H.; van der Zande, A. M.; Chen, W.; Li, Y.; Han, M.; Cui, X.; Arefe, G.; Nuckolls, C.; Heinz, T. F.; Guo, J.; Hone, J.; Kim, P., Atomically thin p–n junctions with van der Waals heterointerfaces. *Nat. Nano.* **2014,** *9* (9), 676-681.

88. Friedman, A. L.; van ‘t Erve, O. M. J.; Li, C. H.; Robinson, J. T.; Jonker, B. T., Homoepitaxial tunnel barriers with functionalized graphene-on-graphene for charge and spin transport. *Nat. Commun.* **2014,** *5*, 3161.

89. Shao, Q.; Yu, G.; Lan, Y.-W.; Shi, Y.; Li, M.-Y.; Zheng, C.; Zhu, X.; Li, L.-J.; Amiri, P. K.; Wang, K. L., Strong Rashba-Edelstein Effect-Induced Spin-Orbit Torques in Monolayer Transition Metal Dichalcogenides/Ferromagnet Bilayers. *Nano Lett.* **2016**, 7514-7520.

90. Amet, F.; Williams, J. R.; Garcia, A. G. F.; Yankowitz, M.; Watanabe, K.; Taniguchi, T.; Goldhaber-Gordon, D., Tunneling spectroscopy of graphene-boron-nitride heterostructures.

Phys. Rev. B **2012,** *85* (7), 073405.

91. Zeng, C.; Wang, M.; Zhou, Y.; Lang, M.; Lian, B.; Song, E.; Xu, G.; Tang, J.; Torres, C.; Wang, K. L., Tunneling spectroscopy of metal-oxide-graphene structure. *Appl. Phys. Lett.* **2010,** *97* (3), 032104.

92. Zhang, Y.; Brar, V. W.; Girit, C.; Zettl, A.; Crommie, M. F., Origin of spatial charge inhomogeneity in graphene. *Nat. Phys.* **2009,** *5* (10), 722-726.

93. Mingqiang, B.; Wang, K. L., Accurately measuring current-voltage characteristics of tunnel diodes. *IEEE Transactions on Electron Devices* **2006,** *53* (10), 2564-2568.

94. Chabal, Y. J.; Higashi, G. S.; Raghavachari, K.; Burrows, V. A., Infrared spectroscopy of Si(111) and Si(100) surfaces after HF treatment: Hydrogen termination and surface morphology. *J. Vac. Sci. Technol., A* **1989,** *7* (3), 2104-2109.

95. Dresselhaus, M. S.; Dresselhaus, G., Intercalation compounds of graphite. *Adv. Phys.* **1981,** *30* (2), 139-326.

96. Bena, C.; Kivelson, S. A., Quasiparticle scattering and local density of states in graphite. *Phys. Rev. B* **2005,** *72* (12), 125432.

97. Casiraghi, C.; Pisana, S.; Novoselov, K. S.; Geim, A. K.; Ferrari, A. C., Raman fingerprint of charged impurities in graphene. *Appl. Phys. Lett.* **2007,** *91* (23), 233108.

98. Berciaud, S.; Ryu, S.; Brus, L. E.; Heinz, T. F., Probing the Intrinsic Properties of Exfoliated Graphene: Raman Spectroscopy of Free-Standing Monolayers. *Nano Lett.* **2009,** *9* (1), 346-352.

99. Tang, J.; Wang, K. L., Electrical spin injection and transport in semiconductor nanowires: challenges, progress and perspectives. *Nanoscale* **2015,** *7* (10), 4325-4337.

100. Schmidt, G., Concepts for spin injection into semiconductors—a review. *J. Phys. D: Appl. Phys.* **2005,** *38* (7), R107.

101. Murphy, E. L.; Good, R. H., Thermionic Emission, Field Emission, and the Transition Region. *Phys. Rev.* **1956,** *102* (6), 1464-1473.

102. Stratton, R., Volt-current characteristics for tunneling through insulating films. *J. Phys. Chem. Solids* **1962,** *23* (9), 1177-1190.

103. Simmons, J. G., Generalized Formula for the Electric Tunnel Effect between Similar Electrodes Separated by a Thin Insulating Film. *J. Appl. Phys.* **1963,** *34* (6), 1793-1803.

104. Fang, T.; Konar, A.; Xing, H.; Jena, D., Carrier statistics and quantum capacitance of graphene sheets and ribbons. *Appl. Phys. Lett.* **2007,** *91* (9), 092109.

105. An, Y.; Shekhawat, A.; Behnam, A.; Pop, E.; Ural, A., Gate tunneling current and quantum capacitance in metal-oxide-semiconductor devices with graphene gate electrodes. *Appl. Phys.*

Lett. **2016,** *109* (22), 223104.

106. Xia, J.; Chen, F.; Li, J.; Tao, N., Measurement of the quantum capacitance of graphene. *Nat. Nano.* **2009,** *4* (8), 505-509.

107. Xu, H.; Zhang, Z.; Wang, Z.; Wang, S.; Liang, X.; Peng, L.-M., Quantum Capacitance Limited Vertical Scaling of Graphene Field-Effect Transistor. *ACS Nano* **2011,** *5* (3), 2340-2347.

108. Zan, R.; Bangert, U.; Ramasse, Q.; Novoselov, K. S., Metal−graphene interaction studied via atomic resolution scanning transmission electron microscopy. *Nano Lett.* **2011,** *11* (3), 1087-1092.

109. Liao, L.; Lin, Y.-C.; Bao, M.; Cheng, R.; Bai, J.; Liu, Y.; Qu, Y.; Wang, K. L.; Huang, Y.; Duan, X., High-speed graphene transistors with a self-aligned nanowire gate. *Nature* **2010,** *467* (7313), 305-308.

110. Liao, L.; Duan, X., Graphene for radio frequency electronics. *Mater. Today* **2012,** *15* (7–8), 328-338.

111. Schwierz, F., Graphene transistors. *Nat. Nano.* **2010,** *5* (7), 487-496.

112. Robertson, J., Band offsets of wide-band-gap oxides and implications for future electronic devices. *J. Vac. Sci. Technol. B* **2000,** *18* (3), 1785-1791.

113. Srikant, V.; Clarke, D. R., On the optical band gap of zinc oxide. *J. Appl. Phys.* **1998,** *83* (10), 5447-5451.

114. Wang, J.-C.; Weng, W.-T.; Tsai, M.-Y.; Lee, M.-K.; Horng, S.-F.; Perng, T.-P.; Kei, C.-C.; Yu, C.-C.; Meng, H.-F., Highly efficient flexible inverted organic solar cells using atomic layer deposited ZnO as electron selective layer. *J. Mater. Chem.* **2010,** *20* (5), 862-866.

115. Pollack, S. R.; Morris, C. E., Electron Tunneling through Asymmetric Films of Thermally Grown Al_2O_3. *J. Appl. Phys.* **1964,** *35* (5), 1503-1512.

116. Huang, M. L.; Chang, Y. C.; Chang, C. H.; Lin, T. D.; Kwo, J.; Wu, T. B.; Hong, M., Energy-band parameters of atomic-layer-deposition Al_2O_3 / InGaAs heterostructure. *Appl. Phys. Lett.* **2006,** *89* (1), 012903.

117. Monaghan, S.; Hurley, P. K.; Cherkaoui, K.; Negara, M. A.; Schenk, A., Determination of electron effective mass and electron affinity in HfO_2 using MOS and MOSFET structures. *Solid State Electron.* **2009,** *53* (4), 438-444.

118. Gu, D.; Dey, S. K.; Majhi, P., Effective work function of Pt, Pd, and Re on atomic layer deposited HfO_2. *Appl. Phys. Lett.* **2006,** *89* (8), 082907.

119. Shi, Y.; Hamsen, C.; Jia, X.; Kim, K. K.; Reina, A.; Hofmann, M.; Hsu, A. L.; Zhang, K.; Li, H.; Juang, Z.-Y.; Dresselhaus, M. S.; Li, L.-J.; Kong, J., Synthesis of Few-Layer Hexagonal Boron Nitride Thin Film by Chemical Vapor Deposition. *Nano Lett.* **2010,** *10* (10), 4134-4139.

120. Loh, K. P.; Sakaguchi, I.; Gamo, M. N.; Tagawa, S.; Sugino, T.; Ando, T., Surface conditioning of chemical vapor deposited hexagonal boron nitride film for negative electron affinity. *Appl. Phys. Lett.* **1999,** *74* (1), 28-30.

121. Vasilopoulou, M.; Kennou, S.; Ladas, S.; Georga, S. N.; Botzakaki, M.; Skarlatos, D.; Krontiras, C. A.; Stathopoulos, N. A.; Argitis, P.; Palilis, L. C., Atomic layer deposited zirconium oxide electron injection layer for efficient organic light emitting diodes. *Org. Electron.* **2013,** *14* (1), 312-319.

122. Chakraborty, S.; Bera, M. K.; Dalapati, G. K.; Paramanik, D.; Varma, S.; Bose, P. K.; Bhattacharya, S.; Maiti, C. K., Leakage current characteristics and the energy band diagram of $Al/ZrO_2/Si_{0.3}Ge_{0.7}$ hetero-MIS structures. *Semicond. Sci. Technol.* **2006,** *21* (4), 467.

123. Lin, Y.-F.; Xu, Y.; Wang, S.-T.; Li, S.-L.; Yamamoto, M.; Aparecido-Ferreira, A.; Li, W.; Sun, H.; Nakaharai, S.; Jian, W.-B.; Ueno, K.; Tsukagoshi, K., Ambipolar $MoTe_2$ Transistors and Their Applications in Logic Circuits. *Adv. Mat.* **2014,** *26* (20), 3263-3269.

124. Schlaf, R.; Lang, O.; Pettenkofer, C.; Jaegermann, W., Band lineup of layered semiconductor heterointerfaces prepared by van der Waals epitaxy: Charge transfer correction term for the electron affinity rule. *J Appl. Phys.* **1999,** *85* (5), 2732-2753.

125. Hsu, W.; Sutter-Fella, C. M.; Hettick, M.; Cheng, L.; Chan, S.; Chen, Y.; Zeng, Y.; Zheng, M.; Wang, H.-P.; Chiang, C.-C.; Javey, A., Electron-Selective TiO_2 Contact for $Cu(In,Ga)Se_2$ Solar Cells. *Sci. Rep.* **2015,** *5*, 16028.